University of Iowa
Iowa Research Online

Theses and Dissertations

Spring 2012

Mechanical analysis of lung CT images using nonrigid registration

Kunlin Cao
University of Iowa

Recommended Citation

Cao, Kunlin. "Mechanical analysis of lung CT images using nonrigid registration." PhD (Doctor of Philosophy) thesis, University of Iowa, 2012.
http://ir.uiowa.edu/etd/2833.

MECHANICAL ANALYSIS OF LUNG CT IMAGES USING NONRIGID

REGISTRATION

by

Kunlin Cao

An Abstract

Of a thesis submitted in partial fulfillment of the
requirements for the Doctor of Philosophy
degree in Electrical and Computer Engineering
in the Graduate College of
The University of Iowa

May 2012

Thesis Supervisor: Professor Gary E. Christensen

ABSTRACT

Image registration plays an important role in pulmonary image analysis. Accurate image registration is a challenging problem when the lungs have deformation with large distance. Registration results estimate the local tissue movement and are useful for studying lung mechanical quantities. In this thesis, we propose a new registration algorithm and a registration scheme to solve lung CT matching problems. Approaches to study lung functions are discussed and presented through a practical application.

The overall objective of our project is to develop image registration techniques and analysis approaches to measure lung functions at high resolution. We design a nonrigid volumetric registration algorithm to catch lung motion from a pair of intra-subject CT images acquired at different inflation levels. This registration algorithm preserves both parenchymal tissue volume and vesselness measure, and is regularized by a linear elasticity cost. Validation methods for lung CT matching are introduced and used to evaluate the performance of different registration algorithms. Evaluation shows the feature-based vesselness constraint can efficiently improve the registration accuracy around lung boundaries and in the base lung region. Meanwhile, a new scheme to solve complex registration problem is introduced utilizing both surface and volumetric registration. The first step of this scheme is to register the boundaries of two images using surface registration. The resulting boundary displacements are extended to the entire ROI domains using the Element Free Galerkin Method (EFGM)

based on weighted extended B-Splines (WEB-Splines). These displacement fields are used as initial conditions for the tissue volume- and vessel- preserving non-rigid registration over the object domain. Both B-Splines and WEB-Splines are used to parameterize the transformations. Our algorithms achieve high accuracy and provide reasonable lung function maps. The mean errors on landmarks, vessel locations, and fissure planes are on the order of 1 mm (sub-voxel level).

Furthermore, we establish methods based on registration derived transformation to analyze mechanical quantities and measure regional lung function. The proposed registration method and lung function measurement are applied on a practical application to detect mechanical alternations in the lung following bronchoalveolar lavage, which achieves satisfactory results and demonstrates the applicability of our proposed approaches.

Abstract Approved: _____

Thesis Supervisor

_____

Title and Department

_____

Date

MECHANICAL ANALYSIS OF LUNG CT IMAGES USING NONRIGID

REGISTRATION

by

Kunlin Cao

A thesis submitted in partial fulfillment of the
requirements for the Doctor of Philosophy
degree in Electrical and Computer Engineering
in the Graduate College of
The University of Iowa

May 2012

Thesis Supervisor: Professor Gary E. Christensen

Graduate College
The University of Iowa
Iowa City, Iowa

CERTIFICATE OF APPROVAL

—————————————————

PH.D. THESIS

———————————

This is to certify that the Ph.D. thesis of

Kunlin Cao

has been approved by the Examining Committee for the
thesis requirement for the Doctor of Philosophy degree
in Electrical and Computer Engineering at the May 2012
graduation.

Thesis Committee: ————————————————————

    Gary E. Christensen, Thesis Supervisor

    ————————————————————

    Joseph M. Reinhardt

    ————————————————————

    Madhavan L. Raghavan

    ————————————————————

    Xiaodong Wu

    ————————————————————

    Punam K. Saha

ACKNOWLEDGEMENTS

ABSTRACT

Image registration plays an important role in pulmonary image analysis. Accurate image registration is a challenging problem when the lungs have deformation with large distance. Registration results estimate the local tissue movement and are useful for studying lung mechanical quantities. In this thesis, we propose a new registration algorithm and a registration scheme to solve lung CT matching problems. Approaches to study lung functions are discussed and presented through a practical application.

The overall objective of our project is to develop image registration techniques and analysis approaches to measure lung functions at high resolution. We design a nonrigid volumetric registration algorithm to catch lung motion from a pair of intra-subject CT images acquired at different inflation levels. This registration algorithm preserves both parenchymal tissue volume and vesselness measure, and is regularized by a linear elasticity cost. Validation methods for lung CT matching are introduced and used to evaluate the performance of different registration algorithms. Evaluation shows the feature-based vesselness constraint can efficiently improve the registration accuracy around lung boundaries and in the base lung region. Meanwhile, a new scheme to solve complex registration problem is introduced utilizing both surface and volumetric registration. The first step of this scheme is to register the boundaries of two images using surface registration. The resulting boundary displacements are extended to the entire ROI domains using the Element Free Galerkin Method (EFGM)

based on weighted extended B-Splines (WEB-Splines). These displacement fields are used as initial conditions for the tissue volume- and vessel- preserving non-rigid registration over the object domain. Both B-Splines and WEB-Splines are used to parameterize the transformations. Our algorithms achieve high accuracy and provide reasonable lung function maps. The mean errors on landmarks, vessel locations, and fissure planes are on the order of 1 mm (sub-voxel level).

Furthermore, we establish methods based on registration derived transformation to analyze mechanical quantities and measure regional lung function. The proposed registration method and lung function measurement are applied on a practical application to detect mechanical alternations in the lung following bronchoalveolar lavage, which achieves satisfactory results and demonstrates the applicability of our proposed approaches.

TABLE OF CONTENTS

LIST OF TABLES

LIST OF FIGURES

CHAPTER 1
INTRODUCTION

1.1 Project Introduction and Specific Aims

The role of the respiratory system is to provide gas exchange. Human lungs are the essential respiratory organs. Lung tissue ventilation depends on the complex interrelationships between the lungs, rib cage, diaphragm, and abdomen. Many lung diseases, such as lung cancer and chronic obstructive pulmonary disease, alter the material properties of the lung tissue and mechanical behavior of the respiratory system, thus altering local and global region ventilation. Therefore, there is a great interest in measuring regional lung ventilation, assessing lung tissue material properties, and observing the associated biomechanical behavior of the respiratory system for disease detection and tracking. These studies help provide a better understanding of the normal and abnormal lung.

Image registration is used to find the spatial mapping that brings two images into alignment. Registration algorithms designed for matching 4D lung scans or two 3D scans acquired at different inflation levels can catch the temporal changes in position and shape of the region of interest. Accurate registration results can be used to estimate lung motion and analyze lung mechanics regionally.

The overall objective of this proposal is to develop accurate image registration techniques and derive mechanical measurements to reveal lung functions at high resolution. According to this objective, the following aims are proposed:

- Aim 1: Develop nonrigid registration algorithms and scheme to match lung CT images with large distance.

- Aim 2: Validate and evaluate performance of different image registration methods.

- Aim 3: Analyze mechanical properties based on registration derived transformation.

- Aim 4: Demonstrate pulmonary mechanical changes with the application of lung following bronchoalveolar lavage (BAL).

1.2   Background

1.2.1   Respiratory Physiology and Lung Anatomy

Respiratory is important because human body needs oxygen in the air to create energy. The primary function of respiratory system is to obtain oxygen for use by body's cells and eliminate carbon dioxide that cells produce. When breathed in through the nose and mouth, fresh air is pulled through the trachea and into the lungs. From the trachea, the air moves through two bronchus. A complex system of much smaller bronchioles branch out from each bronchi and carry oxygen to the millions of tiny air sacs called alveoli. These small sacs have very thin walls that are full of blood vessels. The walls are thin enough such that the oxygen in the air can pass through them to enter bloodstream and travel to cells in the whole human body. In this way, oxygen is breathed in to reach body cells during the inspiration process. On the other hand, during the exhaling process, the byproduct of body cells work -

carbon dioxide is expelled with breaths and blown out of the lungs [118].

The anatomical features of the respiratory system include airways, lungs, and the respiratory muscles. Molecules of oxygen and carbon dioxide are passively exchanged between the gaseous external environment and the blood as the lungs expand and contract during the respiratory cycle [6]. The lung tissue consists of bronchi, bronchioles, blood vessels, alveoli and interstitium. It is the major place conducting gas exchanges. Human lungs consist of left and right lungs, and the right lung is slightly larger than the left lung. The lungs are further divided into five lobes; two for left and three for right. The left lung is divided into the left upper lobe (LUL) and left lower lobe (LLL), and they are separated by an oblique fissure. The right lung is divided into the right upper lobe (RUL), right middle lobe (RML) and right lower lobe (RLL). RUL and RML are separated by a horizontal fissure, while RML and RLL are separated by an oblique fissure. Each lung is invested by a delicate serous membrane - pleura. The pleura is a closed sac, which covers the surface of the lung and dips into the fissures between different lobes.

1.2.2 Lung Capacity and Function Change

Lung capacities and lung volumes refer to the volume of air associated with different phases of the respiratory cycle. Different lung capacities are illustrated in Figure 1.1. Some important lung capacities are defined as follows.

- **Tidal Volume (TV)** is the volume of air that is inhaled or exhaled in a single normal, resting breath.

- **Vital capacity (VC)** is the maximum volume of air that a person can exhale from the lungs after maximum inhalation, which can be measured with a spirometer. In combination with other physiological measurements, the vital capacity can help make a diagnosis of underlying lung disease.

- **Residual Volume (RV)** is the amount of gas remaining in the lung at the end of a maximal exhalation.

- **Total Lung Capacity (TLC)** is the amount of gas contained in the lung at the end of a maximal inhalation. It is composed of VC and RV. The total lung capacity depends on the person's age, height, weight, sex, and normally ranges between 4 to 6 L.

- **Functional Residual Capacity (FRC)** is the volume of air present in the lungs, specifically the parenchyma tissues, at the end of passive expiration.
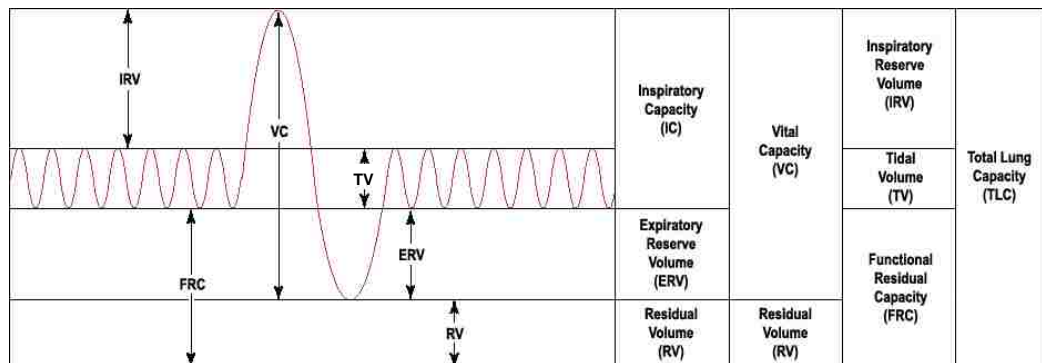
Figure 1.1: Illustration of lung capacity measurements [1].

Pulmonary diseases may change the tissue material and thus change the mechanical properties of parenchymal tissues. An example of obstructive pulmonary diseases, emphysema, is a long-term, progressive disease of the lungs that primarily causes shortness of breath. In people with emphysema, the tissues necessary to support the physical shape and function of the lungs are destroyed [90]. Since the destruction of alveoli makes these air sacs unable to hold their functional shape upon exhalation, emphysema is characterized by loss of tissue elasticity (increased compliance). Another example of restrictive pulmonary diseases, idiopathic pulmonary fibrosis (IPF), is a chronic, progressive form of lung disease characterized by fibrosis of the supporting framework (interstitium) of the lungs [39]. The pulmonary fibrosis increase the lung tissue thickness and stiffness (reduced compliance), which leads to increased lung elastic recoil [88].

Therefore, pulmonary diseases cause tissue material change, which results to its mechanical function change from normal tissue. Based on this fact, finding effective methods to understand ventilation patterns of lung parenchyma and quantify the regional lung mechanical function is desirable to help disease diagnosis, tracking and radiotherapy planning [29].

1.2.3   Existing Methods for Measuring Lung Function

Various attempts have been made to study lung functions. Invasive methods such as using surgically implanted markers to study lung mechanical functions have been discussed. Hoffman et al. have used percutaneously inserted apical and

basal lung markers to estimate the regional pleural surface expansile forces in intact dogs [56]. Hubmayr et al. have tracked the movement of implanted intraparenchymal metallic markers to study the distribution of regional lung volume during static deflation from TLC to FRC in supine and prone anesthetized dogs [67]. Robertson et al. have used fluorescent microspheres (FMS) and intravenous injection of radioactive microspheres to produce high-resolution maps of regional ventilation in mechanically ventilated pigs [95]. Although these approaches help study lung ventilation functions on animals, it is not suitable to apply these invasive methods on human subjects.

Nuclear medicine imaging such as single photon emission computed tomography (SPECT) and positron emission tomography (PET) provides three-dimensional images of the distributions of radionuclides that have been inhaled or injected into the lungs. By using radionuclides with short half-lives, the radiation exposure of the subject can be kept small. By following the evolution of the distributions of radionuclides in gases or compounds that participate in lung function, information about diverse lung functions such as regional ventilation, perfusion, inflammation can be inferred [52]. Thus PET has the ability to reveal lung functions in vivo. However, since nuclear images are acquired across several respiratory cycles, the applications of nuclear medicine imaging are largely constrained by low spatial resolution.

Proton magnetic resonance imaging (MRI) is limited to some extent by low proton density in the lung parenchyma as well as inherent magnetic field inhomogeneities in the chest. The introduction of MRI of hyperpolarized noble gases has led to various functional imaging of pulmonary ventilation distribution and dynam-

ics [83, 117, 55, 38]. Helium (He^3) and xenon (Xe^{129}) are common marker gases for lung studies. MRI avoids the concern about ionizing radiation. But it has shortcomings that the signal from airway walls is insufficient and visualization of the lung tissues is difficult except on those large airways.

Standard CT imaging has been commonly used to help diagnose and evaluate lung diseases because it can provide high-resolution images of the lung structures. But it is static and we can not assess lung ventilations from a single CT image. Another imaging modality which is able to directly assess lung function is xenon-enhanced CT (Xe-CT). It measures regional ventilation by observing the gas wash-in and wash-out rate on serial CT images [79, 112, 19]. But Xenon gas inhaled in the body may bring side effects to people, and Xe-CT imaging is expensive due to special equipment requirement. Also, its axial coverage is limited to a few slices at a time due to the high temporal resolution requirement. Using modern multi-detector scanners, the Z-axis coverage of Xe-CT imaging ranges from about 2.5 to 12 cm currently, which is insufficient compared to the typical z-axis extent of the human lungs that are approximately 25 cm.

Imaging allows non-invasive study of lung behavior and image registration can be used to examine the lung deformation. Some groups have utilized non-invasive imaging and image registration techniques to examine the linkage between estimates of regional lung expansion and local lung ventilation [28, 48, 47, 110, 111, 27, 91, 92, 31, 30]. Coselmon et al. used mutual information based registration to model deformation of lung CT images between exhale and inhale breathing states [28]. Guerrero

et al. used two CT images, acquired at different lung inflations, and optical flow image registration to estimate regional ventilation to identify functioning vs. non-functioning lung tissue for radiotherapy treatment planning [48, 47]. While they were able to show a close correlation with global measurements of lung ventilation, their experimental methods did not allow them to compare local estimates of lung expansion with regional lung ventilation. Sundaram and Gee used serial magnetic resonance imaging to quantify lung kinematics in statically acquired sagittal cross-sections of the lung at different inflations [110]. Using non-linear image registration, they estimated a dense displacement field from one image to the other, and from the displacement field they computed regional lung strain. But they had difficulty in validating the accuracy of the motion estimates. They showed a landmark-based validation later [111], however, they encountered the challenge of the inability to track the same point in successive images consistently. Christensen et al. used consistent image registration to match images across cine-CT sequences, and estimate rates of local tissue expansion and contraction [27]. Their measurements matched well with spirometry data, but they were not able to compare the registration-based measurements to local measures of regional tissue ventilation. Reinhardt et al. used image registration to match lung CT volumes across different levels of inflation [91, 92, 31, 30]. They calculated local specific volume changes as an index of regional ventilation, and compared specific volume change to xenon-CT based estimates of regional ventilation in sheep.

1.2.4   Pulmonary MDCT Imaging

Standard CT imaging has been used to study lung structures because it can provide high-contrast resolution of lung images [94, 61]. Differences between tissues that differ in physical density by less than 1% can be distinguished. As the CT imaging and reconstruction techniques improve, multidetector-row CT (MDCT) appears and it is now possible to image both lung structures and pulmonary functions [57] with high spatial resolution and fast acquisition speed. Anatomical information such as lungs, lobes, airway tree and vessel tree can be extracted from CT image [66, 115, 93, 114, 104]. Functional information such as regional ventilation and perfusion can be measured with the aid of dynamic imaging and contrast gas such as xenon [106, 79, 19, 41, 112, 57]. Generally, static lung CT images are scanned during breath-hold interval to minimize motion artifacts, and they reveals regional lung density patterns [59, 58]. Four-dimensional CT (4DCT) is a dynamic imaging protocol that images are acquired with respiratory gating and retrospective gating methods [73]. 4DCT is able to capture regional lung tissue movement over time and estimate ventilation [71]. In this proposal work, CT data are mainly static lung images acquired during breath-holds at well-controlled lung volumes. 4DCT are also used for method validation and evaluation.

1.2.5   Lung Image Registration

Image registration is a process of determining an optimal spatial mapping that matches images collected at different time points, or using different imaging

modalities. It is becoming a key tool in medical image analysis as one seeks to link images across modalities, across time, or between lung volumes in the use of pulmonary investigations. For example, registration can be used to determine the spatial locations of corresponding voxels in a sequence of pulmonary scans. The computed correspondences immediately yield the displacement fields corresponding with the motion of the lung between a pair of images.

The lung is composed of non-homogenous soft tissue, interlaced by branching networks of airways, arteries, and veins. Lung tissue expansion varies within the lung depending on body orientation, the direction of gravitation forces, the pattern of airway and vessel branching, disease conditions, and other factors. Since lung expansion is non-uniform, non-linear transformation models are needed to track tissue expansion across changes in lung volume.

Lung registration methods may be intensity-based (e.g., [110, 47, 22, 122]), landmark-based (e.g., [75]), feature-based, or based on a combination of these information (e.g., [68, 109, 13, 121]). Intensity-based methods can take advantage of the strong contrast between the lung parenchyma and the chest wall, and between the parenchyma and the blood vessels and larger airways. Landmark-based approaches are usually based on matching corresponding airway or vessel branchpoints. Feature-based methods may utilize airway tree and vessel tree structures, or regions with significant variation of intensity.

A number of registration algorithms on lung CT images have been proposed in the past few years. Modat et al. proposed the NiftyReg package which contains

a global and a local registration algorithm [82]. A block-matching technique is used in the global registration, as proposed by Ourselin et al. [87]. The Free-Form Deformation (FFD) algorithm is used in the local registration stage to maximize the normalized mutual information. Staring et al. proposed the algorithm including a combination of an affine as well as non-rigid transformations by maximizing the normalized correlation coefficient [108]. Han proposed a hybrid feature-constrained deformable registration method. The features are detected based on robust 3D SIFT descriptors, and then a mutual information based registration is used to match those features. The feature correspondences are used to guide an intensity-based deformable image registration which maximizes the mutual information and minimize the normalized sum of squared differences between images [51]. Song et al. proposed the algorithm which includes affine transformation and different diffeomorphic transformation by maximizing cross correlation between images [107]. Kabus et al. proposed a fast elastic registration algorithm that can be used in a multi-resolution setting. It is initialized by an affine pre-registration of the lungs followed by simultaneously minimizing of the similarity measure calculated as the sum of squared differences as well as the regularizing term based on the Navier-Lame equation [70]. The elastic regularizer assumes the lung tissue can be characterized as an elastic and compressible material.

The method by minimizing the sum of squared difference (SSD) assumes that corresponding points in both images have the same grayscale intensities. However, this is not true for the lung because the tissue density changes as the lung inflates

and deflates. CT intensity is a measure of tissue density and therefore changes as the tissue density changes. Efforts have been made to take this intensity change into consideration. Maximizing mutual information or normalized cross correlation accounts for the intensity change between CT images acquired at different inflation levels [80, 28, 82, 108, 51, 107]. Sarrut et al. [102] added a preprocessing step to artificially correct the intensity range. Gorbunova et al. [46] developed a modified SSD measure by adding total lung weight and regional volume change information to preserve lung weight globally and locally. Yin et al. [122] proposed a new similarity cost preserving the lung tissue volume and compared the new cost function driven registration method with SSD driven registration in the estimation of regional lung function. These methods have demonstrated improved registration accuracy.

Local lung expansion can be estimated by using registration to match images acquired at different levels of inflation. Tissue expansion (and thus, specific volume change) can be estimated by calculating the Jacobian determinant of the transformation field derived by image registration [92]. The tissue strain tensor is also calculated from the transformation field. Since both the Jacobian matrix and the strain tensor are formed using partial derivatives of the transformation field, it is important that the underlying registration transformation model be well-behaved with respect to these derivatives if the functional and mechanical results obtained are to be useful.

1.2.6   Lung Mechanical Analysis

Fung [42] studied mechanical properties of various living tissues and developed different material models. Constitutive equations are used to define the relationship between stress and strain for any material. In the present state, the constitutive equations for the lung tissue are known, but the associated material constants are unknown. Zeng et al. [124] measured the mechanical properties of human lung tissue in a state of biaxial tension and found a nonlinear stress-strain relationship. They fitted experimental data with a pseudo-elastic constitutive equation and identified the physical constants. Gao et al. [44] used a nonlinear strain energy function to examine the stress-strain relationship through biaxial loading experiments on lung parenchyma and found the related physical constants. In order to understand the mechanical behavior of the lung material, it is important to have a detailed analysis of the distribution of strain, stretch and other quantities in the lung.

Researchers have studied on measuring the displacement field in the lung based on image registration techniques. But methods to interpret information from displacement physiologically are still lacking. Volume change is the primary measurement for assessing lung deformation. Since the lung is composed of non-homogeneous soft tissue, lung tissue expansion varies in different lung regions [86]. Based on deformable image registration, Reinhardt et al. [92] utilized the Jacobian determinant calculated from displacement fields to quantify the local volume change. Cai et al. [12] used grid-tagged MRI to obtain a displacement field and estimate the fractional ventilation map.

However, volume change of the lung is not enough to describe the regional deformation during the respiratory process. The regional tissue deformation may also includes orientational preference, which can be captured by strain tensor and anisotropy description. Volume change and deformation anisotropy are independent quantities to describe regional lung mechanics. West [119] analyzed the distribution of regional lung tissue expansion, stresses, and surface pressures in an elastic lung-shaped model under the influence of gravity using finite element method. Rodarte [96] proposed two independent elastic constants are required to describe the lung material properties: the bulk modulus for volume change and the shear modulus for shape change. Later, Rodarte et al. [97] studied the regional lung distortion expressed by strain in dogs based on the displacement of multiple metallic markers embedded in the lung parenchyma. Cai et al. [12] also estimated principal strains of the lung using multiple-slice 2D dynamic image of grid-tagged MRI. These methods are based on region information, and do not provide dense estimates of lung mechanical quantities.

Image registration provides us dense displacements which captures the lung motion locally. In this thesis work, we propose different measurements from point-wise displacement fields to quantify the specific volume change and shape change of lung tissue. Besides, the sensitivity of the volume change measurement w.r.t. the registration error and region size is also studied to establish the measurement confidence interval.

1.3 Thesis Overview

The aim of this proposal work is to design effective image registration methods to match a pair of CT images acquired at different inflation levels. Validation and evaluation are conducted to prove the accuracy of registration algorithms. Regional lung functions such as tissue expansion and strain are estimated to reveal the lung mechanical properties. An application on clinical data helps demonstrate the usage of our methods to study pulmonary functions and lung mechanics in a regional level.

The thesis is organized as follows.

- Chapter 1 gives a brief introduction of the project and the specific aims. The background and related work of lung image registration and function estimation are also introduced.

- Chapter 2 describes the nonrigid volumetric registration method by preserving tissue volume and vesselness measure. The components of the registration algorithm are discussed in detail.

- Chapter 3 introduces some validation criterion for lung CT matching and evaluate the performances of different registration methods.

- Chapter 4 describes a new registration scheme to solve complex image matching problem utilizing both surface registration and volumetric registration. Element free Galerkin method and weighted extended B-Splines are introduced in detail. This chapter also provides the validation results of the new registration scheme.

- Chapter 5 provides some approaches to measure the lung function and reveal the lung mechanical properties regionally. Measurement sensitivity to displacement

noise and underlying region size is also discussed.

- Chapter 6 presents a practical application to study the changes of local lung function using nonrigid registration on lung CT images. The study demonstrate pulmonary mechanical alternations in the lung following bronchoalveolar lavage.

- Chapter 7 provides a general conclusion and possible future directions.

CHAPTER 2
NONRIGID REGISTRATION FRAMEWORK FOR LUNG CT IMAGES

2.1   Introduction

The lung is composed of non-homogenous soft tissue. Lung tissue expansion varies in different lung region. Since lung expansion is non-uniform, non-rid transformation are required to model the lung motion across different inflation levels. B-Spline are commonly used basis functions due to its advantages of good approximation, computational ease and localization for representing smooth functions. Therefore, we choose B-Spline to represent our nonrigid transformation.

To estimate correspondences between two lung CT images, registration using intensity information or feature information alone is not enough to provide good accuracy. We couple this information together to achieve better nonrigid registration. We assume the lung is an elastic object and constrain its deformation with an linear elasticity model. In addition, a multiresolution scheme is utilized to improve speed, accuracy and robustness of our registration algorithms. This chapter describes the design of our nonrigid volumetric registration in detail.

2.2   Data Description

For human anatomical reference, data sets from six normal human subjects will be used. Six pairs of volumetric CT data sets from six human subjects in the supine orientation collected on a Siemens Sensation 64 multi-detector CT scanner are

used in this study. Each image pair were acquired during breath-holds near functional residual capacity (FRC) and total lung capacity (TLC) in the same scanning session. Each volumetric data set was acquired at a section spacing of $0.5 \sim 0.6$ mm and a reconstruction matrix of 512×512. In-plane pixel spatial resolution was approximately 0.6 mm $\times$ 0.6 mm. The parenchyma regions in the FRC and TLC data sets were segmented using the method described in [66]. Table 2.1 lists the percentage of vital capacity (VC) for each data set. Figure 2.1 illustrates rendering of a pair of FRC and TLC data.

Table 2.1: Percentage of vital capacity (VC) for each data set.

Subject	FRC	TLC
1	21.8%	95.6%
2	30.5%	89.6%
3	26.3%	95.7%
4	11.0%	68.9%
5	25.8%	92.9%
6	26.5%	102.0%

2.3   Image Registration Framework

The goal of registration is to find the spatial mapping that aligns the moving image with the fixed image. Figure 2.2 shows the main components of the image-to-image registration framework. The input data to the registration framework are two images: one is defined as the *moving* or *template* image I_1, and the other is defined

(a)   (b)
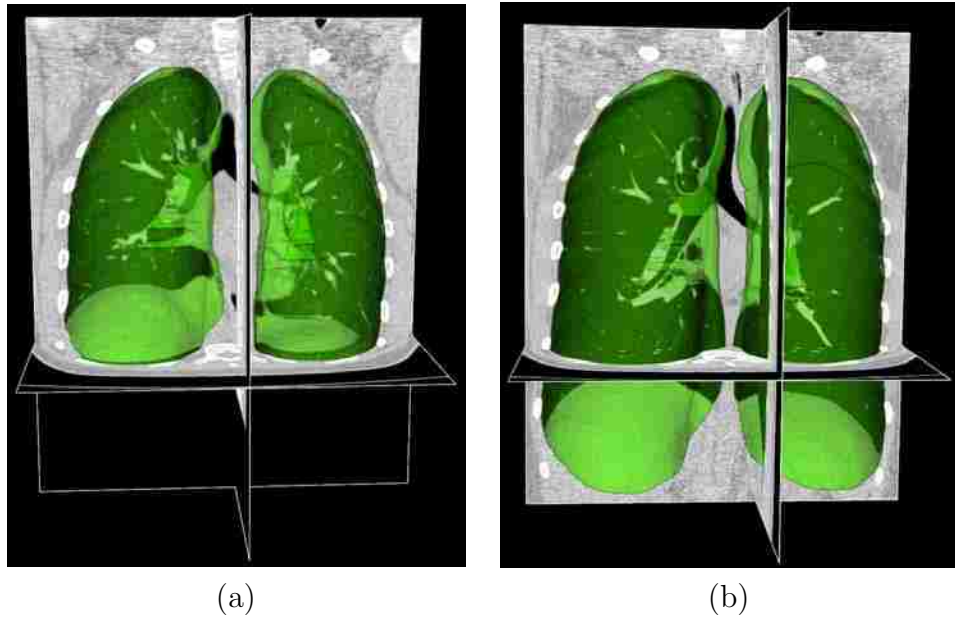
Figure 2.1: Rendering of lung CT images acquired at (a) FRC and (b) TLC.

as the *fixed* or *target* image I_2. The *transform*, **h**, is used to map points between the two images spatially. The *cost function* represents the similarity measure of how well the fixed image is aligned by the deformed moving image. This measure forms the quantitative criterion which is optimized by the *optimizer* over the search space defined by the transformation parameters. The *interpolator* is used to obtain the template image intensities at non-grid positions using information from neighboring grid positions.

For our intra-subject registration problem, the input moving and fixed images are a pair of FRC and TLC data sets from the same subject. And considering the efficiency of computation and the ease of optimization, linear interpolation is selected as the interpolation scheme. In the following, we will discuss the design of *transform*,
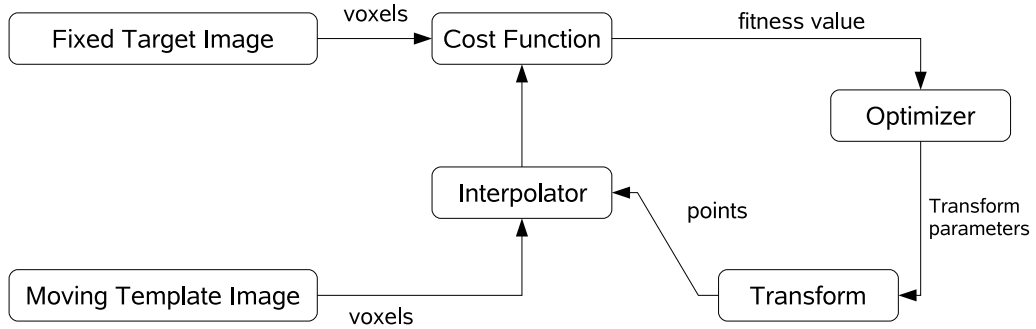
Figure 2.2: Basic components of the registration framework [123].

cost function and optimizer components in more detail.

2.4 Transformation Parameterization

The transform defines how points from the template image I_1 are mapping to their corresponding points in the target image I_2. In three dimensional space, let $\mathbf{x} = (x_1, x_2, x_3)^T$ define a voxel coordinate in the image domain of the target image I_2. The transformation $\mathbf{h}$ is a (3×1) vector-valued function defined on the voxel lattice of target image, and $\mathbf{h}(\mathbf{x})$ gives the corresponding location in template image to the point $\mathbf{x}$..

To represent the locally varying geometric distortions, the transformation can be represented by various forms of basis function, such as Fourier transform, thin-plate splines, and B-splines. B-splines are well suited for shape modeling and are efficient to capture the local nonrigid motion between two images [76, 98]. Considering the computational efficiency and accuracy requirement, the cubic B-spline based parameterization is chosen to represent the transformation.

Let $\phi_i = [\phi_x(\mathbf{x}_i), \phi_y(\mathbf{x}_i), \phi_z(\mathbf{x}_i)]^T$ be the coefficients of the i-th control point $\mathbf{x}_i$ on the spline lattice G along each direction. The transformation is represented as

$$\mathbf{h}(\mathbf{x}) = \mathbf{x} + \sum_{i \in G} \phi_i \beta^{(3)}(\mathbf{x} - \mathbf{x}_i), \tag{2.1}$$

where $\beta^{(3)}(\mathbf{x}) = \beta^{(3)}(x)\beta^{(3)}(y)\beta^{(3)}(z)$ is a separable convolution kernel. $\beta^{(3)}(x)$ is the uniform cubic B-spline basis function defined as

$$\beta^{(3)}(x) = \begin{cases} (4 - 6x^2 + 3|x|^3)/6, & 0 \le |x| < 1 \\ (2 - |x|)^3/6, & 1 \le |x| < 2 \\ 0, & |x| \ge 2 \end{cases}. \tag{2.2}$$

2.5   Cost Function Design

The cost function measures how well the target image is matched by the transformed template image. It can consist of a single metric such as a similarity measure based on intensity or geometric information, it can also be combined with other regulations and constraints depending on potential models. In our cost function design, we have three components: a intensity-based similarity metric, a feature-based similarity metric and a regularization term.

2.5.1   Intensity-based Similarity Metrics

To solve intensity-based image registration problem, people usually assume that intensities of corresponding voxels are related to each other in some way. Many criteria to construct the intensity relationship between corresponding points have been suggested as the metrics for aligning two images. Metrics such as mean square difference (MSD), correlation coefficient, mutual information, pattern intensity, and

gradient correlation [89] are proposed in [89, 62]. In our algorithm design for solving lung volume matching, three commonly used intensity-based metrics are used to register a pair of lung CT images at different inflation levels.

- *Sum of Squared Difference (SSD):*

  A simple and common metric is the sum of squared difference (SSD), which measures the intensity difference at corresponding points between two images. Mathematically, it is defined by

$$C_{\text{SSD}} = \int_{\boldsymbol{\Omega}} [I_2(\mathbf{x}) - I_1(\mathbf{h}(\mathbf{x}))]^2 \, d\mathbf{x}, \tag{2.3}$$

  where I_1 and I_2 are the template and target image intensity functions, respectively. Ω denotes the union of lung regions in target image and deformed template image. The underlying assumption of SSD is that the image intensity at corresponding points between two images should be similar. This is true when registering images of the same modality. In such cases, if the images are perfectly mapped, the corresponding intensities should be identical, which means each point of the same underlying structure has the same intensity value in the two images to be registered.

  However, considering the change in CT intensity as air inspired and expired during the respiratory cycle, the grayscale range are different within the lung region in two CT images acquired at different inflation levels. To balance this grayscale range difference, normalization of the intensities are needed. For example, a histogram matching procedure [120] can be used before SSD registra-

tion to modify the histogram of template image so that it is similar to that of target image. Figure 2.3 gives an illustration of histogram matching before SSD registration between a pair of images acquired at functional residual capacity (FRC) and total lung capacity (TLC) from a human subject. Please note that the histogram matching step is only needed for SSD registration discussed here. It is not necessary for the metrics discussed below.

(a)   (b)   (c)
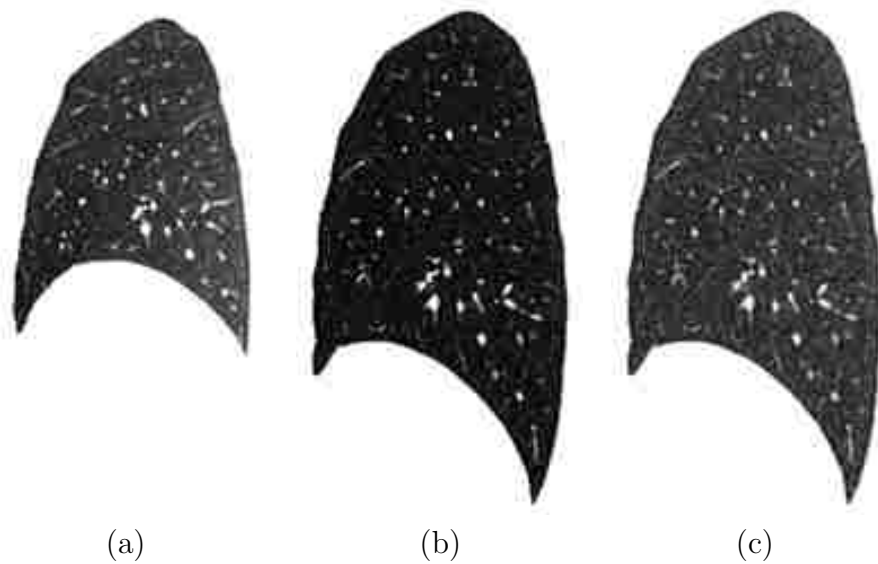
Figure 2.3: Illustration of histogram matching before SSD registration between FRC and TLC images from a human subject. (a) A sagittal slice from FRC. (b) A sagittal slice from TLC. (c) The sagittal slice of (b) after histogram modification so that its grayscale range is similar to that of (a).

- *Mutual information (MI):*

As mentioned above, CT intensity is a measure of tissue density and therefore changes as the tissue density changes during inflation and deflation. The registration problem under this circumstance is similar to the multi-modality image registration, where mutual information (MI) is well suited as the similarity metric.

Mutual information expresses the amount of information that one image contains about the other one. Analogous to the Kullback-Leibler measure, the negative mutual information cost of two images is defined as [113, 80]

$$C_{\mathrm{MI}} = -\sum_i \sum_j p(i,j) \log \frac{p(i,j)}{p_{I_1 \circ h}(i) p_{I_2}(j)}, \qquad (2.4)$$

where $p(i,j)$ is the joint intensity distribution of transformed template image $I_1 \circ h$ and target image I_2; $p_{I_1 \circ h}(i)$ and $p_{I_2}(j)$ are their marginal distributions, respectively. The histogram bins of $I_1 \circ h$ and I_2 are indexed by i and j. The experiments of MI-driven registration use 50×50 histogram bins to estimate joint distribution. Misregistration results in a decrease in the mutual information, and thus, increases the similarity cost C_{MI}. Note that the MI metric does not assume a linear relationship between the intensities of the two images.

- *Sum of Squared Tissue Volume Difference (SSTVD):*

  A recently developed similarity metric, the sum of squared tissue volume difference (SSTVD) [122], accounts for the variation of intensity in the lung CT images during respiration. This similarity criterion minimizes the local difference of tissue volume inside the lungs scanned at different pressure levels.

Assume that lung is a mixture of two materials: air and tissue/blood (non-air). Then the Hounsfield units (HU) in lung CT images is a function of tissue and air content. From the HU of CT lung images, the regional tissue volume and air volume can be estimate following the air-tissue mixture model by Hoffman et al. [60]. The tissue volume V in a voxel at position $\mathbf{x}$ can be estimated as

$$V(\mathbf{x}) = v(\mathbf{x})\frac{HU(\mathbf{x}) - HU_{air}}{HU_{tissue} - HU_{air}} = v(\mathbf{x})\beta(I(\mathbf{x})), \quad (2.5)$$

where $v(\mathbf{x})$ is the volume of voxel $\mathbf{x}$. Similarly, the air volume V' in a voxel can be estimated as

$$V'(\mathbf{x}) = v(\mathbf{x})\frac{HU_{tissue} - HU(\mathbf{x})}{HU_{tissue} - HU_{air}} = v(\mathbf{x})\alpha(I(\mathbf{x})). \quad (2.6)$$

$\alpha(I(\mathbf{x}))$ and $\beta(I(\mathbf{x}))$ are introduced for notational simplicity, and $\alpha(I(\mathbf{x})) + \beta(I(\mathbf{x})) = 1$. In this work, it is assumed that $HU_{air} = -1000$ and $HU_{tissue} = 0$. Then

$$\alpha(\mathbf{x}) = \frac{-HU(\mathbf{x})}{1000}, \quad \beta(\mathbf{x}) = \frac{HU(\mathbf{x}) + 1000}{1000}, \quad (2.7)$$

At location $\mathbf{x}$, let $I_1(\mathbf{x})$ and $I_2(\mathbf{x})$ be the intensity values (HU), $v_1(\mathbf{x})$ and $v_2(\mathbf{x})$ be the voxel volumes, and $V_1(\mathbf{x})$ and $V_2(\mathbf{x})$ be the tissue volumes in the voxel of images I_1 and I_2, respectively. Then the intensity similarity metric SSTVD is defined as [122]

$$
\begin{aligned}
C_{\text{SSTVD}} &= \int_{\Omega} \left[V_2(\mathbf{x}) - V_1(\mathbf{h}(\mathbf{x})) \right]^2 d\mathbf{x} \\
&= \int_{\Omega} \left[v_2(\mathbf{x})\beta(I_2(\mathbf{x})) - v_1(\mathbf{h}(\mathbf{x}))\beta(I_1(\mathbf{h}(\mathbf{x}))) \right]^2 d\mathbf{x}. \quad (2.8)
\end{aligned}
$$

The Jacobian of a transformation $J(\mathbf{h})$ estimates the local volume changes resulted from mapping an image through the deformation. Thus, the tissue volumes in image I_1 and I_2 are related by

$$v_1(\mathbf{h}(\mathbf{x})) = v_2(\mathbf{x}) \cdot J(\mathbf{h}(\mathbf{x})). \tag{2.9}$$

Substituting with Equation 2.9, Equation 2.8 can be rewritten as

$$C_{\text{SSTVD}} = \int_{\mathbf{\Omega}} \left\{ v_2(\mathbf{x}) \left[\beta(I_2(\mathbf{x})) - J(\mathbf{h}(\mathbf{x}))\beta(I_1(\mathbf{h}(\mathbf{x}))) \right] \right\}^2 d\mathbf{x} \tag{2.10}$$

2.5.2 Feature-based Similarity Metrics

Feature information extracted from the intensity image is important to help guide the image registration process. During the respiration cycle, blood vessels keep their tubular shapes and tree structures. Therefore, the spatial and shape information of blood vessels can be utilized to help improve the registration accuracy. Blood vessels have larger HU values than that of parenchyma tissues. The intensity difference between parenchyma and blood vessels can effectively help intensity-based registration. However, as the blood vessel branches, the diameter of vessel becomes smaller and smaller. The small blood vessels are difficult to see because of their low intensity contrast. Therefore, grayscale information of the small vessels give almost no contribution to help guide the intensity-based registration. In order to better utilize the information of blood vessel locations, we do not use their grayscales directly, but rather use the vesselness measure (VM) computed from intensity image.

Sum of Squared Vesselness Measure Difference (SSVMD): The vesselness measure is based on the analysis of eigenvalues of the Hessian matrix of image intensity.

The eigenvalues, which are geometrically interpreted as principal curvatures, can be used to indicate the shape of underlying object. In 3D lung CT images, isotropic structures such as parenchyma tissues (dark) are associated with three similar non-zero positive eigenvalues while tubular structures such as blood vessels (bright) are associated with one negligible eigenvalue and two similar non-zero negative eigenvalues [40]. Ordering the eigenvalues of a Hessian matrix by magnitude $|\lambda_1| \leq |\lambda_2| \leq |\lambda_3|$, the Frangi's vesselness function [40] is defined as

$$
F(\lambda) = \begin{cases} \left(1 - e^{-\frac{R_A^2}{2\alpha^2}}\right) \cdot e^{\frac{-R_B^2}{2\beta^2}} \cdot \left(1 - e^{-\frac{S^2}{2\gamma^2}}\right) & \text{if } \lambda_2 < 0 \text{ and } \lambda_3 < 0 \\ 0 & \text{otherwise} \end{cases}
\tag{2.11}
$$

with

$$
R_A = \frac{|\lambda_2|}{|\lambda_3|}, \qquad R_B = \frac{|\lambda_1|}{\sqrt{|\lambda_2 \lambda_3|}}, \qquad S = \sqrt{\lambda_1^2 + \lambda_2^2 + \lambda_3^2},
\tag{2.12}
$$

where R_A distinguishes between plate-like and tubular structures, R_B accounts for the deviation from a blob-like structure, and S differentiates between tubular structure and noise. α, β, γ control the sensitivity of the vesselness measure. The experiments in this proposal use $\alpha = 0.5$, $\beta = 0.5$, and $\gamma = 5$.

The Hessian matrix is computed by convolving the intensity image with second and cross derivatives of the Gaussian function. For a multiscale analysis, the response of the vesselness filter will achieve the maximum at a scale which approximately matches the size of vessels to detect. Therefore, the final vesselness measure is estimated by computing Equation 2.11 for a range of scales and selecting the maximum response:

$$
F = \max_{\sigma_{min} \leq \sigma \leq \sigma_{max}} F(\lambda).
\tag{2.13}
$$

Here σ is the standard deviation of the Gaussian function [37].

The vesselness image is rescaled to [0, 1] and can be considered as a probability-like estimate of vesselness features. Larger vesselness value indicates the underlying object is more likely to be a vessel structure, as shown in Figure 2.4. The sum of squared vesselness measure difference (SSVMD) is designed to match similar vesselness patterns in two images. Given $F_1(\mathbf{x})$ and $F_2(\mathbf{x})$ as the vesselness measures of images I_1 and I_2 at location $\mathbf{x}$ respectively, this new cost function [14, 15, 16] is formed as

$$C_{\text{SSVMD}} = \int_{\boldsymbol{\Omega}} [F_2(\mathbf{x}) - F_1(\mathbf{h}(\mathbf{x}))]^2 . \tag{2.14}$$

Mismatch from vessel to tissue structures will result a larger SSVMD cost.

(a) (b)

Figure 2.4: The vesselness images calculated from lung CT grayscale images. (a) A transverse slice of FRC data. (b) The vesselness measure of slice in (a). Vesselness measure is computed in multiscale analysis and rescaled to [0, 1].

2.5.3 Elastic Regularization

Enforcing constraints on the transformation helps generate physiologically more meaningful registration results. Continuum mechanical models such as linear elasticity [22, 23, 24] and viscous fluid [23, 25] can be used to regularize the transformation. A common way to constraint the deformation is applying a differential operator on the transformation and formulating an additive cost term in the objective cost function [98, 22, 68, 21, 45, 76, 77, 45, 116, 103]. In our registration algorithms, a linear-elastic constraint is used to regularize the displacement fields $\mathbf{u}$ where

$$\mathbf{u} = \mathbf{h}(\mathbf{x}) - \mathbf{x}. \tag{2.15}$$

This regularization term is formed as

$$C_{\mathrm{REG}}(u) = \int_{\Omega} ||L\mathbf{u}(\mathbf{x})||^2 d\mathbf{x} \tag{2.16}$$

L can be any nonsingular linear differential operator [81]. Here the linear elasticity operator L is formed as $L\mathbf{u}(\mathbf{x}) = -\alpha\nabla^2\mathbf{u}(\mathbf{x}) - \beta\nabla(\nabla \cdot \mathbf{u}(\mathbf{x})) + \gamma\mathbf{u}(\mathbf{x})$ where $\nabla = \left[\frac{\partial}{\partial x_1}, \frac{\partial}{\partial x_2}, \frac{\partial}{\partial x_3}\right]$ and $\nabla^2 = \nabla \cdot \nabla = \left[\frac{\partial^2}{\partial x_1^2} + \frac{\partial^2}{\partial x_2^2} + \frac{\partial^2}{\partial x_3^2}\right]$.

Using linear elasticity differential operator can help smooth the transformation, and help eliminate abrupt changes in the displacement fields. The linear elasticity operator is used in this work to help avoid the transformation from folding onto itself. However, it can not prevent the Jacobian of the transformation from going negative, i.e., destroying the image topology under the transformation [26]. Additional constraints on the displacement fields is needed and introduced later in the optimization method.

2.5.4   Total Cost Function and Parameter Evaluation

Finally, the total cost is defined as a linear combination of the intensity-based metric, vesselness measure preserving metric and Laplacian constraint

$$C_{\text{TOTAL}} \;=\; \rho C_{\text{INTENSITY}} + \chi C_{\text{SSVMD}} + \gamma C_{\text{REG}}. \tag{2.17}$$

$C_{\text{INTENSITY}}$ can be one of the three intensity-based similarity metrics: C_{SSD}, C_{MI} or C_{SSTVD}. Constants ρ, χ and γ are weights to adjust significance of the three terms.

Six pairs of CT image volumes were used to investigate the effect of varying the parameters used in the consistent image registration algorithm. As described in 2.2, these CT data sets were collected from different individuals using the same CT machines and the same scan parameters. We designed experiments to discover the good parameter settings on intensity-based metric C_{SSTVD}, feature-based metric C_{SSVMD}, and regularization term C_{REG}. Parameter settings of registration using other intensity-based metrics, eg. C_{SSD}, C_{MI} can be tuned in the same way.

Table 2.2 and Figure 2.5 shows the results of 20 experiments for CT-to-CT registration, as the weighting values χ and γ are varied. The cost values are averaged on results from six subjects. The weight for the SSTVD cost ρ is set to one for all of the experiments. The values of χ and γ range from 0 to 2 and 0 to 0.5 for these experiments, respectively.

Experiments CT01 correspond to unconstrained estimation in which the transformation are estimated only according to the intensity similarity cost. These experiments produced the relatively worse registration results as evident by the large values of C_{SSTVD}, C_{SSVMD}, and C_{REG} in the respective tables.

Table 2.2: Registration experimental parameters and cost values.

Experiment	SSVMD	REG	χ	γ	C_{SSTVD}	C_{SSVMD}	C_{REG}	Jacobian min	Jacobian 1/max
CT01	No	No	0.0	0	34118	57879	172605	0.25	0.11
CT02	No	Yes	0.0	0.05	32751	49291	111770	0.38	0.12
CT03	No	Yes	0.0	0.1	32059	46156	86780	0.44	0.13
CT04	No	Yes	0.0	0.2	33571	44504	63530	0.50	0.13
CT05	No	Yes	0.0	0.4	36736	44853	43827	0.58	0.15
CT06	Yes	No	0.5	0	31288	29492	153068	0.33	0.12
CT07	Yes	Yes	0.5	0.05	30275	28611	110499	0.40	0.12
CT08	Yes	Yes	0.5	0.1	30074	27326	87990	0.44	0.13
CT09	Yes	Yes	0.5	0.2	31194	26812	63612	0.50	0.14
CT10	Yes	Yes	0.5	0.4	33426	28111	46094	0.57	0.14
CT11	Yes	No	1	0	30873	23963	161940	0.36	0.11
CT12	Yes	Yes	1	0.05	29991	22560	115510	0.40	0.11
CT13	Yes	Yes	1	0.1	29923	22328	94784	0.44	0.13
CT14	Yes	Yes	1	0.2	30956	22261	70079	0.49	0.13
CT15	Yes	Yes	1	0.4	32830	23576	50549	0.57	0.15
CT16	Yes	No	1.5	0	31713	20082	181465	0.34	0.11
CT17	Yes	Yes	1.5	0.05	31046	20059	124563	0.39	0.12
CT18	Yes	Yes	1.5	0.1	30871	20270	103340	0.43	0.12
CT19	Yes	Yes	1.5	0.2	31407	20024	76930	0.49	0.13
CT20	Yes	Yes	1.5	0.4	32982	21413	55329	0.56	0.14
CT21	Yes	No	2	0	32532	18907	192035	0.34	0.11
CT22	Yes	Yes	2	0.05	31566	18396	134317	0.39	0.12
CT23	Yes	Yes	2	0.1	31709	18742	109223	0.41	0.12
CT24	Yes	Yes	2	0.2	32172	19218	82619	0.49	0.13
CT25	Yes	Yes	2	0.4	33252	19946	59525	0.56	0.14
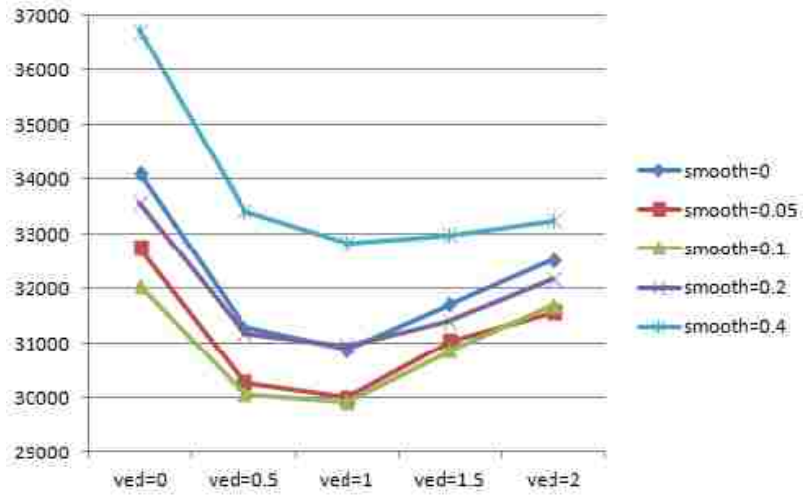
(a) SSTVD Cost
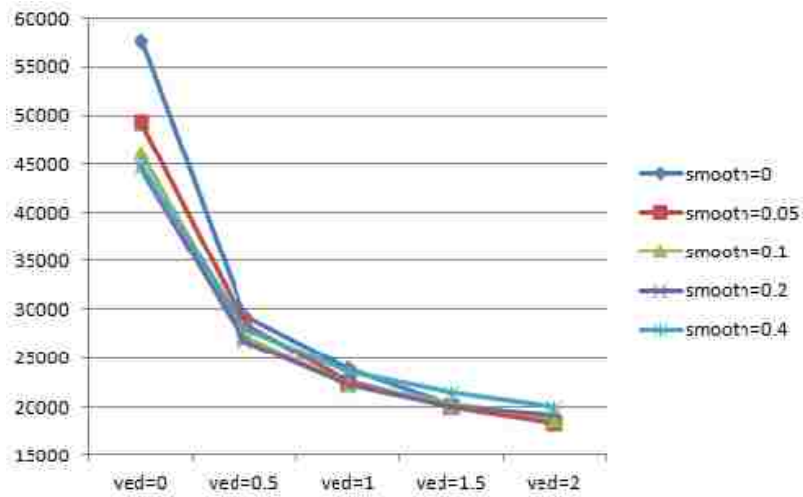
(b) SSVMD Cost
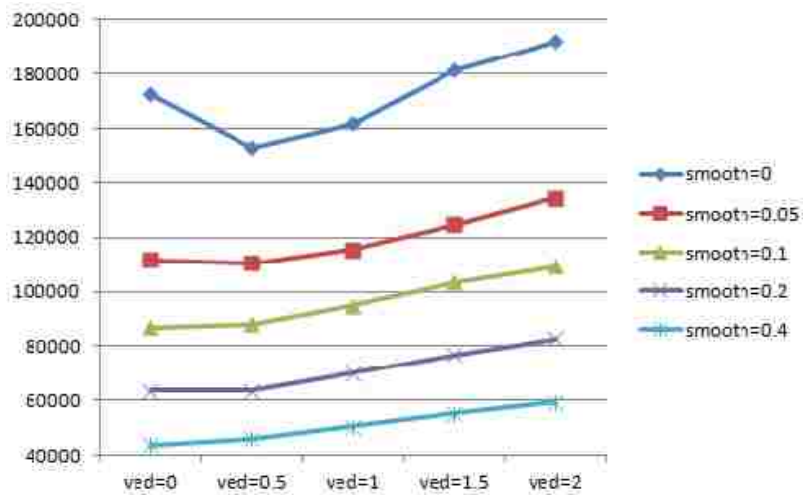
(c) REG Cost

Figure 2.5: Plots of (a) SSTVD, (b) SSVMD, and (c) REG costs using different parameter settings. Data are averaged through results from six subjects.

Experiments CT02, CT03, CT04 and CT05 demonstrate the effect of estimating the transformations without minimizing feature similarity cost while varying γ the weight of the linear elastic cost. Minimizing linear elastic cost is good for optimizing the other two similarity costs C_{SSTVD} and C_{SSVMD}, as we can see from Figure 2.5 (a) and (b). γ values larger than 0.2 is not recommended since it may cause the C_{SSTVD} increases dramatically. Increasing the constraint weights results in the similarity cost to increase indicating a worse intensity match between images.

Experiments CT06, CT11, CT16, and CT21 demonstrate the effect of using vesselness similarity metric without enforcing the linear elasticity constraint. The C_{SSVMD} values for these experiments are much lower than the previous cases since they are being minimized. The intensity similarity costs C_{SSTVD} are also decreased using registration with vesselness constraint, especially when χ is in the range of [0.5, 1].

The remaining experiments show the effect of jointly estimating the transformations while varying the weights on both the vesselness similarity cost and the linear elasticity constraint. These experiments show that it is possible to find a set of parameters that produce better results using both constraints than only using one or none.

The optimal set of parameters should be chosen to provide a good intensity match and vesselness match, while producing less amount of spatial distortion as measured by an acceptable level of linear elastic cost. From the experiments, we may get the idea that $\chi = 0.5 - 1$ and $\gamma = 0.05 - 0.1$ is good for minimizing the three

costs at the same time. In this thesis work, all results are generated using parameters setting of $\rho = 1, \chi = 1$, and $\gamma = 0.1$.

2.6 Optimization Method

Most registration algorithms can employ standard optimization ways to solve the problems and find the good transformation. There are several existing methods in numerical analysis such as the partial differential equation (PDE) solvers to solve the elastic and fluid transformation, steepest gradient descent method, conjugate gradient method etc.

In our registration algorithm design, the similarity cost functions are optimized using a limited-memory, quasi-Newton minimization method with bounds (L-BFGS-B) [11] algorithm which is well suited for optimization with a high dimensional parameter space. This algorithm allows bound constraints on the independent variables.

The bound constraints are applied on B-Spline coefficients so that it is sufficient to guarantee the local injectivity (one-to-one property) of transformation [18], i.e., the transformation maintains the topology of two images. According to their analysis, the displacement fields are locally injective all over the domain if B-Spline coefficients satisfy the condition that $\phi_x \leq \delta_x/K, \phi_y \leq \delta_y/K, \phi_z \leq \delta_z/K$, where $\delta_x, \delta_y, \delta_z$ are the B-Spline grid sizes along each direction, and K is a constant approximately equal to 2.479772335. As we can see from Table 2.2, the Jacobian values are all positive in all 20 experiments. This indicates that our registration produces transformations with

image topology preserved.

2.7 Multiresolution Scheme

A spatial multiresolution procedure from coarse to fine is used in the registration in order to improve speed, accuracy and robustness. The basic idea of multiresolution is that registration is first performed at a coarse scale where the images have much fewer pixels, which is fast and can help eliminate local optima. The resulting spatial mapping from the coarse scale is then used to initialize registration at the next finer scale. This process is repeated until registration is performed at the finest scale.

In the experiments, the spatial multiresolution strategy proceeds from low to high resolution is designed to start at one-eighth the spatial resolution and increase by a factor of two until the full resolution is reached. Meanwhile, a hierarchy of B-Spline grid spacings from large to small is also used. The finest B-spline grid space used in the experiments is 4 mm. An example multiresolution scheme design for minimizing the total cost function is listed in Table 2.3. The image spatial resolution and B-spline grid spacing are refined alternatively.

Table 2.3: An example multiresolution scheme.

Image resolution	B-Spline grid size	Max. Iteration
1/8	128 mm $\longrightarrow$ 64 mm	400
1/4	32 mm $\longrightarrow$ 16 mm	400
1/2	16 mm $\longrightarrow$ 8 mm	100
1	8 mm $\longrightarrow$ 4 mm	40

Each experiment that ran for 8 levels took approximately 1 hour to run on a computer using a single 2.27GHz, Intel(R) Xeon(R) CPU E5520 processor. Figure 2.6 lists the cost values in each iteration. At 1/8 and 1/4 image resolutions, registration speed is fast and we allow it to run more iterations. The algorithm in the two steps usually stops before reaching the maximum iterations due to the total cost change is nominal between consecutive iterations. Global shapes are matched during these two levels. At 1/2 image resolution, the inner structures get clearer and are aligned roughly. Registration at full resolution will further adjust the local structures matching. During the whole registration procedure, the Jacobian values are ensured to be positive.

2.8 Summary

In order to study the lung mechanics, we firstly develop a nonrigid, regularized, intensity-based and feature-based registration scheme. It is suitable for registering lung CT scans and catching lung motions. The nonrigid registration structure has been established using C++. Different intensity-based similarity metrics have been implemented. These intensity similarity metrics are used to minimize intensity difference (after histogram matching), preserve tissue volume, and maximize mutual information between two images.

The feature-based similarity metric is proposed to match the similar vessel patterns. It can help guide lung CT registration and improve matching accuracy effectively. The linear elastic operator is applied on displacements to constrain the
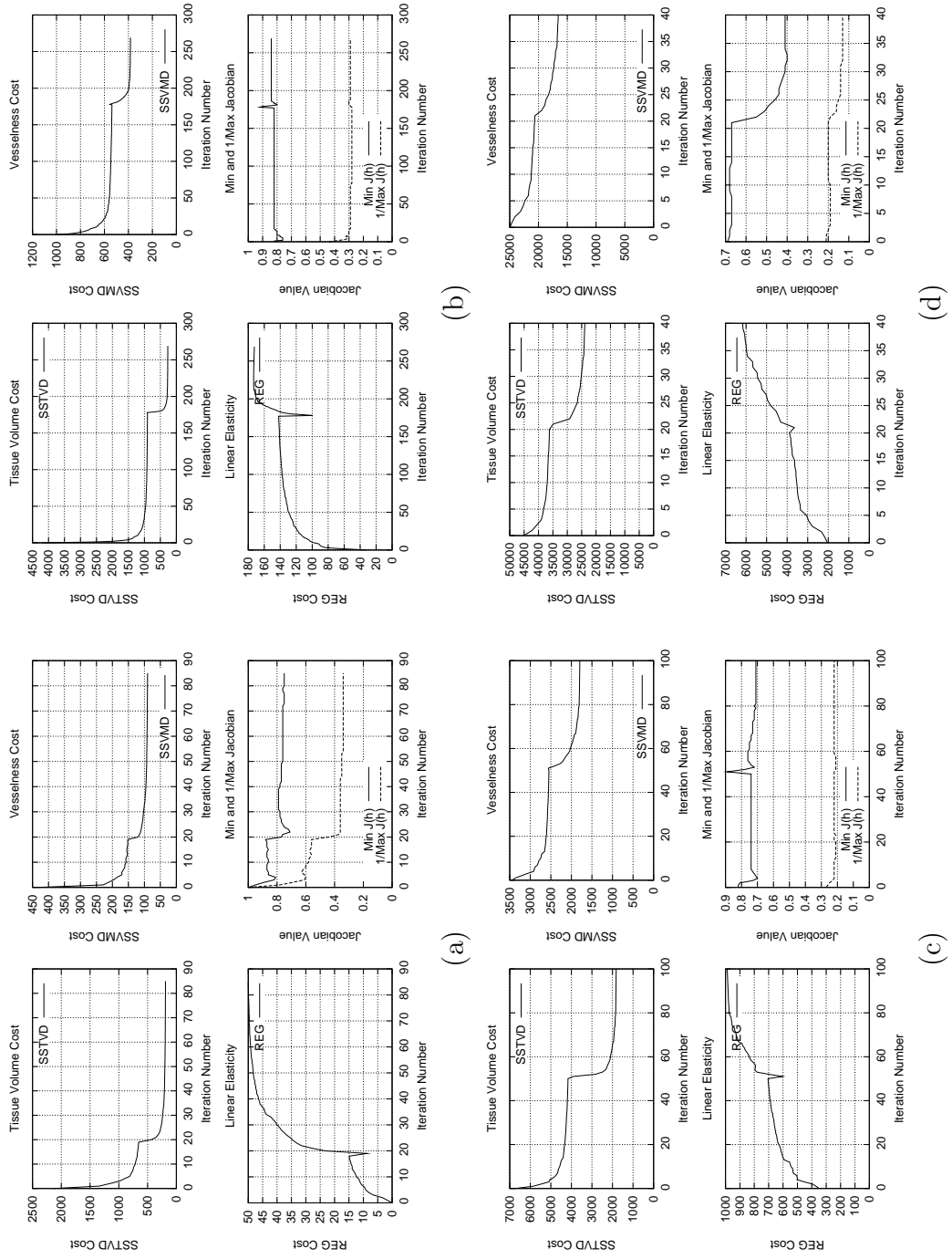
Figure 2.6: Statistics associated with experiment CT13.

transformation. It is used to smooth out displacement field along each direction and also allows coupling deformation in different directions. The weighting effects for three costs are studied and appropriate parameter settings are selected to provide good intensity and vesselness matching with acceptable level of linear elastic cost. The optimization method uses limited memory, which is suitable for optimization in a high dimensional parameter space. Hard constraints on the B-Spline coefficients is used to guarantee our registration provides one-to-one mappings. Finally, we use a multiresolution scheme from coarse to fine to improve program speed and robustness.

In the next chapter, we will validate the matching accuracy of our registration method, and evaluate the improvement by using our novel feature-based metric through various aspects.

CHAPTER 3
VALIDATE AND EVALUATE THE PERFORMANCE OF
DIFFERENT IMAGE REGISTRATION METHODS

3.1 Introduction

Evaluation of image registration is an important task to quantify the performance of registration algorithms. Due to the absence of a "gold standard" to judge a registration algorithm, various evaluation methods are needed to validate the performance of image registration with respect to different properties of transformations. In this specific aim, we will develop a thorough scheme of evaluation methods related to lung image registration.

In the process of developing lung registration algorithms, different evaluation methods are considered, designed and used to validate the effectiveness of our registration algorithms. Focusing on lung CT image registration, we can use following image features and information to measure our registration accuracy:

- Features extracted from image, such as landmarks, airway and vessel trees, lobar segmentations, fissures, region boundaries and object volumes;

- Transformation properties, such as zero singularities, reproducibility and consistency between different methods;

- Extraneous information that are not used in the registration data, such as ventilation map estimated from Xenon-CT image;

All the features and image information mentioned above provide different perspectives for registration accuracy measurement. Some of the evaluation methods are discussed

in [15]. In this chapter, we will discuss some validation methods and results in detail.

3.2   Data Sets and Experiment Setting

The validation and evaluation experiments will use data sets from six normal human subjects, which is described in section 2.2. For some specific evaluation methods, images of animals will be used, such as sheep to provide a functional reference. The acquisition of those data sets will be described in the corresponding section.

In order to validate our registration accuracy and evaluate how the vesselness metric affects the registration algorithm results, we perform six registrations using different similarity metrics on each pair of data sets for comparison. They are three basic registration methods driven by only intensity-based similarity metrics, and three registration methods with feature-based similarity metric SSVMD build in. These metrics are listed in Table 3.1.

Table 3.1: Similarity metrics of different registration methods.

Without SSVMD	C_{SSD}	C_{MI}	C_{SSTVD}
With SSVMD	$C_{\text{SSD}} + C_{\text{SSVMD}}$	$C_{\text{MI}} + C_{\text{SSVMD}}$	$C_{\text{SSTVD}} + C_{\text{SSVMD}}$

3.3   Landmark Matching Accuracy

Landmarks are point features of an object. Anatomical landmarks have biological meaning. In the lung CT image, the vascular tree and airway tree can be

extracted by intensity contrast, and their bifurcations can then be identified. Points at bifurcations of vessel and airways provide good candidates for landmarks.

The distance between corresponding landmarks is called the landmark error. Landmark error is calculated by the Euclidean distance from its estimated to real position, as shown in Figure 3.1.
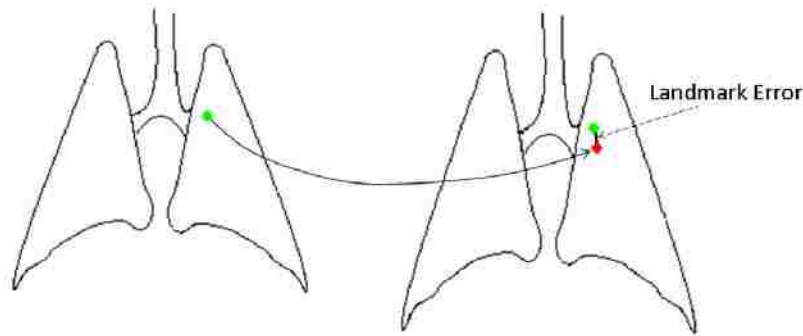
Figure 3.1: Illustration of the landmark error calculation. The green landmark in one image should correspond to the green point in the second image. Registration maps the green landmark to the position marked as red in the second image. The distance between the predicted position (red point) and the true position (green point) is defined as landmark error.

The Euclidean distance between registration-predicted landmark position and its true position is defined as

$$d = ||\mathbf{p}_k - \mathbf{h}(\mathbf{q}_k)||, \tag{3.1}$$

where $\mathbf{p}_k$ and $\mathbf{q}_k$ are the location of landmark k on template image I_1 and target

image I_2, respectively. $\mathbf{h}$ is the Eulerian transformation generated from registration process. For two sets of N corresponding landmarks $P = \{\mathbf{p}_1, \mathbf{p}_2, \mathbf{p}_3, ..., \mathbf{p}_M\}$ and $Q = \{\mathbf{q}_1, \mathbf{q}_2, \mathbf{q}_3, ..., \mathbf{q}_M\}$, the mean landmark error after matching is defined as

$$\mu(P, \mathbf{h}(Q)) = \frac{1}{N} \sum_{k=1}^{N} d(\mathbf{p}_k, \mathbf{h}(\mathbf{q}_k)), \tag{3.2}$$

and the variance is defined as

$$\sigma(P, \mathbf{h}(Q))) = \frac{1}{N} \sum_{k=1}^{N} (d(\mathbf{p}_k, \mathbf{h}(\mathbf{q}_k)) - \mu(P, \mathbf{h}(Q)))^2. \tag{3.3}$$

For each scan pair of FRC and TLC data, a well-distributed set of distinctive landmark points are defined in the target and template images. The landmarks in FRC image are firstly selected as the bifurcations of the segmented vessel tree [104, 105]. To remove the small branches of the vessel tree, the segmented vessel tree is processed by binary erosion followed by dilation with a rectangular structure element of 1.5 mm $\times$ 1.5 mm $\times$ 0.5 mm and connected component process is performed to eliminate the small disconnected pieces which have volume smaller than 10 mm^3. A 3D skeletonization is then applied and the vessel bifurcation is detected by using the local topological numbers showing the bifurcation as the curve-curve junction. A semi-automatic system [84] is used to guide the observer to find the landmarks in the TLC image with their corresponding voxels in the FRC image.

The landmarks are well dispersed throughout the lungs and lie in the regions of good grayscale contrast. An example of the point distribution is shown in Figure 3.2. The corresponding landmarks (green points) are selected at vessel-tree branch points on FRC and TLC scans of one subject. An expert selected over 100 landmark pairs

for each of the six subjects.

<center>(a)</center> <center>(b)</center>
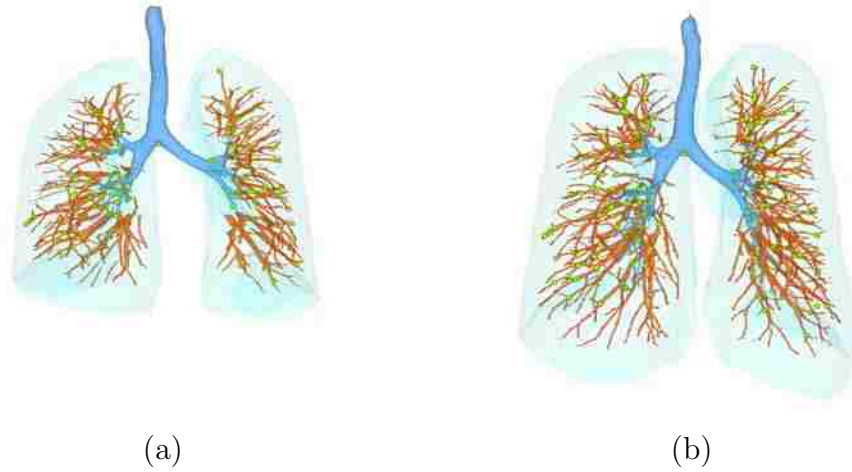
Figure 3.2: Distribution of landmarks (green points) selected at vessel-tree branch points on (a) FRC, and (b) TLC scans of one subject.

The original average landmark error is 27.40 ± 14.37 mm with a maximum landmark error of 72.79 mm (after rigid registration). Table 3.2 shows the mean and standard deviation of landmark errors through all six subjects after using different registration methods. Figure 3.3 shows the box-plot of landmark errors. We noticed that adding the SSVMD cost function reduced the mean landmark errors of the three basic registration methods. Landmarks with large errors, shown as outliers in the box-plot, are aligned much better when SSVMD is used.

Analyzing the landmark errors derived from SSTVD only and SSTVD + SSVMD methods, we observe that large error reduction mostly happens with land-

Table 3.2: Landmark errors (mm) through six subjects.

	SSD		MI		SSTVD	
	Avg.	Max	Avg.	Max	Avg.	Max
Without SSVMD	0.95 ± 1.29	15.97	1.05 ± 1.85	16.72	0.92 ± 1.28	15.38
With SSVMD	0.71 ± 0.46	4.56	0.68 ± 0.46	5.11	0.71 ± 0.45	4.1
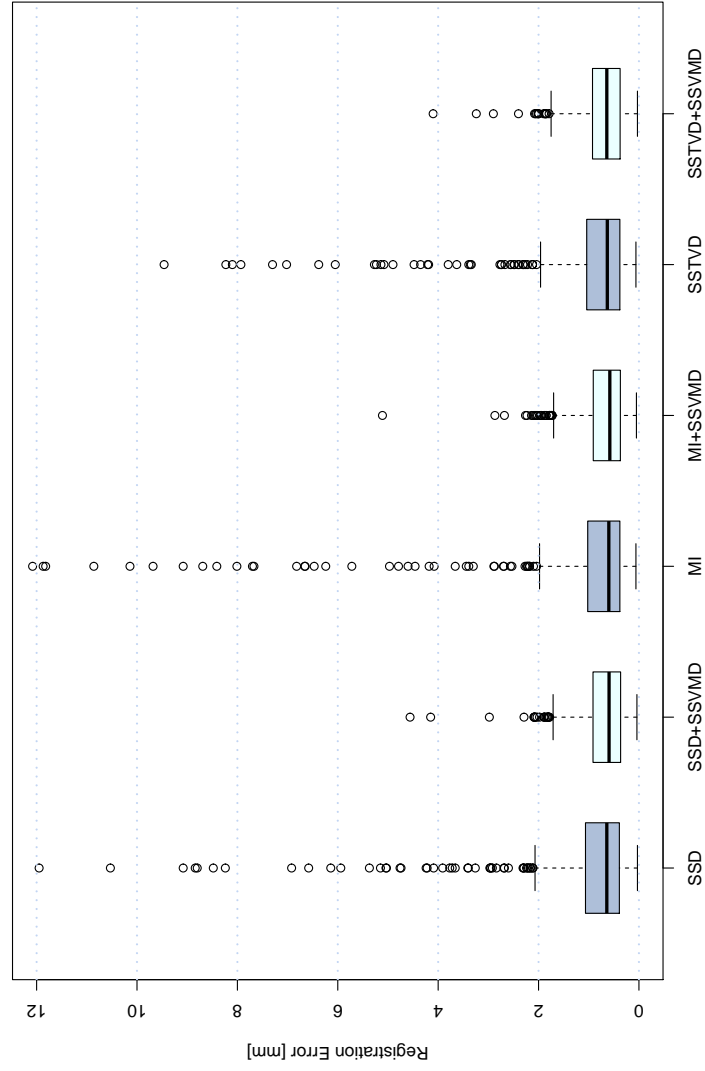
Figure 3.3: Box-plot of landmark errors through six subjects after using six registration methods. Results from methods with SSD, MI and SSTVD metic along contain outliers beyond the error range.

marks located in the regions near diaphragm. Figure 3.4 shows the distribution of the true landmark locations (green points) on vascular tree and their estimated locations (red points) for one subject. It can be seen that for landmarks located in the base of lung (yellow rectangular region), the distances from their estimated positions to the true positions are decreased after adding the new SSVMD cost while the distances for landmarks in upper lung regions do not change much.

(a)   (b)
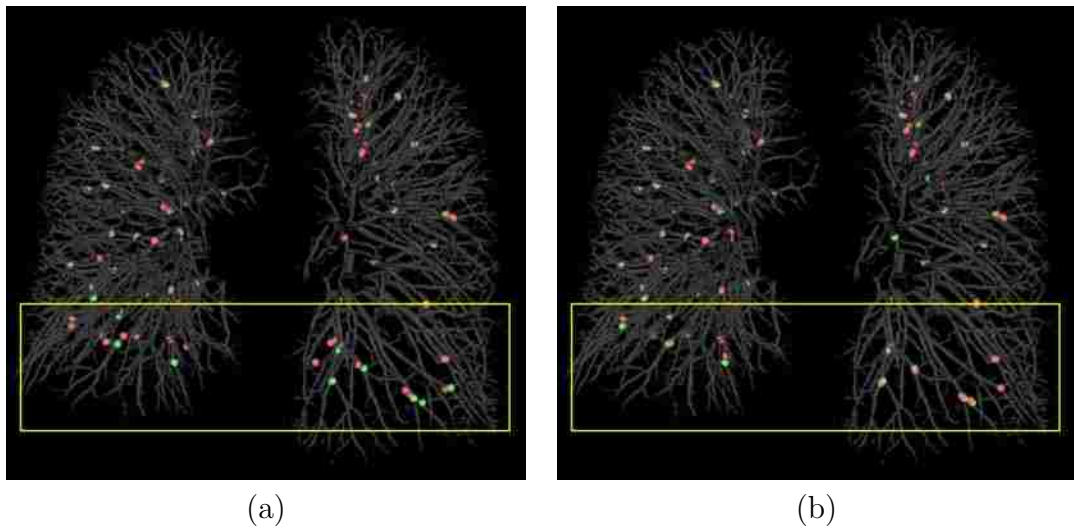
Figure 3.4: Distribution of the true landmark locations (green points) and the transformation estimated locations (red points) on bifurcations of vascular trees. The estimated locations are calculated using transformations resulted from (a) SSTVD method and (b) SSTVD + SSVMD method.

3.4   Vessel Matching Accuracy

Vessels in the lung form tree structures and they keep their tubular shape and tree structures during the respiratory process. The vascular tree provide us rich spatial and shape information in parenchyma regions. Therefore, evaluating the alignment on vessel trees is an important perspective to validate matching accuracy at the lung feature level.

The registration accuracy on the vessel tree are evaluated by vessel matching distance which is calculated as the distance between a point on the target vessel tree and its closet point on warped template vessel tree. Mathematically, this distance can be stated as the vessel positioning error (VPE)

$$VPE(\mathbf{x}) = \min_{\mathbf{y} \in V_2} d(\mathbf{x}, \mathbf{h_{12}}(\mathbf{y})) \tag{3.4}$$

for a given point $\mathbf{x}$ in V_1, where V_1 (V_2, resp.) is the set of all points in the vessel trees extracted from image I_1 (I_2, resp.) and $d(\cdot)$ defines the Euclidean distance.

The vessel positions used for validation are segmented using vessel segmentation algorithm [104]. Figure 3.5 shows the distance map on FRC vessel tree from one subject after using six different registration methods. Large errors between the deformed source and target vessel trees are reduced after adding the SSVMD constraint. It reflects the fact that SSVMD constraint helps improve matching accuracy over all three basic methods on small vessels, around lung boundaries and in the region near diaphragm. The reason for this is that blood vessels in those regions are usually small and have low intensity contrast, and thus they contribute little to conventional intensity similarity criteria. The vesselness measurement enhances blood

vessel information and strengthens contribution of small vessels to registration process when using the SSVMD similarity metric. Although SSD method (after histogram matching) has smaller mean landmark error than SSTVD method, its accuracy in the inferior region of the lung is not as good as that of SSTVD method. The reason may be that SSTVD cost function contains a local Jacobian factor which can constrain incorrect displacement and capture large deformation in the region near diaphragm with higher accuracy. However, after adding SSVMD on the three basic methods, the vessels are generally aligned better and the resulting vessel matching distance maps (Figure 3.5 right column) look similar.

The original average vessel positioning error is 12.65 ± 14.18 mm (after rigid registration). Table 3.3 shows the vessel positioning errors (mm) through six subjects after using different registration methods. The average errors and standard deviations are all decreased after adding vesselness constraint. The reason is that we enhance the vessel contribution to the total cost by adding the vesselness similarity metric. Therefore, the vessel locations are better aligned with SSVMD.

Table 3.3: Vessel positioning errors (mm) through six subjects.

	SSD	MI	SSTVD
Without SSVMD	0.80 ± 0.70	0.82 ± 0.70	0.67 ± 0.57
With SSVMD	0.70 ± 0.58	0.68 ± 0.56	0.60 ± 0.49
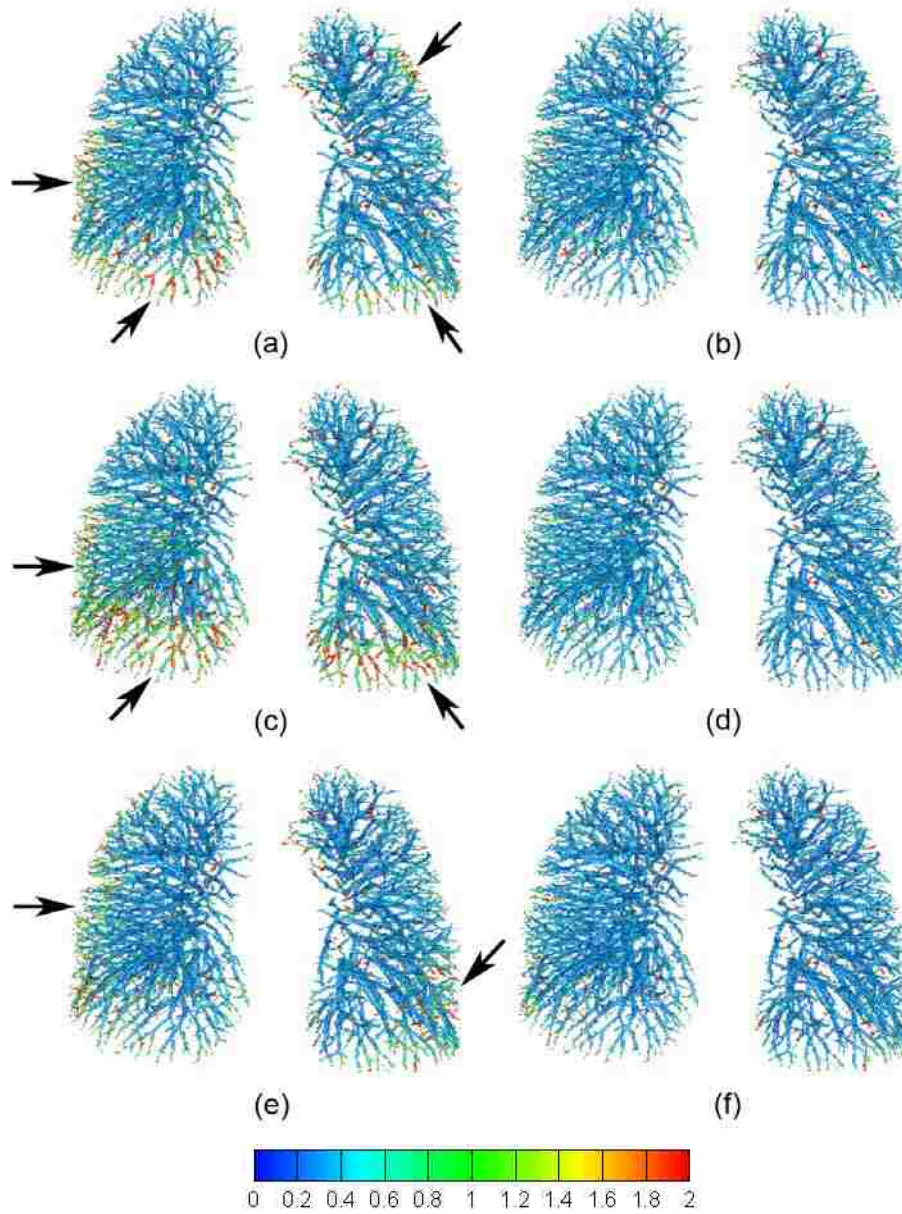
Figure 3.5: Vessel matching distance (mm) on target vessel tree. Results are generated from six registration methods: (a) SSD, (b) SSD + SSVMD, (c) MI, (d) MI + SSVMD, (e) SSTVD, and (f) SSTVD + SSVMD. Arrows denote regions of large discrepancies between the deformed source and target vessel trees. Note that the errors in these regions were reduced after adding the SSVMD constraint to the registration algorithms.

3.5   Fissure Alignment Distance

The human lungs are divided into five independent compartments which are called lobes. Lobar fissures are the division between adjacent lung lobes. The left lung is divided into the left upper (LUL) and left lower (LLL) lobes, separated by the oblique fissure. The right lung is partitioned into the right upper lobe (RUL), middle lobe (RML), and the lower lobe (RLL), separated by the oblique and horizontal fissures. The division of lung lobes are shown in Figure 3.6. Since fissures represent important physical boundaries within the lungs, their alignment result is included as an evaluation category.
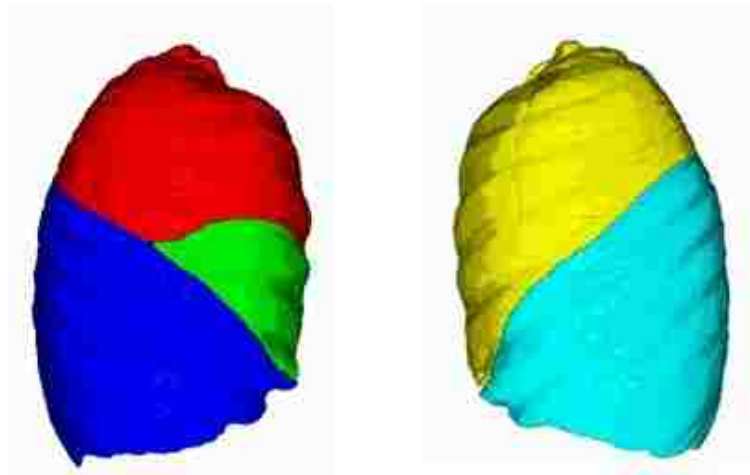
Figure 3.6: Illustration of lobe division [2].

To evaluate the fissure alignment, the fissure positioning error (FPE) is used and determined by comparing the distance between the transformed fissure and target

fissure. The FPE is defined as the minimum distance between a point on the deformed fissure and the closest point on the corresponding target fissure. Mathematically, this metric can be stated as

$$FPE(\mathbf{x}) = \min_{\mathbf{y} \in F_2} d(\mathbf{x}, \mathbf{h_{12}}(\mathbf{y})) \tag{3.5}$$

for a given point $\mathbf{x}$ in F_1, where F_1 (F_2, resp.) is the set of all points in the fissure in image I_1 (I_2, resp.) and $d(\cdot)$ defines the Euclidean distance.

For each scan pair of FRC and TLC data, an automatic lobe segmentation algorithm [115] is used to segment the parenchyma regions into five different lobes. The lobar segmentation begins with automatic lung, airway tree, and vessel tree segmentation [66, 114, 104]. A watershed transform, applied to a distance map derived from the original CT image and the vessel segmentation, provides an initial lobar segmentation. The lobar surfaces are then refined using a 3D optimal surface detection that divides the lungs at the fissure surfaces. Three fissures are identified where the lobe segmentations touched each other.

Figure 3.7 illustrates a visual comparison of registration results from two methods. (a) and (b) show the sagittal views of the same slice number in FRC and TLC datasets. (c) and (d) show the slices of deformed images from FRC to TLC using SSTVD method (top) and SSTVD + SSVMD method (bottom). (e) and (f) show the absolute grayscale differences between the target image and the deformed image $|I_2(\mathbf{x}) - I_1(\mathbf{h}(\mathbf{x}))|$ resulted from SSTVD method (top) and SSTVD + SSVMD method (bottom). The absolute difference images are rescaled to [0, 1]. Bright differences in (e) denote poor alignment of the vessels. Notice that the vessels are matched well

using SSVMD since there are no bright differences in (f). Comparing the absolute intensity difference image, it can be noticed that adding SSVMD helps improve registration accuracy in the lung regions near the thoracic cage. Since the air content in FRC and TLC data are different, the deformed image from FRC data has a different grayscale range compared with target TLC image. As a result, the overall difference in lung region is not zero. The Jacobian map shown in Figure 3.7 (g) and (h) reflect the underlying tissue expansion patterns using SSTVD method (top) and SSTVD + SSVMD method (bottom). In comparison, Jacobian in (h) has less distortion in the region inside the red rectangular.

The original average fissure positioning error is $9.20 \pm 7.94\ mm$ (after rigid registration). The mean and standard deviation of fissure positioning error over all three fissures after using six registration methods are shown in Table 3.4. The average fissure positioning error across six subjects is 9.20 mm and is decreased to around 1.50 mm and 1.00 mm without and with SSVMD cost, respectively. The fissure positioning matching accuracy is improved by about 30% after adding SSVMD cost. This indicates that the SSVMD not only helps match vessel structures, but also helps improve registration accuracy in other regions, such as positions on the fissure planes.

Table 3.4: Fissure positioning errors (mm) through six subjects.

	SSD	MI	SSTVD
Without SSVMD	1.53 ± 1.87	1.48 ± 1.78	1.41 ± 1.61
With SSVMD	1.09 ± 0.88	1.05 ± 0.79	1.00 ± 0.69
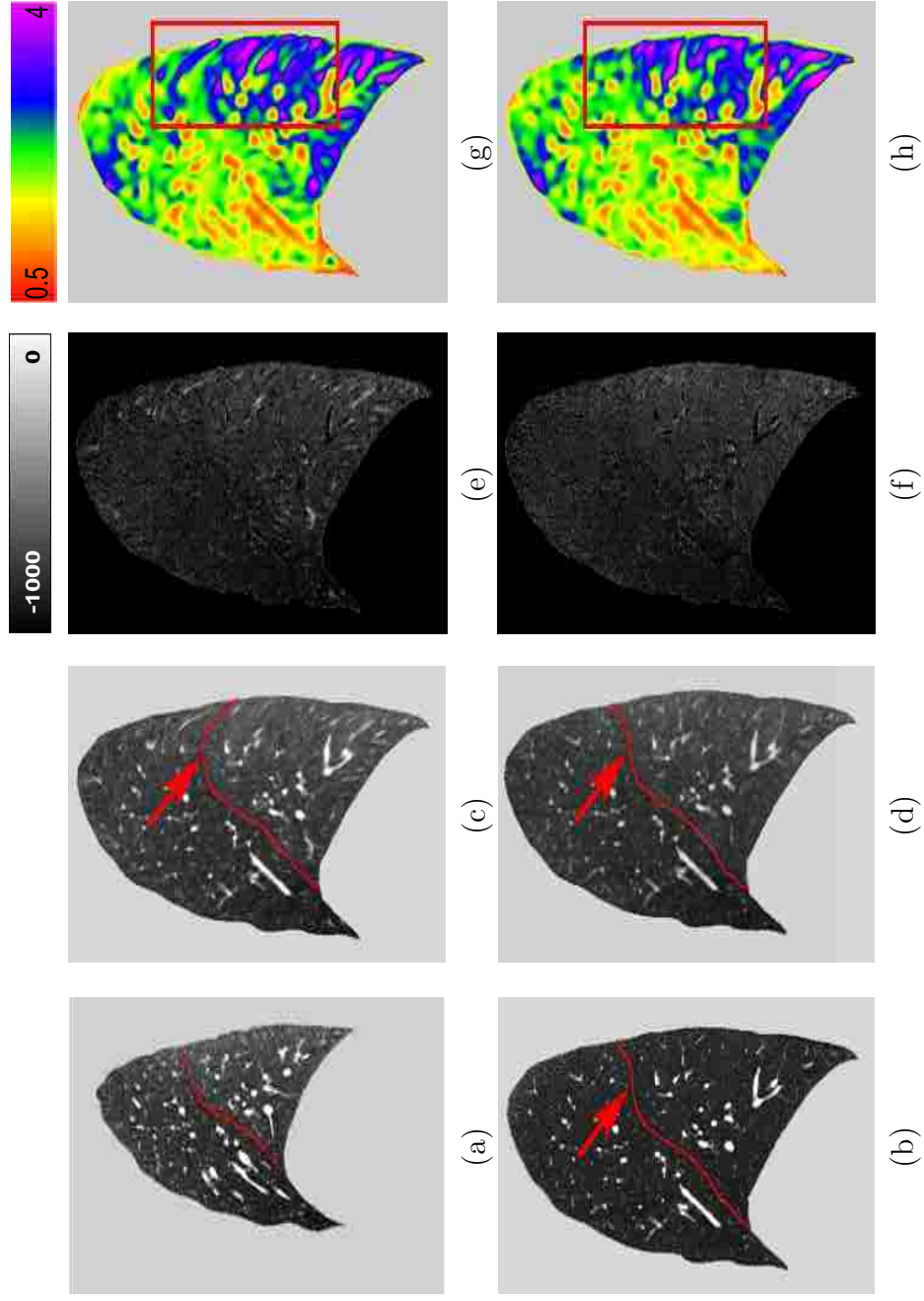
Figure 3.7: The visual comparison of registration results using two methods. (a) and (b) show the sagittal views in FRC and TLC datasets. column 2 − 4 show the deformed image, difference image, and Jacobian maps from SSTVD (top) and SSTVD+SSVMD (bottom), respectively.

For reference, the FPE on each fissure is listed in Table 3.5. The original average FPE on the left oblique fissure, the right oblique fissure and the right horizontal fissure are 9.30 ± 8.49 mm, 7.86 ± 5.40 mm, and 10.71 ± 9.37 mm. As we noticed, using vessel preserving metric improves accuracy on each fissure. The right horizontal fissure has the largest deformation of the three, and mismatching on this plane get most correction with SSVMD constraint.

Table 3.5: Fissure positioning errors (mm) on three fissures planes.

Left oblique fissure	SSD	MI	SSTVD
Without SSVMD	1.55 ± 2.07	1.44 ± 1.87	1.46 ± 1.60
With SSVMD	1.07 ± 0.91	1.01 ± 0.76	0.99 ± 0.68

Right oblique fissure	SSD	MI	SSTVD
Without SSVMD	1.29 ± 1.21	1.34 ± 1.33	1.19 ± 0.97
With SSVMD	1.08 ± 0.85	1.05 ± 0.80	1.00 ± 0.72

Right horizontal fissure	SSD	MI	SSTVD
Without SSVMD	1.81 ± 2.18	1.70 ± 2.08	1.63 ± 2.13
With SSVMD	1.12 ± 0.86	1.11 ± 0.81	1.01 ± 0.70

3.6   Lung Segmentation Overlap

A more global feature-based registration validation approach compared to methods mentioned above is to calculate the relative overlap (RO) between the segmentations of images. The alignment of objects or regions of interests (ROIs) is one

perspective to indicate how well two images are matched.

The parenchyma regions in the FRC and TLC data sets are segmented using Hu et al. [66]. The Relative Overlap (RO) statistic is used to measure how well corresponding regions of the parenchyma agreed with each other. The RO metric is given by

$$RO(S_1 \circ \mathbf{h}, S_2) = \frac{(S_1 \circ \mathbf{h}) \cap S_2}{(S_1 \circ \mathbf{h}) \cup S_2} \tag{3.6}$$

where S_1 and S_2 are segmentations of parenchyma regions on images I_1 and I_2, respectively. $S_1 \circ \mathbf{h}$ corresponds to a segmentation transformed from image I_1 to I_2. $RO = 1$ implies a perfect segmentation matching. The relative overlap of segmentations can be evaluated on the whole parenchyma region, or subvolumes of left lung, right lung, or even on the lobe level whenever the segmentations are available.

The RO metric has several limitations for evaluating registration algorithms: it gives larger (better) values for large object compared to smaller objects; there may be biases and errors due to differences in anatomy and error in the hand segmentations; a high relative overlap does not ensure the shape of the two segmentations are close enough since this metric does not reflect the local shape difference. The RO metric is limited to measure how well two binary segmentations align, however, it can not give a measure of the inside microscopic local structure matching. Therefore, volume overlap may be considered a better global performance measure than local performance measure.

The relative overlaps (RO) of parenchyma regions through six subjects after using different registration methods are listed in Table 3.6. Before registration, the RO

is 0.50 averaged through six subjects. The changes on RO are nominal after adding vesselness constraint. Combined with observations from other evaluation results, we may conclude that the vesselness metric helps improve matching accuracy on local structures, but not on global volume overlaps.

Table 3.6: Relative overlap of lung regions through six subjects.

	SSD	MI	SSTVD
Without SSVMD	0.98	0.97	0.97
With SSVMD	0.98	0.97	0.97

3.7 Evaluation Using Transformation Properties

Jacobian of the Transformation: Good matching accuracy on the feature locations does not guarantee that the parenchymal tissues are correctly aligned. In order to reveal the lung tissue deformation pattern, the Jacobian determinant of the transformation field derived by image registration is used to estimate the local tissue deformation [92].

The Jacobian determinant (often simply called the Jacobian) [10, 26, 22] is a measurement to estimate the pointwise expansion and contraction during the deformation. In three-dimensional space, let $\mathbf{h}(\mathbf{x}) = [h_1(\mathbf{x}), h_2(\mathbf{x}), h_3(\mathbf{x})]^T$ be the vector-valued transformation and $\mathbf{u}(\mathbf{x}) = [u_1(\mathbf{x}), u_2(\mathbf{x}), u_3(\mathbf{x})]^T$ be the correspoing displacement deforms the template image I_1 to the target image I_2. The relation-

ship between $\mathbf{h}(\mathbf{x})$ and $\mathbf{u}(\mathbf{x})$ is shown as $\mathbf{h}(\mathbf{x}) = \mathbf{x} + \mathbf{u}(\mathbf{x})$. The Jacobian of the transformation $J(\mathbf{h}(\mathbf{x}))$ at location $\mathbf{x} = (x_1, x_2, x_3)^T$ is defined as

$$
\begin{aligned}
J(\mathbf{h}(\mathbf{x})) &= \begin{vmatrix} \frac{\partial h_1(\mathbf{x})}{\partial x_1} & \frac{\partial h_2(\mathbf{x})}{\partial x_1} & \frac{\partial h_3(\mathbf{x})}{\partial x_1} \\ \frac{\partial h_1(\mathbf{x})}{\partial x_2} & \frac{\partial h_2(\mathbf{x})}{\partial x_2} & \frac{\partial h_3(\mathbf{x})}{\partial x_2} \\ \frac{\partial h_1(\mathbf{x})}{\partial x_3} & \frac{\partial h_2(\mathbf{x})}{\partial x_3} & \frac{\partial h_3(\mathbf{x})}{\partial x_3} \end{vmatrix} \\
&= \begin{vmatrix} 1 + \frac{\partial u_1(\mathbf{x})}{\partial x_1} & \frac{\partial u_2(\mathbf{x})}{\partial x_1} & \frac{\partial u_3(\mathbf{x})}{\partial x_1} \\ \frac{\partial u_1(\mathbf{x})}{\partial x_2} & 1 + \frac{\partial u_2(\mathbf{x})}{\partial x_2} & \frac{\partial u_3(\mathbf{x})}{\partial x_2} \\ \frac{\partial u_1(\mathbf{x})}{\partial x_3} & \frac{\partial u_2(\mathbf{x})}{\partial x_3} & 1 + \frac{\partial u_3(\mathbf{x})}{\partial x_3} \end{vmatrix}.
\end{aligned} \tag{3.7}
$$

The Jacobian determinant J at a given point gives important information about the behavior of transformation $\mathbf{h}$ near that point. If the Jacobian value at $\mathbf{x}$ is zero, then $\mathbf{h}$ is not invertible near $\mathbf{x}$. A negative Jacobian indicates $\mathbf{h}$ reverses orientation, which folds the domain [26, 20]. A positive Jacobian means $\mathbf{h}$ preserves orientation near $\mathbf{x}$. Furthermore, using a Lagrangian reference frame, a Jacobian value of one corresponds to zero expansion or contraction. Local tissue expansion corresponds to a Jacobian greater than one and local tissue contraction corresponds to a Jacobian less than one. These indications of Jacobian are listed in Eq. 3.8.

$$
\begin{cases} J > 0, \text{preserve orientation} \begin{cases} J > 1, \text{local expansion} \\ \\ J = 1, \text{no deformation} \\ \\ 0 < J < 1, \text{local contraction} \end{cases} \\ \\ J = 0, \text{non-injective} \\ \\ J < 0, \text{reverse orientation} \end{cases} \tag{3.8}
$$

Rather than evaluates the alignment accuracy, the Jacobian evaluates the quality of the transformation properties. It reveals how well the transformation preserves

topology, and measures the differential lung volume change. Figure 3.8 shows the Jacobian maps resulted from six registration methods. The top row shows that the Jacobian maps generated by the three registration methods without SSVMD have a similar ventral to dorsal gradient as expected since the subjects were imaged in the supine orientation. However, the local tissue deformation patterns derived from these methods are different even in the methods pair SSD and SSTVD which have similar landmark errors as shown in Table 3.2. This is consistent with the findings that while the inter-method variability on the landmark error is small there may be discriminating difference in the Jacobian maps [69]. The Jacobian from MI method is strikingly different in the region pointed by an arrow, which may be due to the differences in convergence speed among registration methods. The Jacobian maps from SSD and SSTVD methods show more local structure in the dorsal region, but they are of different patterns, especially in the region around lung boundaries. The bottom row shows that adding the SSVMD constraint produces Jacobian images that are very similar across the three registration methods and reveal more detailed deformation patterns especially near vessel locations. Generally, vessels have smaller volume changes comparing with parenchymal tissues during breathing cycles. The three Jacobian maps produced using registration methods with SSVMD are very similar which may imply that the derived local deformation patterns are more reliable.
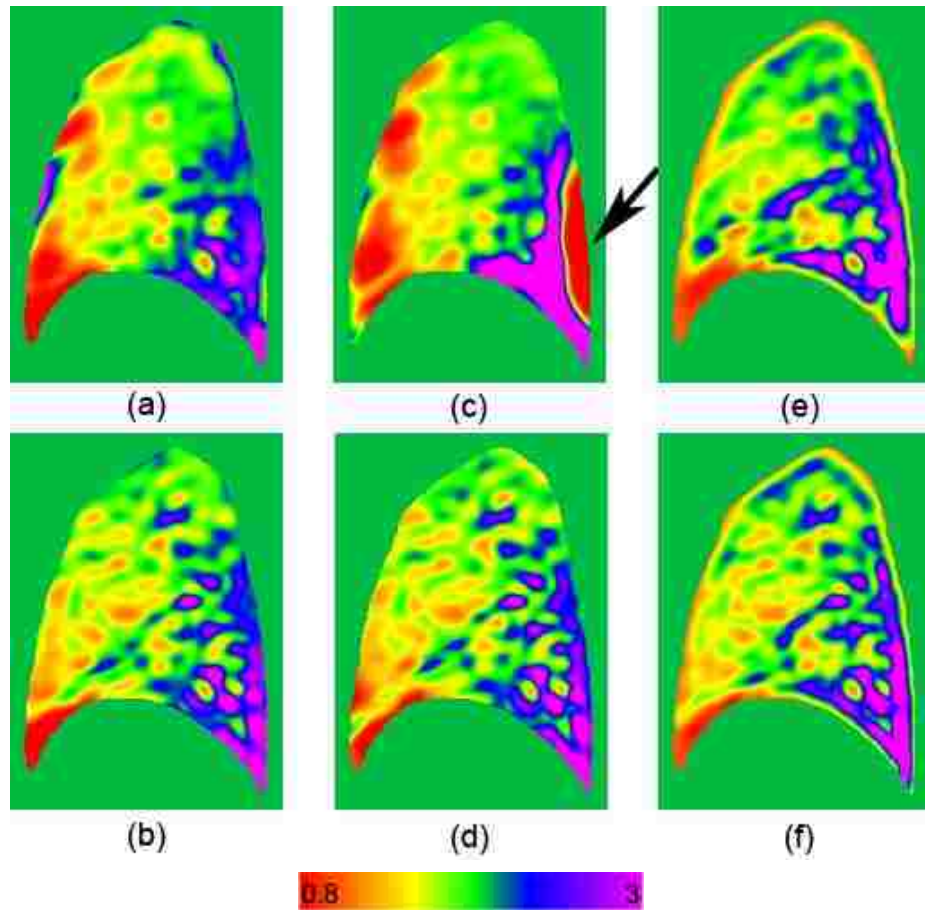
Figure 3.8: Color-coded Jacobian maps on a sagittal slice. Results are generated from six registration methods: (a) SSD, (b) SSD + SSVMD, (c) MI, (d) MI + SSVMD, (e) SSTVD, and (f) SSTVD + SSVMD. Blue and purple regions have larger lung deformation, while red and orange regions are deforming less. The arrow points to a region where Jacobian pattern is suspected to be incorrect.

3.8   Evaluation Using Extraneous Information

Correlation between Lung Expansion and Xe-CT Estimates of specific ventilation: Anatomical reference can usually provide features such as landmarks at the regions with high contrast which can be recognized by either human observer or computer algorithms. However, they are not able to provide accuracy assessment at the regions where no high contrast landmarks are available. From the registration result, we can directly calculate the registration based estimate of the regional specific ventilation (regional lung function). By comparing it with the xenon-CT based estimate of the regional specific ventilation, we are able to assess the registration accuracy in the prospect of lung function.

Our previous studies have shown that the degree of regional lung expansion is directly related to specific ventilation (sV) [92]. A good registration should produce a deformation map (Jacobian map) which has high correlation with ventilation map. In order to evaluate how each registration algorithm performs on the resulting deformation properties, and to estimate of regional lung tissue deformation, we compare lung expansion measured by the Jacobian with Xe-CT estimates of sV on lung CT data sets from one sheep.

The adult sheep is anesthetized using intravenous pentobarbital and mechanically ventilated during the experiment. CT scans are acquired with the sheep in the supine orientation and with a static protocol at 10 cm (P10) and 25 cm (P25) H_2O airway pressure. For Xe-CT studies, twelve contiguous axial locations and approximately 40 breaths are selected from the whole lung volumetric scan performed near

end-expiration. Both types of images are acquired at a reconstruction matrix of 512 $\times$ 512.

The sV is computed using the Pulmonary Analysis Software Suite 11.0 (PASS) [49]. During the Xenon gas wash-in phase of image acquisition, the Xe-CT time series data shows an exponential rise in lung density. In each ROI to be analyzed, the mean density $D(t)$ is modeled as [106]

$$D(t) = \begin{cases} D_0 & 0 \leq t < t_0 \\ D_0 + (D_f - D_0)(1 - e^{-\frac{t-t_0}{\tau}}) & t \geq t_0, \end{cases} \tag{3.9}$$

where D_0 is the density in the ROI before switching to xenon gas, D_f is the density when xenon was inspired until equilibrium, t_0 is the start time switching to xenon from room air, and τ is the model time constant. Specific ventilation (sV, ventilation per unit lung air volume in $\min^{-1}$) for each ROI was calculated as the inverse of the time constant τ, i.e., $sV = \tau^{-1}$. A bigger sV value in a ROI indicates larger density change in a time unit.

The Jacobian map is derived from P10 to P25 registration. To compare the Jacobian values with the sV, the static scan P10 was registered to the Xe-CT scan using rigid affine registration. The Jacobian and sV measurements are shown on a transverse slice in Figure 3.9. The correlation between ventilation map and Jacobian map can be utilized to validate the registration results. A higher correlation indicates a better registration.

The Jacobian map is derived from registration of images of different inflation levels (P10 to P25). To compare the Jacobian values with the sV estimates, the tar-

(a)   (b)
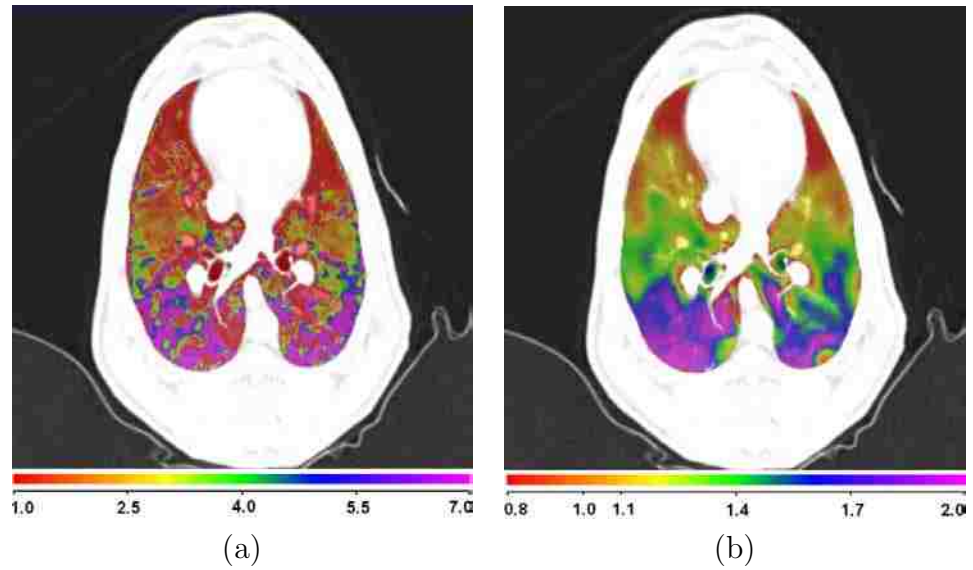
Figure 3.9: Color-coded maps showing specific ventilation and the Jacobian of transformation from sheep lung registration. The maps are overlaid on a transverse slice from the sheep lung data showing (a) specific ventilation (1/min) and (b) the Jacobian of transformation between P10 and P25. Blue and purple regions show higher ventilation in (a) and larger deformation in (b), while red and orange regions show lower ventilation in (a) and smaller deformation in (b).

get static scan P10 was registered to the Xe-CT scan using rigid affine registration. The Xe-CT data was subdivided into 30 slabs along the y (ventral–dorsal) direction. The average Jacobian within each slab was compared to the corresponding average sV measurement in the Xe-CT images. Table 3.7 shows the correlation coefficient r value between sV and Jacobian derived from six registration methods. Regional lung expansion should correlate with regional ventilation measured by Xe-CT estimates of sV. As shown in Figure 3.9, both sV and Jacobian maps show a similar ventral to dorsal gradient. High specific ventilation should correspond with large tissue expansion. Table 3.7 shows that SSVMD improves the correlation results for both SSD and MI methods. For SSTVD, there is little change in the correlation. This may result from the accurate regional model of the intensity change in SSTVD method, and it is difficult to achieve additional improvement in the case of small deformation. These results suggest that SSVMD helps generate more physiologically meaningful transformations.

Table 3.7: Correlation coefficient between sV and Jacobian.

	SSD	MI	SSTVD
Without SSVMD	0.72	0.60	0.92
With SSVMD	0.88	0.87	0.91

3.9   Summary

In this chapter, we introduce some validation methods related to lung image registration, and evaluate the lung registration results using different similarity metrics. The registration errors are small compared to the large overall deformations. It proves that our registration scheme is able to catch large lung motion between FRC and TLC using different intensity-based similarity metrics.

We demonstrate that vesselness preserving method effectively helps improve the overall registration accuracy on landmark positions, vessel structures and fissure planes. The purpose of adding this metric in registration process is that it can help correct the mismatches of small vessels and their surrounding lung tissues.

From the observation of the underlying Jacobian map, we find that methods with SSVMD constraint is shown to produce a more detailed expansion pattern for local tissue, especially near vessel locations. And adding the feature-based similarity metric SSVMD helps registration methods with different intensity-based similarity metrics to produce consistent deformation map.

In addition, adding the SSVMD constraint is shown to improve the correlation between Jacobian and specific ventilation after registration. This demonstrates that using the SSVMD constraint not only helps match vessel structures, but it also helps align corresponding parenchymal tissues providing a more reliable pattern of local lung tissue deformation.

In conclusion, the vesselness preserving constraint SSVMD helps improve registration accuracy on places with large discrepancies between images and produce

mechanically plausible results.

CHAPTER 4
BOUNDARY CONDITIONED NONRIGID REGISTRATION FRAMEWORK

4.1 Introduction

In Chapter 3, we demonstrate that we are able to match images with large distance using volumetric registration method introduced in Chapter 2. Please note that all the registrations are performed in the direction from TLC to FRC, and the displacements are defined on FRC image coordinate. This is because in discretized images, FRC data contains less information than TLC data. And optimization of the cost function over FRC lung region is relatively easier and faster than optimization over TLC lung region.

However, in some cases we may need to know the motion on the coordinate of TLC, which provides more information. Registration from FRC to TLC is more difficult because the optimization complexity is increased. Using method described in Chapter 2 may result in inaccurate registration in some cases, as shown in Figure 4.1. In this example, boundaries and some features inside the region are misaligned. To solve this problem, we propose a new scheme to combine surface registration and volumetric registration together so as to provide better image matching results.

The framework of this new scheme is shown in Figure 4.2. It takes boundary correspondences from surface registration as input. Then interpolation is used to extend the boundary correspondences to the interior of ROI. Finally the interpolated displacement is served as the initial of volumetric registration, and intensity/feature-

(a)   (b)
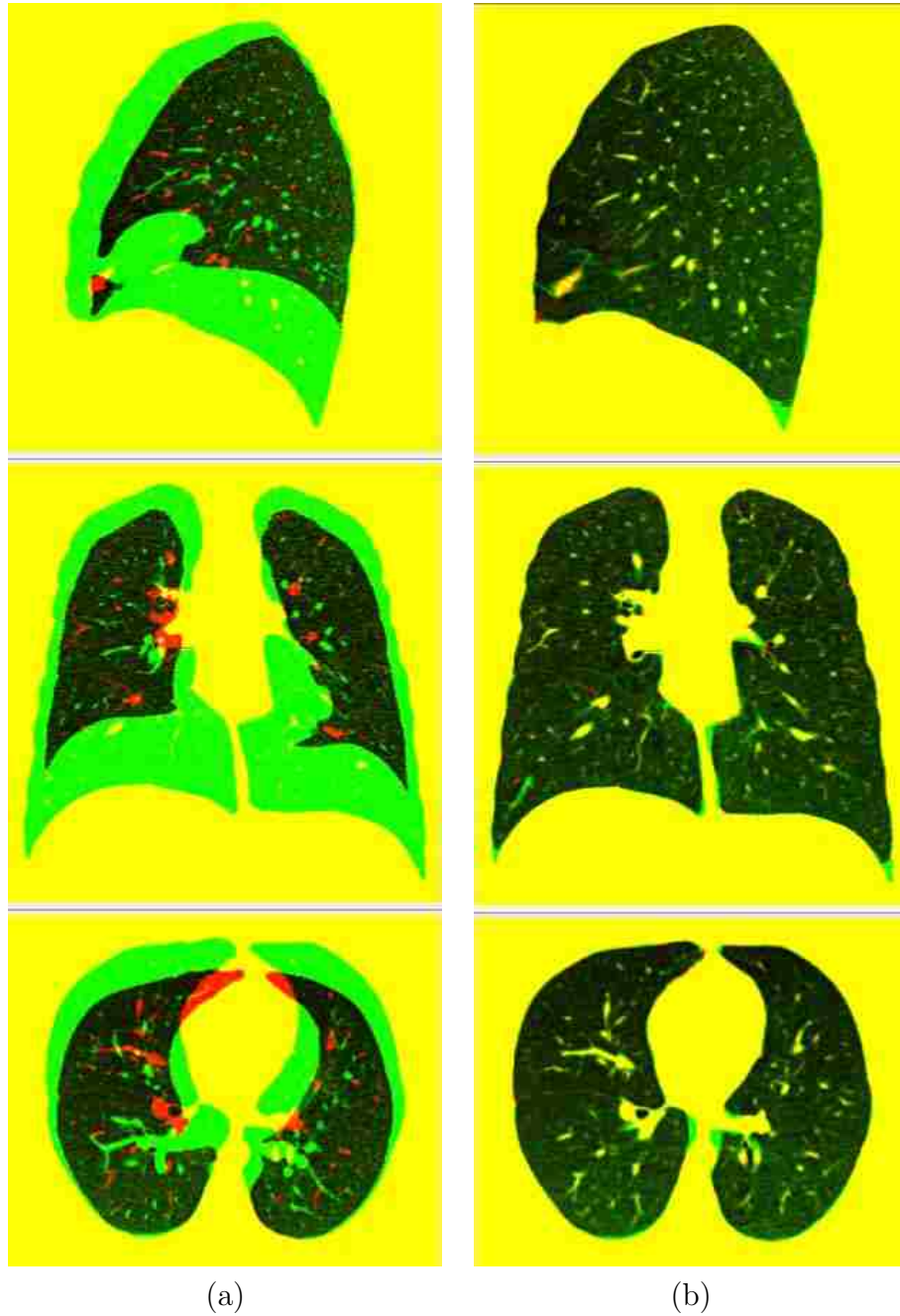
Figure 4.1: Mismatching problem using volumetric registration only. (a) shows the fused image of a pair of TLC data (colored red) and FRC data (colored green) before registration. (b) shows the fused images of the TLC data (colored red) and its corresponding deformed data from FRC (colored green) using registration methods described in Chapter 2.

based registration is used to fine tune the registration results.

4.2   Surface and Vessel Matching

Surfaces extracted from volumetric images play an important role in medical image analysis. Surface extraction usually utilizes the intensity contrast between the object and the background. For lung CT images, the parenchyma regions in the FRC and TLC data sets can be segmented using the method described in [66], followed by manual editing when necessary.

Since surfaces are relatively easy to define and provide rich source of shape information, their correspondences provide important boundary conditions for volumetric registration. There are many methods to solve surface registration problem, as discussed in [7]. An example is using transitive inverse consistent manifold registration (TICMR) method developed by Geng et al. [45]. TICMR uses a closest distance similarity measurement. It is regularized by a curvature based energy cost, and constrained by inverse-consistency and transitivity costs.

However, surface matching can only provide information along the lung boundaries. Adding feature correspondence inside the object may help generate more accurate initialization for the following steps. As we discussed in Section 2.5.2, vessel mask provides rich information of the major vessel locations. Those vessel locations in lung CT images are segmented using vessel segmentation algorithm [104]. The vessel matching can be solved using registration based on the centerlines of the vessel trees. The anatomical corresponding points on the centerlines can be determined using ICP
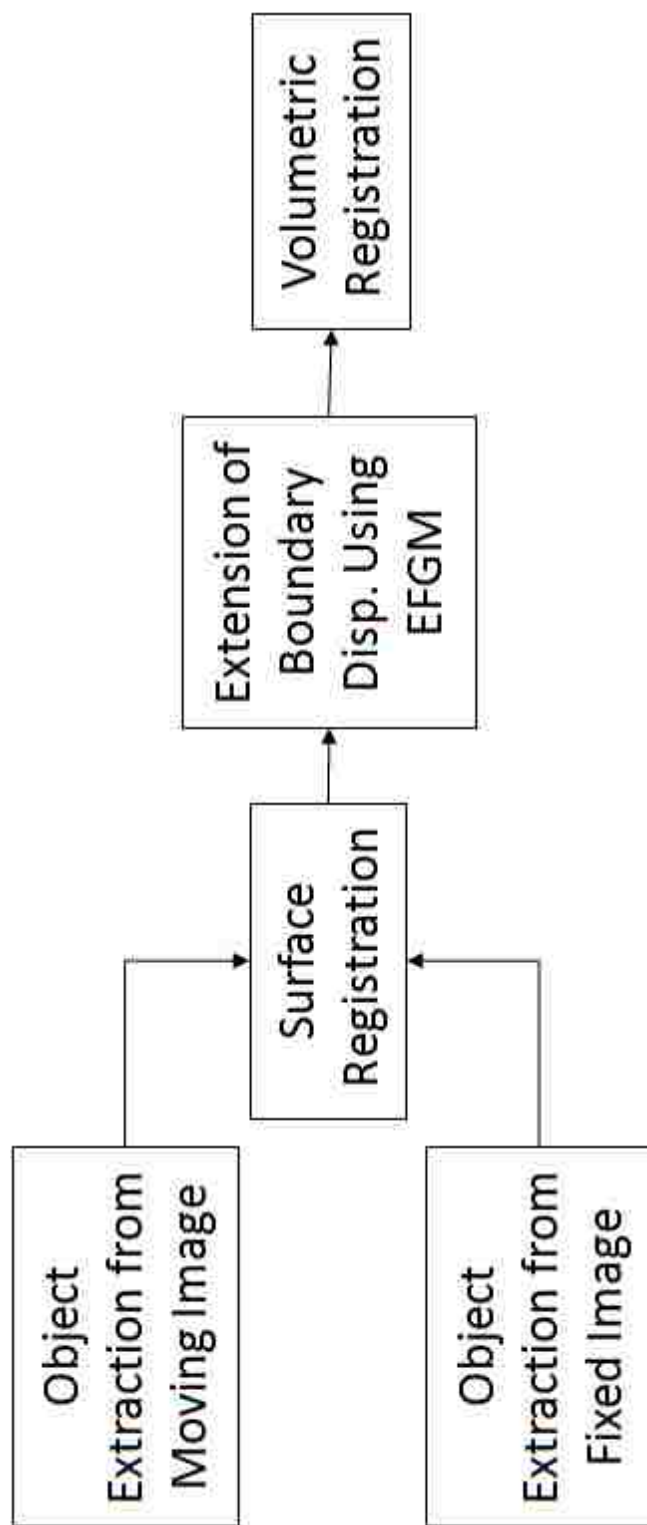
Figure 4.2: Flowchart illustrating steps of the new registration scheme. The boundaries of the objects are extracted and registered firstly to get the boundary correspondence. The element free Galerkin method is used to extend boundary conditions to the interior region. Volumetric registration is performed afterwards to further tuning the results.

(a)   (b)

Figure 4.3: Masks used to represent the object domain of lung CT images. The are generated by subtracting vessel masks from lung masks so as to enhance the vessel locations on (a) FRC data and (b) TLC data.

algorithm [9] or other methods measuring distances between contours [53].

In this work, surface and curve matching is not our focus. The object domain lies in the lung segmentation excluding the vessel masks. We simply registered the lung masks subtracted by the vessel masks, which provide strong intensity contrast across the lung surfaces and vessels, as shown in Figure 4.3. The registration method minimizing sum of squared intensity difference is used to solve this mask matching problem. Displacement on the lung surfaces and major vessel locations are extracted to serve as the boundary conditions for following steps.

4.3   Extension Using Element Free Galerkin Method

In order to extend the correspondence on the boundaries to the entire ROI, an interpolation step is needed. This step is a connection between surface registra-

tion and volumetric registration. It extends the boundary constraint generated in surface matching step to the interior of the object, which serves as initialization to the volumetric registration.

Traditional finite element method can be used to interpolate the boundary correspondence into the interior region. However, meshing of the object is needed for traditional finite element method, which is a computationally expensive process and is time consuming. Another solution is using element free Galerkin method (EFGM) [85]. EFGM does not require object meshing, but uses a uniform grid to solve the problem.

4.3.1 System Governing Equation

The problem of boundary matching between two objects can be represented by the boundary value problem as follows

$$\begin{cases} f(u(x)) = 0, \ x \in \Omega \\ u(x)|_{\partial\Omega} = u_\Delta(x), \ x \in \partial\Omega. \end{cases} \tag{4.1}$$

Here f is a differential operator representing energy constraints. Ω represent the region of interest to be registered, and $\partial\Omega$ represent the boundary of the object Ω. $u_\Delta(x)$ denotes the displacement fields in the entire region, and $u_\Delta(x), \ x \in \partial\Omega$ is the boundary displacements generated from previous step of surface registration. For 3D cases, $x = [x_1, x_2, x_3]$.

The boundary value problem can be described from two aspects: a differential equation governing the displacement fields over the object domain, and the boundary

conditions obtained from surface registration. The boundary value problem represented by Equation 4.1 is solved for displacement field $u(x)$, $x \in \Omega$ over the entire region of interest Ω, while the boundary correspondences is treated as the essential boundary conditions.

We consider the differential operator f as the Laplacian operator, i.e., $f = \nabla^2$ and $\nabla^2 = \nabla \cdot \nabla = \left[\frac{\partial^2}{\partial x_1^2} + \frac{\partial^2}{\partial x_2^2} + \frac{\partial^2}{\partial x_3^2} \right]$ for the 3-dimensional case. This leads to the following governing differential equation

$$\nabla^2 u(x) = \frac{\partial^2 u(x)}{\partial x_1^2} + \frac{\partial^2 u(x)}{\partial x_2^2} + \frac{\partial^2 u(x)}{\partial x_3} = 0 \tag{4.2}$$

Then the system equation becomes a Laplace's equation with boundary conditions

$$\begin{cases} \nabla^2 u(x) = 0, \ x \in \Omega \\ \\ u(x)|_{\partial\Omega} = u_\Delta(x), \ x \in \partial\Omega. \end{cases} \tag{4.3}$$

The system equation 4.3 has the following weak form for $\nabla^2 = \frac{\partial^2}{\partial x_1^2} + \frac{\partial^2}{\partial x_2^2} + \frac{\partial^2}{\partial x_3^2}$:

$$\int \int \int \phi(x) \left[\frac{\partial^2 u(x)}{\partial x_1^2} + \frac{\partial^2 u(x)}{\partial x_2^2} + \frac{\partial^2 u(x)}{\partial x_3^2} \right] dx_1 dx_2 dx_3 = 0. \tag{4.4}$$

Here $\phi(x)$ can be any smooth weighting function, which is non-zero inside the region of integration. In the Galerkin procedure, it is chosen to be the same as the shape function, i.e., basis function defined on the uniform grid. Selection of the basis function is discussed below.

4.3.2 Weighted Extended B-Splines

Splines are piecewise-polynomial functions used to represent smooth functions over a domain. In shape modeling and interpolating problems, B-Splines are popular

basis functions due to its advantages of good approximation, computational ease and localization for smooth functions. However, B-Spline basis can only represent functions in a rectangular domain, and can not represent arbitrarily shaped region.

Since the element free Galerkin method uses a regular grid instead of object mashing, the boundary conditions are enforced using a weighting function on the basis function. For example, B-Splines are not falling off to zero at the arbitrarily shaped object boundaries. This deficiency can be overcome by adding a weighting function on the basis function, which is called Weighted B-Splines. In addition, the B-Splines are defined over a regularly spaced grid. There may exist some B-Spline functions supporting only a very small portion of the object. Those B-splines with a small support of the ROI will cause the system equation to be unstable, and therefore cause inaccurate approximation.

Hollig et al. [63] have defined a new basis function called weighted extended B-Splines (WEB-Splines) to solve the finite element problem. In order to define WEB-Splines, we start by classifying cells or grids over image. Image cells can be partitioned into three categories:

1. *Interior cells*: These cells are contained entirely inside the object domains, and do not contain any point that lies on the boundary of the object or outside it.

2. *Boundary cells*: These cells contains at least one point from the boundary of the object.

3. *Exterior cells*: These cells do not contain any point that lies inside or on boundary of the object of interest.

Figure 4.4 shows the three different type of the cells for an object defined on a 2D domain using an equally spaced horizontal and vertical grid setting.
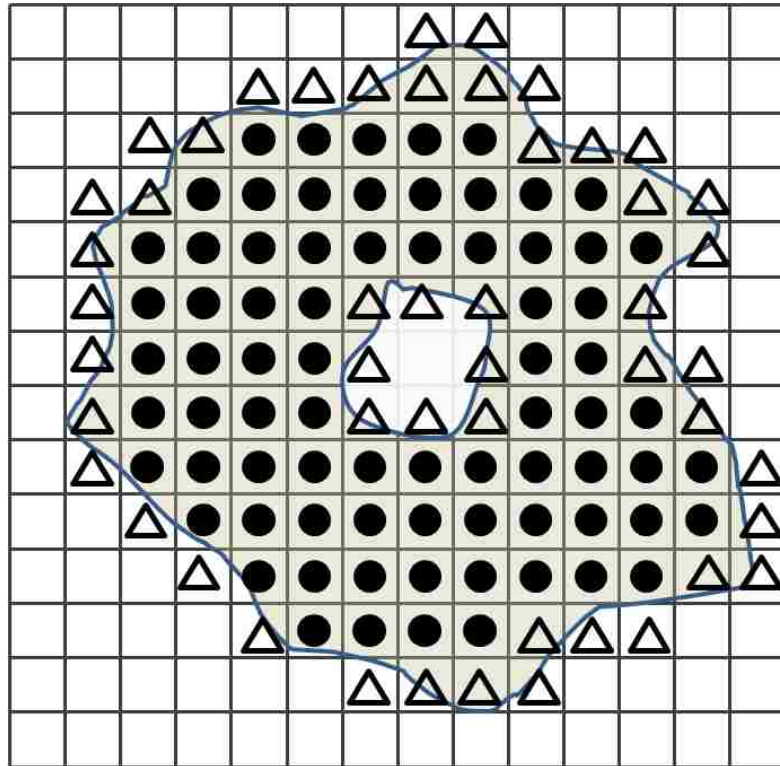
Figure 4.4: Illustration of cell types. The interior cells are marked with solid circle, and boundary cells are marked with triangle. All other cells are exterior cells.

Based on the cell definitions, the B-Splines are also partitioned into three categories:

1. *Inner splines*: These splines have support of at least one interior cell.

2. *Outer splines*: These splines have only boundary cells or exterior cells in their

support.

3. *Exterior splines*: These splines do not have any support over the object domain. Among the three kind of splines, outer splines do not contribute to represent the displacement in the object domain. In addition, directly updating the coefficients of outer splines may result in a highly sensitive response due to its limited support. In element free Galerkin method, this presents a problem since it causes Galerkin matrix to become ill-conditioned and unstable. Hollig et al. [63, 65, 64] overcome this problem by using weighted extended B-Splines (WEB-Splines). The WEB spline coefficients are evaluated only on the knot locations of the inner splines, and outer splines are taken into account using Marsden's identity [63].

Let $b(x) = \beta^{(3)}(x) = \beta^{(3)}(x_1)\beta^{(3)}(x_2)\beta^{(3)}(x_3)$ be the regular cubic B-Spline function in 3D case. $\beta(x)$ is defined in Equation 2.2. WEB-Splines $B(x)$ are defined based on B-Spline. It is computed using the inner and outer B-Splines over the object region.

Let the set of inner indices (indices of control point where inner splines start) be denoted by I and the set of outer indices be denoted by J, respectively. The WEB-Splines are constructed using Marsden identity for approximating polynomials with B-Splines. By construction, WEB-Splines combine the support of both inner splines and their associated outer splines, and they are defined only at the inner spline indices. This WEB-Splines are formulated as Equation 4.5.

$$B_i(x) = \frac{w(x)}{w(x_i)}[b_i(x) + \sum_{j \in J(i)} e_{i,j}b_j(x)], i \in I. \tag{4.5}$$

Here b_i and b_j's are the regular b-spline function. b_i is a inner spline index starts
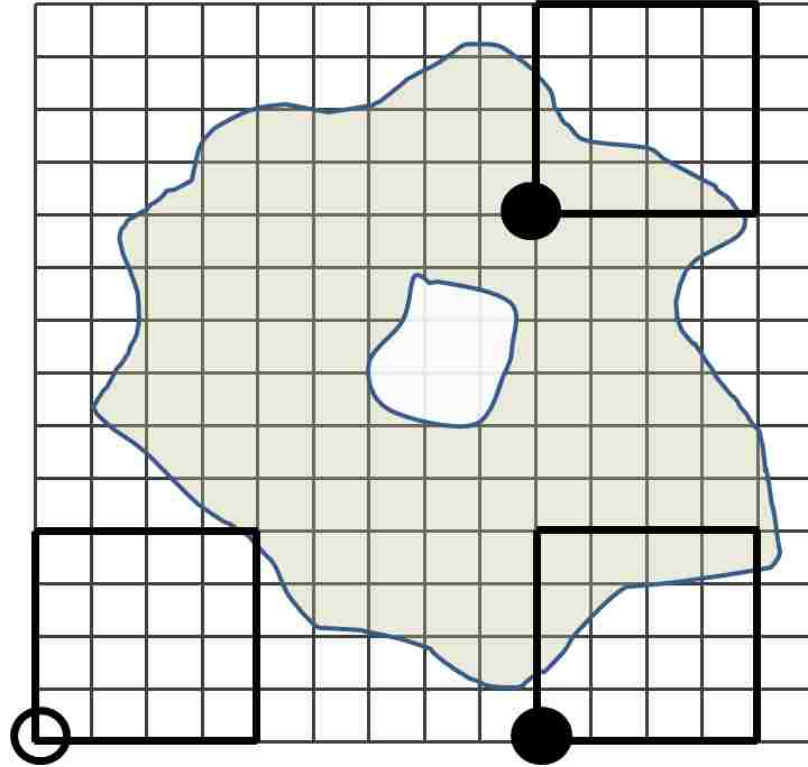
Figure 4.5: Illustration of spline types. We marked out two inner splines which start at the location marked with solid circle, and one outer spline which start at the location marked with hollow circle. The support is shown for splines of the order 3, i.e., for cubic splines. Therefore, the support is over $[0, 4]^2$ cells.

at index i, and b_j's are its associated outer spline start at indices j's. $w(x_i)$ is the value of weighting function at the center of interior cell in the support of inner spline starting at index i. The set $J(i)$ includes the set of outer spline indices, which are closest to inner index i using the following rule:

$$J(i) = \{j \in J | i \in I(j)\} \tag{4.6}$$

where $I(j)$ is the array of inner spline indices closest to the outer index j measured by Hausdorff distance. As long as the grid size is small enough, such an array always exists given by following equation:

$$I(j) = l + \{0, 1, \ldots, m\}^n \subset I. \tag{4.7}$$

The coefficients $e_{i,j}$ is solved by Hollig et al. using a closed form based on Marsden identity. The coefficients are calculated as

$$e_{i,j} = \prod_{\nu=1}^{n} \prod_{\mu=1, \mu \neq (i_\nu - l_\nu)}^{m} \frac{j_\nu - l_\nu - \mu}{i_\nu - l_\nu - \mu}. \tag{4.8}$$

$w(x)$ in Eq. 4.5 is a weighting function incorporated to satisfy essential homogenous boundary conditions. It is used to limit the support of WEB-Splines to the object domain. The weighting function $w(x)$ is defined as non-zero only over the region of interest and are zero at boundaries of the object and everywhere outside the object. It is a smooth function of distance from the object boundaries. The R-function method of Rvachev [99, 101, 100] provides an automatic mechanism for constructing the weighting functions. Following [63], we construct the weighting function based on the distance function. It is defined as follows

$$w(x) = 1 - max(0, 1 - dist(x, \partial\Omega)/\delta)^\gamma. \tag{4.9}$$

Here $dist(x, \partial\Omega)$ represents the distance function from a point x to the object boundary $\partial\Omega$. The parameter δ controls the width of the strip where the weighting function is between 0 and 1. γ controls the smoothness of the weighting function.

4.3.3 Displacement Parameterization

Now we solve the boundary value problem described in Equation 4.3 using WEB-Splines as basis functions. This system equation is solved for displacement field $u(x)$, $x \in \Omega$. The solution can be decomposed into two parts: $u^*(x)$ and $g_\partial(x)$. The component $u^*(x)$ is parameterized using WEB-Splines, which is constructed based on the shape of Ω. Due to the properties of WEB-Splines, $u^*(x)$ drops to zero at the boundary locations. On the other hand, $g_\partial(x)$ is a smooth function which approximates the boundary displacement resulted from surface registration, and gradually falls to zero at locations away from boundaries. The main purpose of using $g_\partial(x)$ function is to approximate the boundary conditions, and extend the boundary values to a region with non-zero measure. Then, the solution $u(x)$ can be represented as the sum of two functions $u^*(x)$ and $g_\partial(x)$:

$$u(x) = u^*(x) + g_\partial(x) \tag{4.10}$$

where

$$u^*(x) = \sum_i \mu_i B_i(x) \tag{4.11}$$

with B_i representing the WEB-Spline basis function.

The function $g_\partial(x)$ can be approximated using regular B-Splines with a least square fitting [78]:

$$g_\partial(x) = \sum_i c_i \beta_i(x) \tag{4.12}$$

where c_i is the B-Spline coefficient associated with its starting indices i. The Equation 4.12 approximate boundary displacement in a least-squared sense. $g_\partial(x)$ func-

tion can also generated by initialization from a delta function with $g_\partial(x) = u_\Delta(x)$ for $x \in \partial\Omega$ and $g_\partial(x) = 0$ for $x \notin \partial\Omega$, then simply apply a Laplacian convolution filteron the image for a number of iterations until a smooth function is achieved.

Please note that function $g_\partial(x)$ can be any smooth function that extends the boundary conditions to the object interiors. It does not need to explicitly follow any bending energy minimization. This is because only the function $u(x)$ combined from $u^*(x)$ and $g_\partial(x)$ need to satisfy the governing differential equation. Either $u^*(x)$ or $g_\partial(x)$ does not required to be minimized by the bending energy. The coefficients need to be estimated in Equation 4.3 correspond to u^*, while g_∂ function is fixed once computed.

4.3.4 Weak Form Formulation

In Equation 4.4, we show a weak form for the governing differential equation for $\nabla^2 = \frac{\partial^2}{\partial x_1^2} + \frac{\partial^2}{\partial x_2^2} + \frac{\partial^2}{\partial x_3^2}$. In the Galerkin procedure, the smooth weighting function $\phi(x)$ is chosen to be same as the shape function, which is WEB-Spline functions $B(x)$ in this case. Then we get the weak form

$$\int \int \int B(x) \left[\frac{\partial^2 u}{\partial x_1^2} + \frac{\partial^2 u}{\partial x_2^2} + \frac{\partial^2 u}{\partial x_3^2} \right] dx_1 dx_2 dx_3 = 0. \tag{4.13}$$

Substituting Equation 4.10 into Equation 4.13 and using the rule of integration by parts, we can rewrite the above weak form as

$$\begin{aligned} \int \int \int & \left(\frac{\partial B}{\partial x_1}, \frac{\partial B}{\partial x_2}, \frac{\partial B}{\partial x_3} \right) \left(\frac{\partial u}{\partial x_1}, \frac{\partial u}{\partial x_2}, \frac{\partial u}{\partial x_3} \right) dx_1 dx_2 dx_3 = \\ & - \int \int \int \left(\frac{\partial B}{\partial x_1}, \frac{\partial B}{\partial x_2}, \frac{\partial B}{\partial x_3} \right) \left(\frac{\partial g_\partial}{\partial x_1}, \frac{\partial g_\partial}{\partial x_2}, \frac{\partial g_\partial}{\partial x_3} \right) dx_1 dx_2 dx_3 \end{aligned} \tag{4.14}$$

For each element, the weak form in Equation 4.14 can be written as a matrix form:

$$A_e \ \mu_e = -B_e \tag{4.15}$$

Assembling matrices for all the grid points, we achieve a global matrix form of the equation:

$$A \ \mu = -B \tag{4.16}$$

A and B can be computed by evaluating the weak form integrals over each grid element, and using the pre-computed g function. Solving Equation 4.16 we will get WEB-Spline coefficients μ for the displacement inside the object domain. And therefore we extend the boundary matching results to the whole region of interest.

4.4 Volumetric Registration

The interpolated displacements over the object domain by extending boundary constraint using EFGM is now served as initialization of volumetric registration. The volumetric registration method introduced in Chapter 2 can be used to match lung CT images. The method utilizes the intensity and feature information at vessel locations. It is regularized by a linear elasticity constraint. The cost function for the volumetric registration is described in Section 2.5.

In the algorithm discussed in Chapter 2, regular cubic B-Spline is used to represent the displacement fields. In Section 4.3.2 we introduced the WEB-Spline functions, which is used to represent the displacement in the object domain during EFGM step. It can also be selected to parameterize the transformation in the

volumetric registration problem

$$h(x) = x + \sum_i \mu_i B_i(x), \ x \in \Omega \qquad (4.17)$$

WEB-Spline functions are non-zero inside the object, and zeros on the boundary and exterior region. Parameterization using WEB-Spline allows the boundary conditions to be fixed during the procedure of volumetric registration.

After using boundary conditions and EFGM interpolation, volumetric registration based on WEB-Splines and B-Splines are both evaluated in Section 4.5.

4.5   Results

4.5.1   Phantom Experiment

In order to illustrate how this registration scheme works, we create a pair of phantom images and show the intermediate results in each step in Figure 4.6. The first column show the moving and fixed images. Column 2 show the displacement and corresponding deformed moving image after using $g_\partial(x)$ function which extends the boundary values to a region with non-zero measure. Column 3 and 4 show the displacement and corresponding deformed moving image after EFGM interpolation and volumetric registration parameterized by WEB-Splines. It clearly show that the $g_\partial(x)$ function extends the boundary values to a region with non-zero measure (smooth along the boundary). The EFGM interpolation generates a gradually changing displacement fields in the entire region based on boundary values. The intensity information inside the object is blind to EFGM extension, and is used in the volumetric registration procedure to align the interior features.
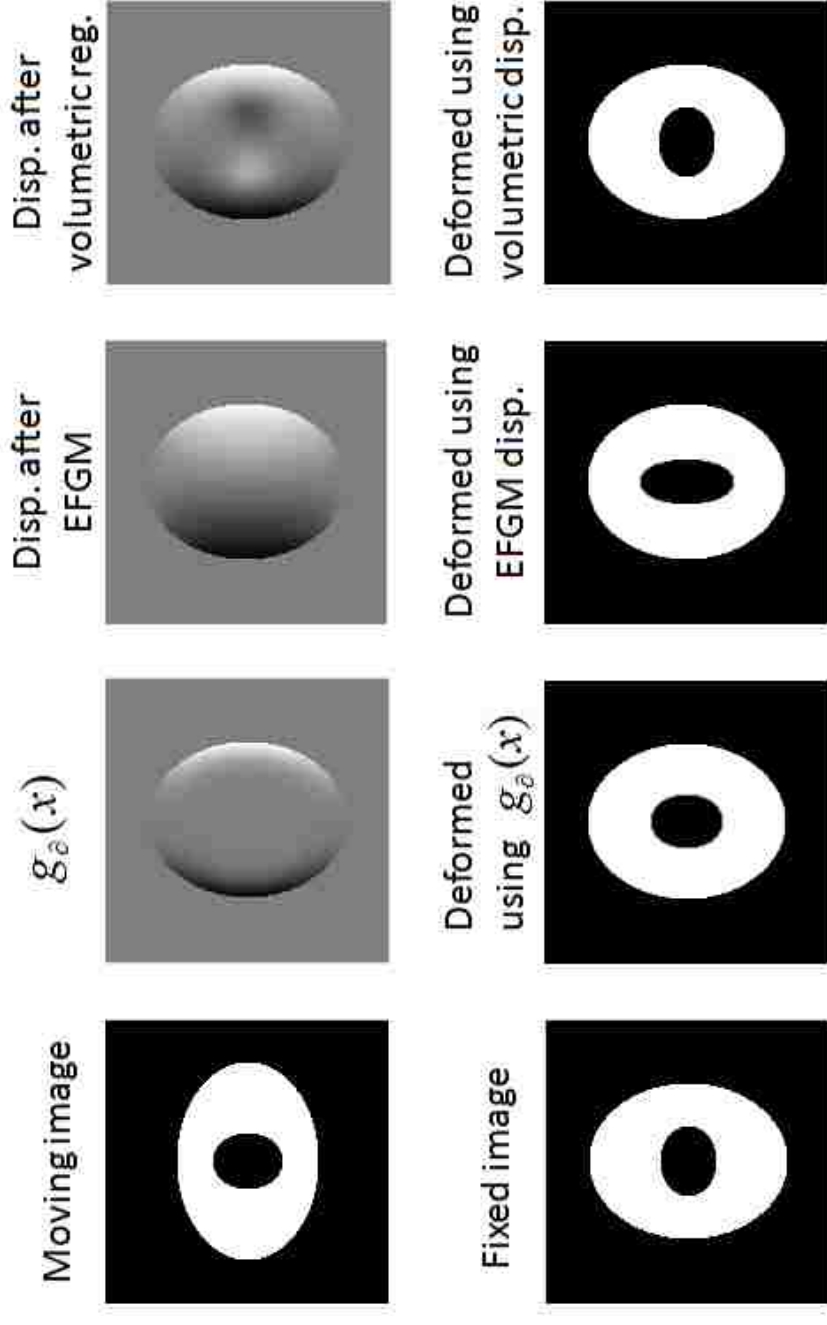
Figure 4.6: Illustration of the registration scheme working on phantom images. Column 2 to column 4 show the displacement and corresponding deformed moving image after using $g_\partial(x)$ function, EFGM interpolation and volumetric registration parameterized by WEB-Splines, respectively.

4.5.2   Visual Results of Registration Performance

The validation and evaluation experiments use data sets from six normal human subjects, which are described in Section 2.2. Contrary to the experiments in Chapter 2 (register TLC data to FRC data), registration experiments here are performed from FRC data to TLC data. In order to evaluate the performance of this boundary-conditioned registration scheme, three registrations are performed for each pair of data sets.

1. *B-Spline Reg. without EFGM*: Regular B-Spline based volumetric registration presented in Chapter 2.

2. *EFGM + WEB-Spline Reg.*: Extend boundary displacement generated from surface registration to the interior using EFGM. **WEB-Spline** based volumetric registration is performed afterwards.

3. *EFGM + B-Spline Reg.*: Extend boundary displacement generated from surface registration to the interior using EFGM. **B-Spline** based volumetric registration is performed afterwards.

Method 1 is purely volumetric registration, and method 2 and 3 are boundary conditioned registration using the new scheme.

The visual comparison of results from three different methods are illustrated in Figure 4.7 on a coronal slice. Figure 4.7 (a) shows the fused image of a TLC slice (colored red) and FRC slice (colored green) before registration; (b) - (d) show the fused images of the target TLC slice and its corresponding deformed slice from FRC using Method 1, 2, and 3, respectively. Using volumetric registration only, there

are mismatching along boundaries and at some vessel locations near the diaphragm region, as shown in Figure 4.7 (b).

Using methods which combines both surface and volumetric matching together, the boundaries and major vessels are firstly matched by surface registration. Then the displacement at boundaries are extended into the interior region using EFGM. Finally volumetric registration using information in the entire region are performed to achieve more accurate alignment. As shown in Figure 4.7 (c) and (d), those mismatching in (b) are corrected using the newly introduced registration scheme.

4.5.3 Lung Segmentation Overlap

The relative overlap (RO) between the segmentations of images is described in Section 3.6 and used to validate the global matching accuracy of different methods. The Relative Overlap (RO) statistic is used to measure how well corresponding regions of the parenchyma agreed with each other. Since the new scheme includes a surface matching in the first step, we expect them to achieve higher volume overlap than directly using volumetric registration. Table 4.1 lists the RO of parenchyma regions through six subjects after using volumetric registration only and registrations with boundary correspondences. It indicates that boundary-conditioned registration methods aligns global volumes better.

4.5.4 Landmark Error

For each scan pair of FRC and TLC data, the landmark selection is described in Section 3.3. The landmarks are selected at locations with good grayscale con-
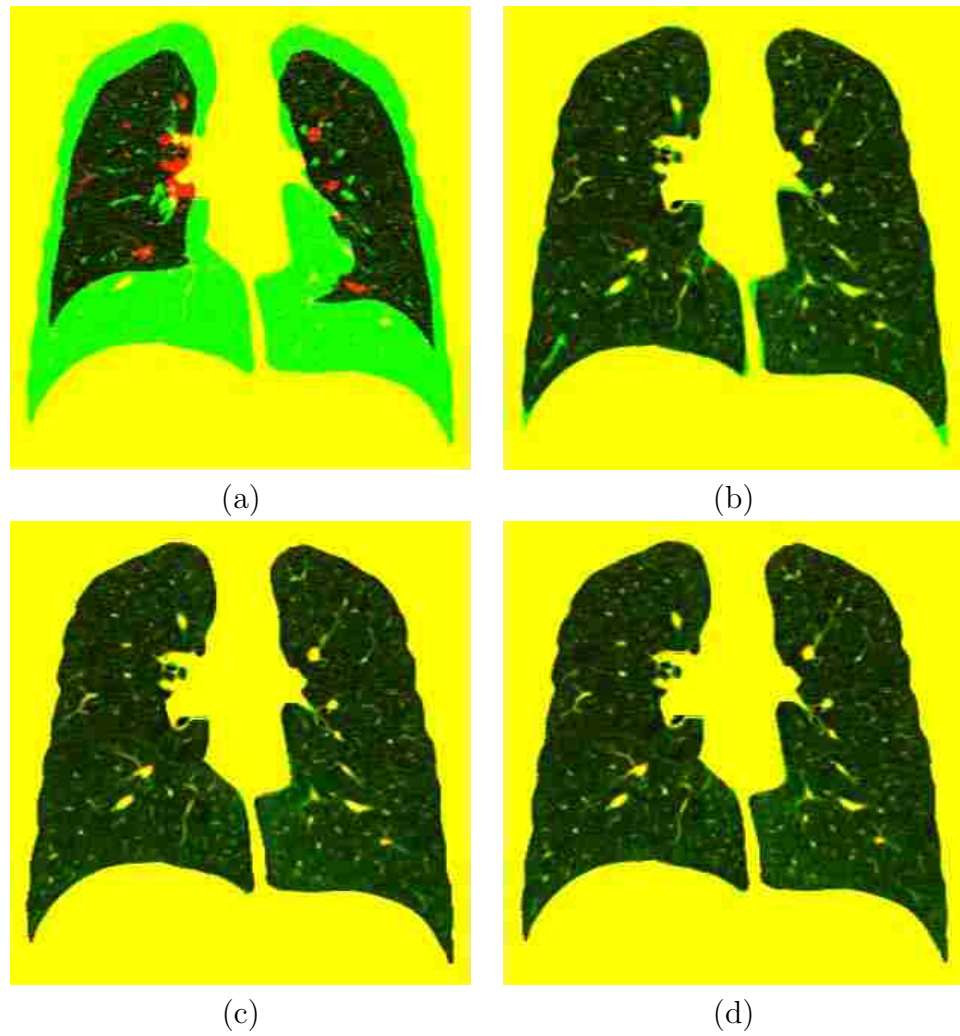
Figure 4.7: Visual comparison of results using volumetric registration only and registrations with boundary correspondences. (a) shows the fused image of a TLC slice (colored red) and FRC slice (colored green) before registration. (b) (d) show the fused images of the target TLC slice and its corresponding deformed slice from FRC using registration methods 1, 2, and 3, respectively.

trast, such as vessel-tree branches. Landmark distribution is illustrated in Figure 3.2. The distance between corresponding landmark pairs are estimated as landmark error. Table 4.2 lists the average and standard deviation of landmark errors through six subjects after using volumetric registration only and boundary-conditioned registrations. Although the average landmark errors from three methods are similar, the standard deviation using boundary conditions and volumetric registration is smaller than using volumetric registration only. This indicates that using volumetric registration only may result in a few dispersed landmark errors with large values. On the other hand, the landmark error resulted from the new scheme are tend to be closer to the mean when register images from FRC to TLC.

4.5.5   Vessel Matching Accuracy

The vessel matching accuracy is measured using the vessel positioning error (VPE) introduced in Section 3.4. Table 4.3 shows the vessel positioning errors (mm) through six subjects after using different registration methods. Since the vessels masks contain only major vessel locations, the mean and standard deviation of vessel matching errors are similar from three methods, with a slight drop when using the new boundary conditioned registrations.

4.5.6   Fissure Alignment Distance

The fissure alignment is measured by fissure positioning error (FPE) defined in Section 3.5. Table 4.4 shows the fissure positioning errors (mm) through six subjects after using volumetric registration only and registrations with boundary correspon-

Table 4.1: Relative overlap of parenchyma regions through six subjects.

Before Reg.	B-Spline Reg.	EFGM + WEB-Spline Reg.	EFGM + B-Spline Reg.
0.50	0.95	0.98	0.98

Table 4.2: Landmark errors (mm) through six subjects.

Before Reg.	B-Spline Reg.	EFGM + WEB-Spline Reg.	EFGM + B-Spline Reg.
27.40 ± 14.37	0.80 ± 1.37	0.78 ± 0.56	0.77 ± 0.56

Table 4.3: Vessel positioning errors (mm) through six subjects.

Before Reg.	B-Spline Reg.	EFGM + WEB-Spline Reg.	EFGM + B-Spline Reg.
12.65 ± 14.18	0.58 ± 0.50	0.57 ± 0.47	0.57 ± 0.46

Table 4.4: Fissure positioning errors (mm) through six subjects.

	Before Reg.	B-Spline Reg.	EFGM + WEB-Spline Reg.	EFGM + B-Spline Reg.
All fissures	**9.20 ± 7.94**	**1.15 ± 1.58**	**0.92 ± 0.79**	**0.90 ± 0.71**
Left oblique fissure	9.30 ± 8.49	1.04 ± 1.31	0.84 ± 0.70	0.86 ± 0.68
Right oblique fissure	7.86 ± 5.40	0.91 ± 0.71	0.95 ± 0.78	0.93 ± 0.74
Right horizontal fissure	10.71 ± 9.37	1.69 ± 2.47	0.99 ± 0.89	0.94 ± 0.73

dences. The first row lists the error statistics on all fissure locations, followed by errors on each fissure plane. It clearly shows the new scheme significantly improves matching accuracy on the left oblique fissure and right horizontal fissure by around 15% and 40%, respectively. This is because the left oblique fissure and right horizontal fissure extend to the base lung region, where large expansion happens and is usually difficult to register by directly using volumetric registration. The new scheme divides the problem into two parts, which matches boundaries and major vessels in the first place, then extend the boundary conditions to the interior region and adjust the displacement using volumetric information. The complexity for each single step is lower than the original task, and thus the matching problem is easier to solve and higher accuracy can be achieved.

4.6   Summary

In this chapter, we introduce a technique to register a pair of images with large distance utilizing both surface registration and volumetric registration. The novelty of this scheme is the idea of combining surface correspondence with volumetric intensity information using an efficient EFGM procedure. Boundary matching including surface and major vessel locations can be interpolated internally to the entire object domain using element free Galerkin method based on WEB-Splines.

Element free Galerkin method does not need object meshing, but uses a uniform grid to solve the interpolation problem. This method provide us an efficient approach to extend the boundary correspondence into the interior. In order to satisfy

the essential boundary conditions, a newly proposed WEB-Spline function is used as the basis to solve the system equation. The WEB-Spline function is nonzero inside the object domain, and vanishes at the boundaries. This property enable us to represent arbitrarily shaped region even with a uniform grid setting. In addition, outer splines which have very limited support in the image domain are removed in WEB-Spline setting, and their contributions are assigned on their closest inner splines. This property is important to ensure the system stability, and thus to achieve a more accurate approximation.

The volumetric registration can be parameterized by many basis functions, for instance, regular B-Splines and WEB-Splines in our method. The advantage of using WEB-Splines is that it enable us to keep the boundary correspondence unchanged, which is a good property when we have a satisfying surface matching results. On the other hand, this also implies the results will be impacted by the errors in the initial boundary correspondence. A poor initial boundary correspondence will remain unchanged since the basis function falls to zero at boundaries. Those error existing in surface matching step need to be corrected utilizing the intensity information of the entire image. Using regular B-Spline in the volumetric registration procedure allows boundary movement because it is nonzero valued on the boundaries. A better idea is using methods that allow the boundaries moving along the surface while minimizing the volumetric intensity based similarity cost, which is a future research direction.

The validation and evaluation results demonstrate that we are able to match the entire image volumes using the boundary correspondence as initialization. The

accuracy of global volume matching and alignment of regions around the base lung region are improved using both surface and volumetric registration. In conclusion, this new registration scheme provides a useful solution to solve complex registration problem in several procedures and achieves acceptable accuracy.

CHAPTER 5
ANALYZE MECHANICAL QUANTITIES BASED ON REGISTRATION DERIVED TRANSFORMATION

5.1   Introduction

CT imaging of the lungs provides a new opportunity for assessment of lung function through non-rigid image registration of a pair of scans at different inflation levels. After finding out the transforms and correspondence for each voxel between two images, we are ready for mechanical analyses on a regional level. Post-analyses of the registration resulting transformation reflect the mechanical quantities of local lung tissue.

From the image registration, we get the displacement fields which can be directly used to assess the magnitude and direction of local volume movement. Figure 5.1 shows a 3D displacement fields from FRC to TLC for one human subject. The vector fields give the direction of tissue motion, and the length of vectors reflects the motion magnitude. As observed, regions near diaphragm have larger tissue motions, and they are moving downwards.

Measurements resulted from the point-wise displacement fields reveal details of local tissue deformation pattern. Based on the dense displacement fields, some important mechanical quantities can be assessed by parameters and index maps from:

- Specific volume change analysis, quantifying specific volume through the nonlinear deformation;

- Strain analysis, quantifying the regional deformation magnitude and direction;
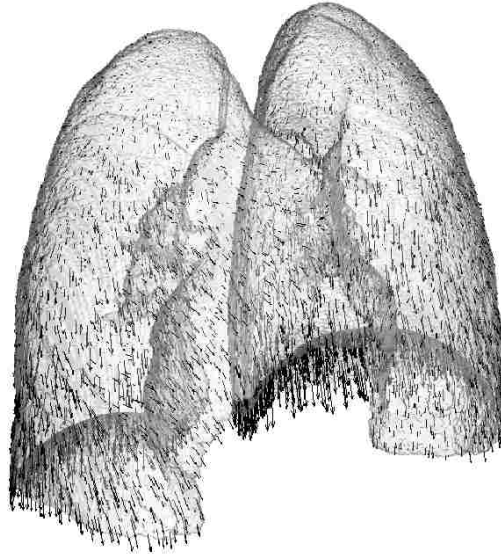
Figure 5.1: 3D displacements from FRC to TLC for one human subject.

- Anisotropic deformation analysis, quantifying the regional deformation pattern.

    Besides, assessment of the sensitivity of our technique for measuring regional lung mechanics to the registration error is also important for establishing the measurement confidence interval. The ability of measurements to detect features of different size is directly related to the node spacing of the transform parameterization. Understanding the sensitivity of measurement w.r.t. feature size using different B-Spline grid space is also of our interest.

    In this chapter, we will look into the mechanical quantity analyses and motion estimation of lung tissues. Also we will assess the measurement sensitivity related to the registration error and size of region of interest.

5.2   Data Sets

Mechanical analyses are performed on both human and sheep data. Human data acquisition is described in 2.2. For animal experiments, six adult sheep were used in this work. The image data were acquired using a Siemens Sensation 64 multi-detector CT scanner (MDCT) (Siemens Medical Solutions; Erlangen, Germany) with the sheep in supine position. The animals were anesthetized and mechanically ventilated during the experiments. Volumetric CT scans covering the thorax were acquired at 0, 5, 10, 15, 20, and 25 cm H_2O airway pressures (pitch 1, slice collimation 0.6 mm, rotation time 0.5 sec, slice thickness 0.75 mm, slice separation 0.5 mm, 120kVp, 100 mAs, Kernel B30f). They are denoted as the $P0$, $P5$, $P10$, $P15$, $P20$, and $P25$ images. The sheep data had voxel size of approximately $0.55 \times 0.55 \times 0.5$ mm^3. The image dimension of the transverse view is 512×512, and the z-dimension varies from 587 to 729.

5.3   Specific Volume Change

Specific volume change (SVC) measures the volume change of local structure under the deformation. The most intuitive way is calculating the Jacobian determinant as described in 3.7. The Jacobian of a transformation can be used to estimate the pointwise volume expansion and contraction of the transformation [92, 30].. Using a Lagrangian reference frame, local tissue expansion corresponds to a Jacobian greater than one and local tissue contraction corresponds to a Jacobian less than one.

For a region located at $\mathbf{x}$ defined in the target image I_2, transformation $\mathbf{h}(x)$

provide its corresponding position in the template image I_1 at $\mathbf{h}(\mathbf{x})$. Let $v_1(\mathbf{h}(\mathbf{x}))$ and $v_2(\mathbf{x})$ be the volumes of the same region in images I_1 and I_2, respectively. The Jacobian $J(\mathbf{h}(x))$ expresses the ratio between two volume states $v_1(\mathbf{h}(\mathbf{x}))$ and $v_2(\mathbf{x})$ for the volume element in I_1 and I_2

$$J(\mathbf{h}(x)) = \frac{v_1(\mathbf{h}(\mathbf{x}))}{v_2(\mathbf{x})} = \frac{v_2(\mathbf{x}) + \triangle v}{v_2(\mathbf{x})}, \tag{5.1}$$

where $\triangle v = v_1(\mathbf{h}(\mathbf{x})) - v_2(\mathbf{x})$ is the local volume change due to inspiration/expiration. Specific volume change is solved by rearranging Equation 5.1 [92]

$$sVC = \frac{\triangle v}{v_2(\mathbf{x})} = J(\mathbf{h}(x)) - 1. \tag{5.2}$$

Note that sVC is linearly related to the Jacobian, thus we can simply use the Jacobian measurement to observe the specific volume change.

In Figure 5.2, the specific volume change maps reflected by Jacobian show local volume expansion/contraction during inhalation/exhalation stages. Since the CT images were acquired with subjects in the supine orientation, an obvious dorsal to ventral gradient is noticed. This complies with the well known physiology that subjects positioned in the supine posture have more ventilation in the dorsal region. They also reflect the fact that vessels have little deformation during the respiratory cycle while lung tissues and airways expand/contract a lot.

For the sheep subjects, images at different inflation levels were acquired, noted as $P0$, $P5$, $P10$, $P15$, $P20$, and $P25$ images in an increasing pressure order. To track the deformation continuously, registration from $P0$ to $P5$, $P5$ to $P10$, $P10$ to $P15$, $P15$ to $P20$, and $P20$ to $P25$ are performed. From Jacobian maps of those
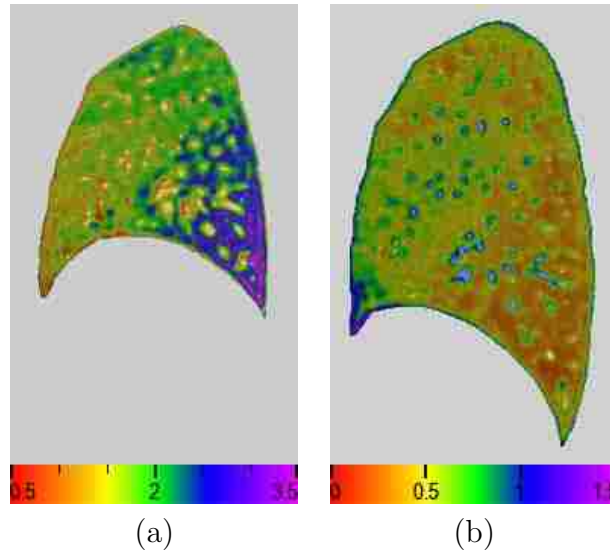
Figure 5.2: The Jacobian maps on a sagittal slice. (a) Jacobian on FRC image showing local volume deformation in inhalation stage; and (b) Jacobian on TLC image showing local volume deformation in exhalation stage.

transformations, we can estimate the local specific volume change for each pressure change pair during the inhalation process. Figure 5.3 (a)-(e) show the local lung tissue specific volume change of a transverse section from one sheep across all five pressure change pairs. The resulting volume change map has few negative values. Figure 5.3 (f) shows the pressure change pair for each voxel when it experienced the largest expansion during the inflation phase. It is noticed that lung tissue expands little from $P15$ to $P20$ and from $P20$ to $P25$. The first three pressure changes dominate the lung expansion. In addition, Figure 5.3 (f) shows that for this section, the superior half has most expansion from $P0$ to $P5$ while the inferior half has most expansion from $P10$ to $P15$.

Figure 5.3: Local lung tissue specific volume change of a transverse section during inflation. The inflation process of one sheep consists of (a) $P0$ to $P5$, (b) $P5$ to $P10$, (c) $P10$ to $P15$, (d) $P15$ to $P20$, and (e) $P20$ to $P25$ pressure change pairs. (f) shows the pressure change pair for each voxel when it experienced the largest expansion.
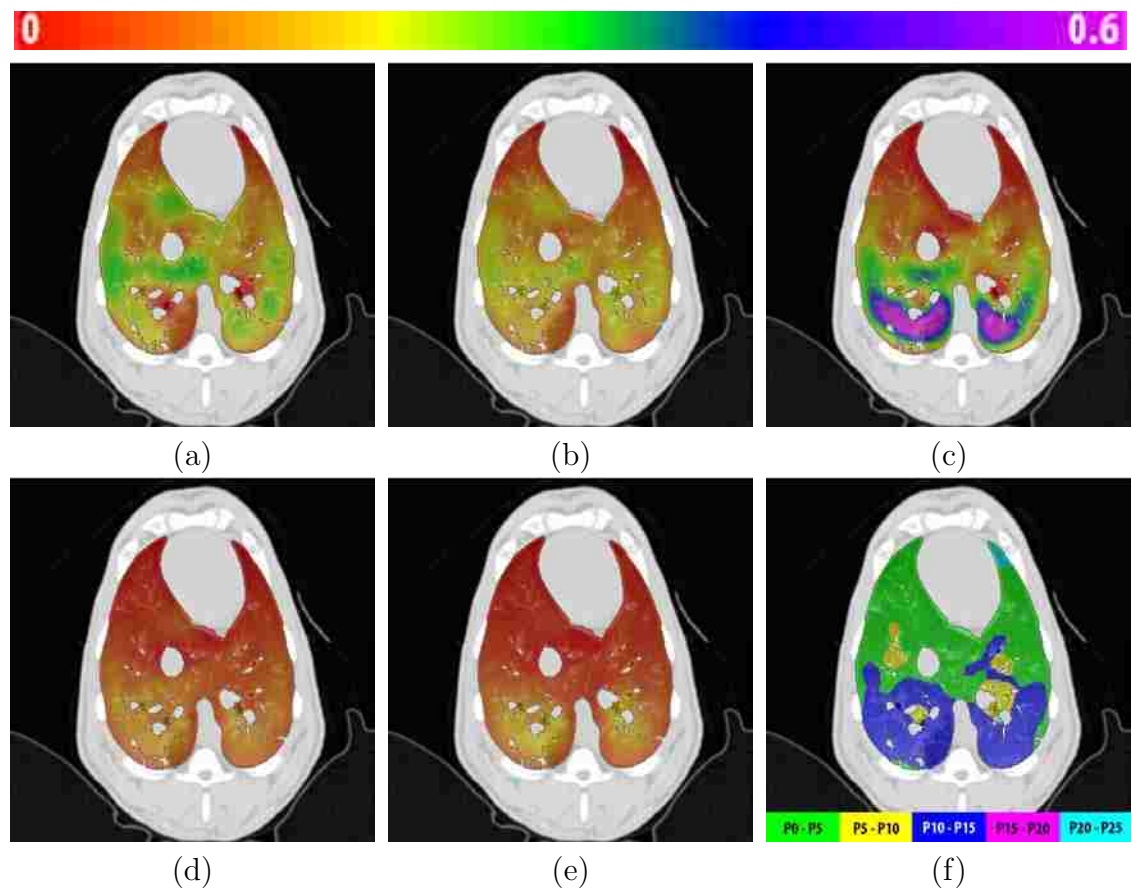
5.4   Strain Analysis

In classical mechanics, deformation of structures is characterized by the regional distribution of a strain or stretch tensor. From the displacement fields estimated in registration process, the displacement gradient tensor $\nabla \mathbf{u}$ can be calculated as the partial differentiation of the displacement vector with respect to the material coordinates

$$\nabla \mathbf{u} = \begin{bmatrix} \frac{\partial u_x}{\partial x} & \frac{\partial u_x}{\partial y} & \frac{\partial u_x}{\partial z} \\ \frac{\partial u_y}{\partial x} & \frac{\partial u_y}{\partial y} & \frac{\partial u_y}{\partial z} \\ \frac{\partial u_z}{\partial x} & \frac{\partial u_z}{\partial y} & \frac{\partial u_z}{\partial z} \end{bmatrix}. \tag{5.3}$$

Then we can apply strain tensor on the deformation gradient, and do analysis to express the geometrical deformation caused by the action of stress in the lung. In most general form, the strain is a symmetric tensor.

Linear Strain Tensor: The linear strain along x, y, and z axes are defined as

$$\epsilon_x = \frac{\partial u_x}{\partial x}, \quad \epsilon_y = \frac{\partial u_y}{\partial y}, \quad \epsilon_z = \frac{\partial u_z}{\partial z} \tag{5.4}$$

where $u = [u_x, u_y, u_z]^T$ is the 3D displacement field. Similarly the angular change at any point between two lines crossing this point before and after deformation can be measured as a shear strain. The shear strain are defined as

$$\begin{aligned} \gamma_{xy} &= \frac{\partial u_x}{\partial y} + \frac{\partial u_y}{\partial x} = \gamma_{yx}, \\ \gamma_{yz} &= \frac{\partial u_y}{\partial z} + \frac{\partial u_z}{\partial y} = \gamma_{zy}, \\ \gamma_{xz} &= \frac{\partial u_x}{\partial z} + \frac{\partial u_z}{\partial x} = \gamma_{zx}. \end{aligned} \tag{5.5}$$

Figure 5.4 gives an illustration of 1D linear strain and 2D sheer strain. Using the above notation for linear strain and sheer strain, it is possible to express strain as a

symmetric strain tensor

$$L = \begin{bmatrix} \epsilon_x & \frac{\gamma_{xy}}{2} & \frac{\gamma_{xz}}{2} \\ \frac{\gamma_{yx}}{2} & \epsilon_y & \frac{\gamma_{yz}}{2} \\ \frac{\gamma_{zx}}{2} & \frac{\gamma_{zy}}{2} & \epsilon_z \end{bmatrix} = \frac{1}{2}[\nabla\mathbf{u} + (\nabla\mathbf{u})^T] \tag{5.6}$$
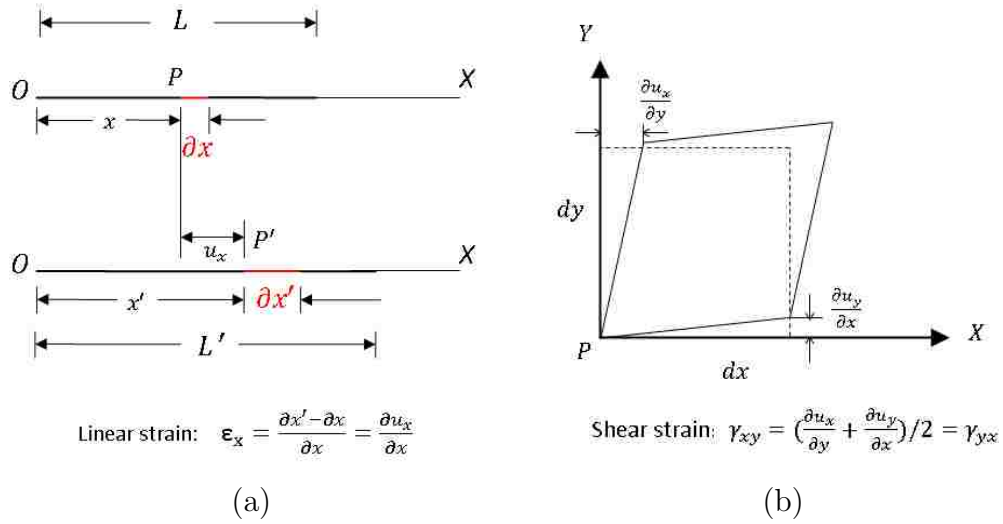
Figure 5.4: Illustration of (a) 1D linear strain and (b) 2D shear strain.

Green Strain Tensor: The concept of strain is used to evaluate how much a given displacement differs locally from a rigid body displacement. One of such strains for large deformations is the Lagrangian finite strain tensor, also called the Green-Lagrangian strain tensor or Green - St-Venant strain tensor, defined as

$$G = \frac{1}{2}[\nabla\mathbf{u} + (\nabla\mathbf{u})^T + (\nabla\mathbf{u})^T\nabla\mathbf{u}]. \tag{5.7}$$

Unlike Linear strain, Green strain considers the situation that rotation is a involved in the deformation.

Eulerian Strain Tensor: The Eulerian-Almansi finite strain tensor, referenced to the deformed configuration, i.e. Eulerian description, is defined as

$$G = \frac{1}{2}[\nabla\tilde{\mathbf{u}} + (\nabla\tilde{\mathbf{u}})^T - (\nabla\tilde{\mathbf{u}})^T\nabla\tilde{\mathbf{u}}], \tag{5.8}$$

where $\tilde{\mathbf{u}}$ can be considered as $\mathbf{u}^{-1}$.

The strain tensors are real symmetric matrices. Through singular value decomposition (SVD), they can be represented as a set of orthogonal eigenvectors, along which there is no shear, but only expansion or compression. These eigenvalues and eigenvectors are denoted as principal strains and principal directions. The maximal eigenvalue for each tensor is defined as maximal principal strain, and its corresponding eigenvector is called maximal principal direction. The principal strains and directions provide valuable information on preferential directionalities in deformation.

After applying strain tensor on the displacement fields, the directions along which there is only linear strain (stretch or compression) for local lung tissue were also estimated using SVD analysis. Figure 5.5 illustrates the maximal principal direction, maximal principal strain, and Jacobian together on a transverse slice and a coronal slice. It enable us to get more details of the lung tissue expansion instead of just knowing the expansion ratio from Jacobian.

Figure 5.6 shows maps of the maximal principal strain from linear strain, Green strain, and Eulerian strain tensors. Although they are of different ranges, regional patterns are similar among all three strain measures. Within the six sheep subjects, the maximal principal strain (linear) varied regionally from 0% at some sites to 116% at others (5th to 95th percentiles: 8 to 72%).

(a) (b)
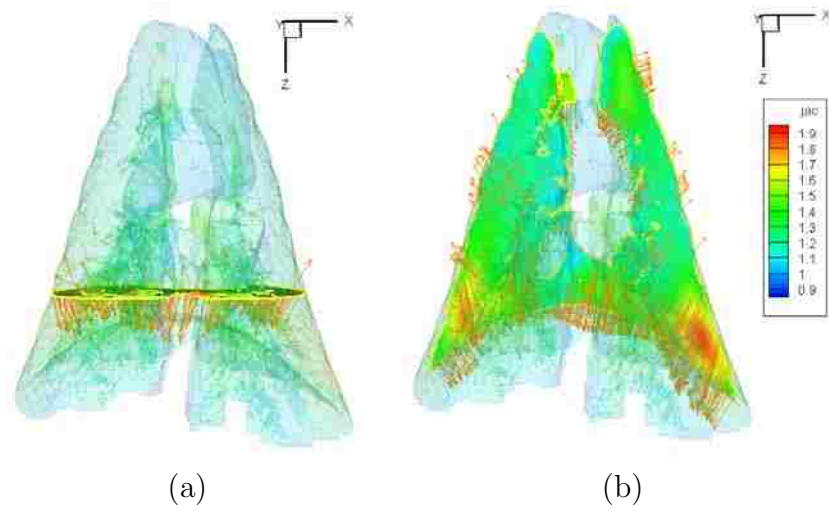
Figure 5.5: Maximal principal directions of $P0$ to $P10$ transformation are shown on (a) a transverse slice and (b) a coronal slice for one sheep. Vector magnitudes represent maximal principal strains, and colored contours express the Jacobian.
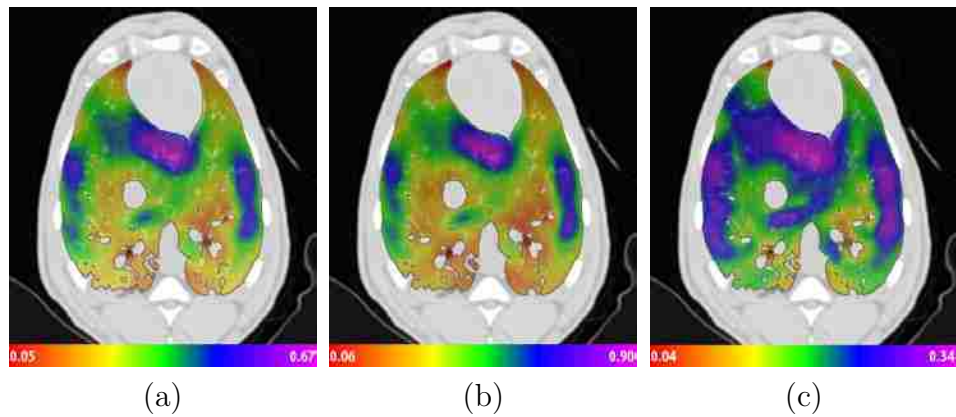

(a) (b) (c)

Figure 5.6: Maximal principal strains from (a) linear strain, (b) Green strain, and (c) Eulerian strain tensors shown on a transverse slice from $P0$ to $P10$ for one sheep.

5.5   Anisotropy Analysis

Regional deformation of the lung during inspiration and expiration is more than just volume change. Volume change may also have orientational preference anisotropy of deformation [119, 97]. For instance, regions closest to the diaphragm are likely to experience more volume change in the vertical orientation. And regions closest to the heart may be more constrained from expanding normal to the heart. Volume change and deformation anisotropy are independent quantities as a region may undergo no volume change but still have deformed significantly, such as the case that the lengthening in one orientation is compensated by contraction along another orientation. Therefore, without orientational preference, regional volume change alone is not enough to justice the characterization of lung deformation.

Regional Stretch: In continuum mechanics, the deformation gradient tensor $\mathbf{F}$ is the same as the Jacobian matrix $\mathbf{J}$ of the transformation. It describes the continuum deformation from point-wise displacements, and can be decomposed into stretch and rotation components:

$$\mathbf{F} = \begin{bmatrix} 1 + \frac{\partial u_x}{\partial x} & \frac{\partial u_x}{\partial y} & \frac{\partial u_x}{\partial z} \\ \frac{\partial u_y}{\partial x} & 1 + \frac{\partial u_y}{\partial y} & \frac{\partial u_y}{\partial z} \\ \frac{\partial u_z}{\partial x} & \frac{\partial u_z}{\partial y} & 1 + \frac{\partial u_z}{\partial z} \end{bmatrix} = \mathbf{R}\mathbf{U}. \tag{5.9}$$

Here $\mathbf{U}$ is the right stretch tensor and $\mathbf{R}$ is an orthogonal rotation tensor.

The Cauchy-Green deformation tensor is defined as follows

$$\mathbf{C} = \mathbf{F}^T\mathbf{F} = \mathbf{U}^T\mathbf{R}^T\mathbf{R}\mathbf{U} = \mathbf{U}^T\mathbf{U}. \tag{5.10}$$

In order to obtain stretch information from $\mathbf{U}$, we firstly evaluate the deformation tensor $\mathbf{C}$. The eigensystem of $\mathbf{C}$ can be represented by the eigenvector N_1, N_2 and

N_3 and their corresponding eigenvalues λ_1^2, λ_2^2 and λ_3^2. Therefore, after eigendecomposition of $\mathbf{C}$ and taking the square root of the three eigenvalues, we can get the eigenvalues of $\mathbf{U}$ λ_1, λ_2 and λ_3 (ordered as $\lambda_1 > \lambda_2 > \lambda_3$). The eigenvalues of $\mathbf{U}$ are defined as principal stretches and calculated as

$$\lambda_i = \sqrt{eigenvalues \ of \ \mathbf{C}}. \tag{5.11}$$

Distortion Index (DI): The ratio of the length in the direction of maximal stretch over the length in the direction of minimal stretch is defined as distortion index (DI)

$$DI = \frac{\lambda_1}{\lambda_3}. \tag{5.12}$$

The DI value is always larger or equal to 1. A big DI value indicates an anisotropic expansion, while a DI values approximately 1 represents an isotropic expansion.

Figure 5.7 shows the maps of Jacobian, principal linear strain and distortion index (DI) on one transverse slice. Comparison between Jacobian and principal strain together with the distortion index map can reflect more lung tissue deformation information. For the region near the aorta in the left lung (black rectangular region), the Jacobian is big where the principal strain is relatively small. This illustrates that this region experienced an isotropic expansion, shown as red in the DI map (small DI value approximately 1) . For the region near heart (red rectangular region), the Jacobian is relatively small while its principal strain is large. This illustrates that region experienced an anisotropic expansion, shown as purple in the DI map (larger DI value approximately 2). This anisotropic expansion may be caused by the blocking of heart. Within the six sheep subjects, DI varied from 1 (isotropic deformation) to

3.71 (anisotropic deformation). Regional deformation is significantly anisotropic at the posterior end of lungs, but more isotropic at the anterior end.
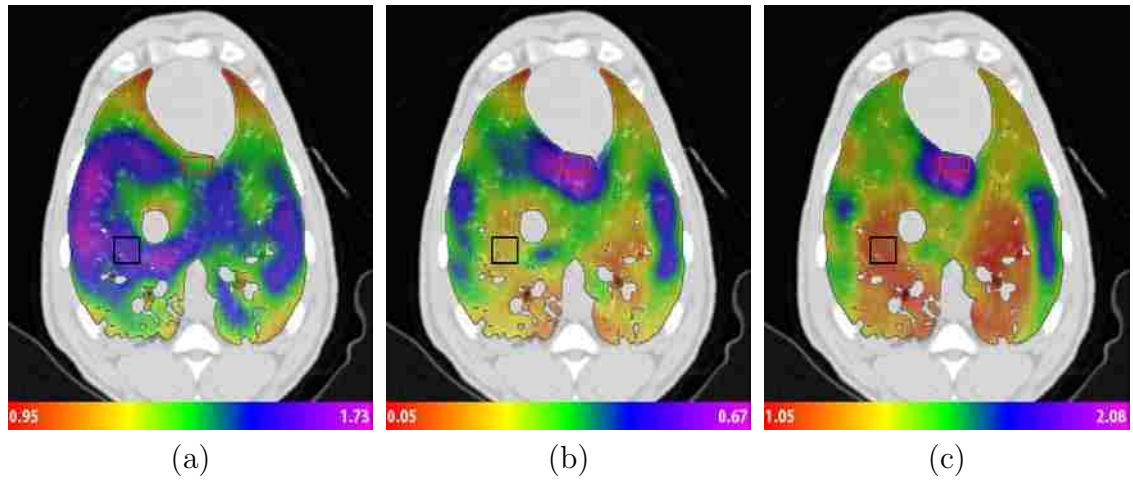
Figure 5.7: Lung expansion measures resulted from registration. (a) Jacobian, (b) principal linear strain, and (c) distortion index are shown on a transverse slice of deformed image from $P0$ to $P10$ for one sheep.

Amelon et al. [4] has proposed another method to quantify the magnitude of anisotropy by defining the anisotropy deformation index (ADI)

$$ADI = \sqrt{(\frac{\lambda_1 - \lambda_2}{\lambda_2})^2 + (\frac{\lambda_2 - \lambda_3}{\lambda_3})^2}. \tag{5.13}$$

It takes the three stretch factors into consideration, and thus has better discriminability among different anisotropy deformation patterns. This ADI calculation ranges from 0 to ∞ where 0 indicates perfectly isotropic deformation.

The average volume change ratio from FRC to TLC through six human sub-

jects is 1.93. Table 5.1 lists the 5th to 95th percentiles of Jacobian, principal strain, and distortion index calculated from the six subjects. It gives approximate ranges of different mechanical parameters quantifying tissue expansion from FRC to TLC. The mean and standard deviation of the three parameters on parenchymal tissues, vessels and fissures are listed in table 5.2. We can observe that tissues have more expansion than vessels, and fissures are deforming more anisotropically than other regions.

Table 5.1: 5th to 95th percentiles of lung mechanical quantities.

	5%	95%
Jacobian	1.17	3.03
Principal Strain	0.23	1.08
Distortion Index	1.17	3.32

Table 5.2: Statistics of lung mechanical quantities on different structures.

	Parenchyma	Vessel	Fissure
Jacobian	1.91 ± 0.55	1.28 ± 0.27	1.81 ± 0.41
Principal Strain	0.52 ± 0.25	0.35 ± 0.20	0.68 ± 0.34
Distortion Index	1.66 ± 0.67	1.56 ± 0.43	2.34 ± 1.34

5.6   Sensitivity to Noise on Displacement Field

Since the lung function quantities are derived from the displacement fields, the lung registration results need to be correct and physiologically meaningful, in addition to be spatially accurate. Kabus et al. [69] have recently shown that methods with roughly the same mean landmark error may produce very different Jacobian patterns. Therefore, we are interested in assessing the sensitivity of our registration method for measuring regional lung mechanical quantity w.r.t. the registration error, and then establish measurement confidence interval.

We introduce the perturbation to the coefficients of displacement field with random noise. The noise is zero mean additive Gaussian noise with a standard deviation σ. The standard deviation σ is proportional to the coefficients magnitude, which means coefficients with larger magnitude is prone to get larger deviations. This design is based on the observation that registration usually has larger errors in the region with larger deformation. Introducing noise in displacement will result in changing biomechanical measurement. We perform statistical analysis on the ratio between original Jacobian measurement and deviated Jacobian measurement. Note that at each location, the ratio is calculated as larger value divided by smaller value. Then the geometric mean of the Jacobian ratio is calculated w.r.t. the mean of displacement noise. This may imply the robustness and the detectable resolution of a intrinsic lung tissue function change from our technique. The experiments are performed on B-Spline coefficients with varying grid spaces. Synthesized statistics using results form six different subjects are shown in Figure 5.8.
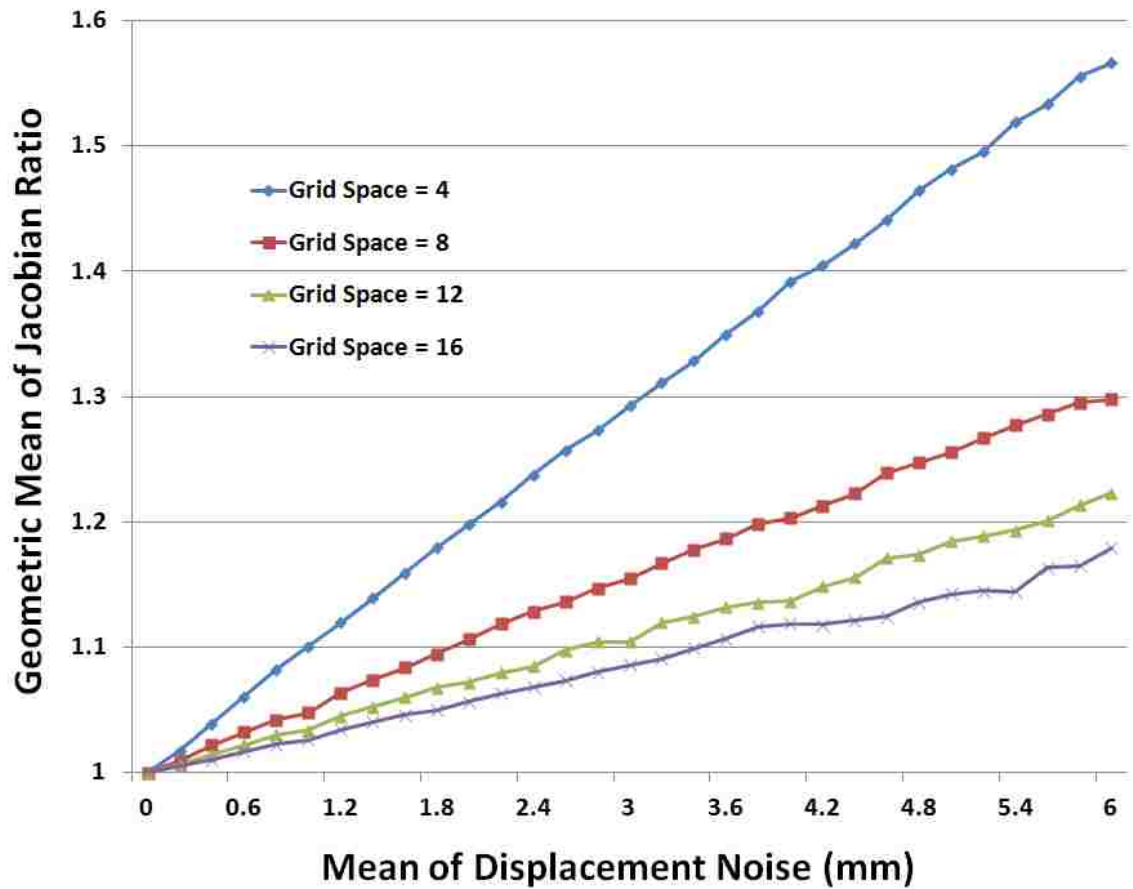
Figure 5.8: Geometric mean of ratio between Jacobian measurements from original displacements and from displacements with noise. The range of noise is reflected by the mean of displacement noise on horizontal axis.

Figure 5.8 reflects the fact that larger grid space is less sensitive to the displacement noise. Our registration estimates the lung motion with average error within 1 mm on landmarks, vessels and fissure planes. According to Figure 5.8, 1 mm average error on displacement may result in at most 10% measurement change for B-Splines with grid space 4 mm. As the grid space increase to 8 mm, 12 mm, and 16 mm, the measurement changes decrease to around 5%, 3% and 2%, respectively.

5.7   Sensitivity to Feature Size

The grid size of the B-Spline lattice decides the number of parameters estimated in the registration process. Smaller B-Spline grid spacing setting models the transformation with more local details [13]. However, a smaller B-Spline grid spacing setting leads to a larger parameter sets to optimize in the registration process, which may cause longer running time. For a fixed region, it is interest to study how small the grid spacing need to be in order to detect its mechanical quantity change. Utilizing the difference of deformation pattern between vessel and parenchymal tissue structures, we can use derived Jacobian maps to reveal how fine the grid spacing need to be in order to detect a given size structure.

Figure 3.8 reflects the fact that vessels have little deformation during the respiratory cycle while lung tissues and airways expand/contract a lot. The Jacobian difference between vessels and other lung regions can be utilized to reveal how small a structure can be detected as the grid size of the B-Spline lattice is changed. Using different lattice grid size settings, the Jacobian maps on the same sagittal slice of a

FRC data are compared in Figure 5.9. For comparison, Small Deformation Inverse Consistent Linear Elastic [22] (SICLE) registration, which uses the sum of squared difference as similarity cost and its transformation represented by Fourier coefficients, is also used to register the same data and produce Jacobian map. SICLE uses approximately the same number of basis parameters compared to our B-Spline based registration with grid size of 16 mm.

SICLE uses the low order Fourier coefficients in each direction to represent the transformation, only global information are preserved. Thus its resulted Jacobian map Fig. 5.9 (d) is much smoother than that from B-Spline based registration, which loses the ability to model deformation locally. This observation reveals the advantage of using B-Splines as basis function to represent transformation. For B-Spline based registration, finer grid setting can give a more detailed deformation map, as noticed in Fig. 5.9 (a)-(c).

Figure 5.10 shows the effect of changing grid size to detect vessels of different sizes and to detect two vessels in real images based on Jacobians (FRC to TLC). The Jacobian of the transformation produced using SICLE is also plotted for comparison. Each picture in Figure 5.10 plots the 1/Jacobian (left vertical axis) and HU value (right vertical axis) changes along a line profile. The horizontal axis lists the point numbers on the line profile.

As the vessel size goes smaller, their deformation can be detected from registration using smaller grid size setting, while registration using larger grid size setting loses track of small vessels and nearby vessels. This can help us make choice of our
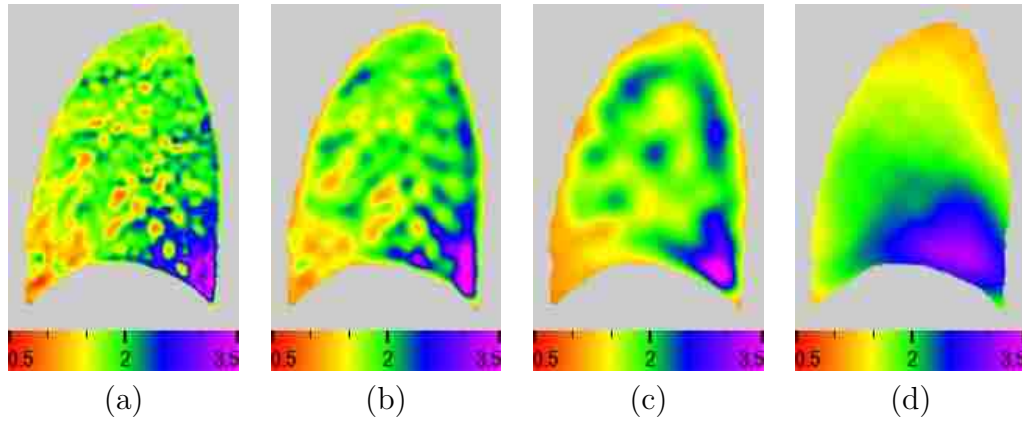
Figure 5.9: Jacobian maps from transformations using B-Splines with different grid space and from SICLE. The maps are shown on the same sagittal slice of a FRC data resulting from registration with the B-Spline lattice grid size of (a) 4 mm, (b) 8 mm, and (c) 16 mm. (d) shows the Jacobian map resulted from SICLE.

B-Spline lattice setting in order to detect the deformation of features with acceptable accuracy and time cost.

From Figure 5.10, we notice that the Jacobian values change quickly around the vessel/tissue boundary. For quantified analyzing purpose, we can use full width at half maximum (FWHM) as a parameter to describe the ability of feature detection. The definition of FWHM is illustrated in Figure 5.11. Given the difference between two extreme values of a variable, FWHM express the distance of two points at which the variable drops to half from its maximum value. For our cases, the FWHM of Jacobian close to vessel size implies a good feature detection. Please note that since Jacobian is not a linear parameter, we perform a logarithm operation on the Jacobian variable to bring it to a linear space. FWHM is calculated based on the logarithmic
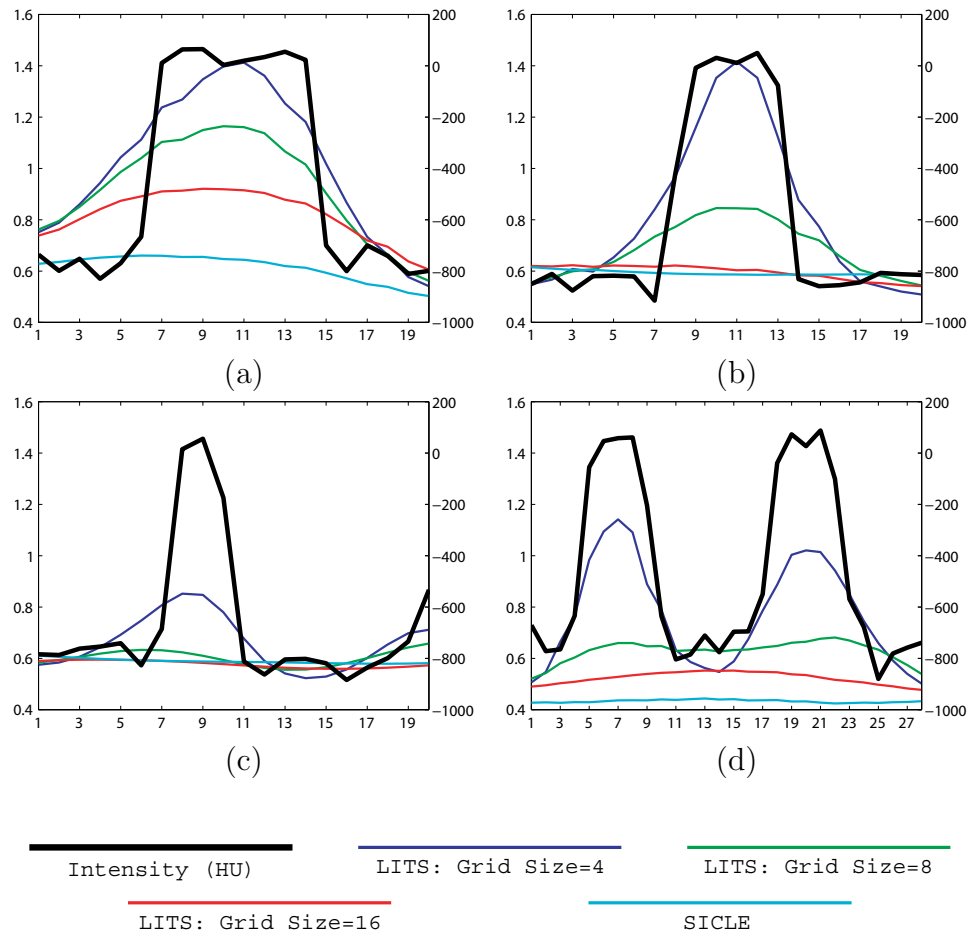
Figure 5.10: Jacobian changes along profile lines. The changes of 1/Jacobian (left vertical axis) and HU value (right vertical axis) on line profiles (a)-(c) across vessels of different sizes, and (d) across two nearby vessels. The horizontal axis lists the point numbers on the line profiles. Jacobian values are estimated from SICLE resulting transformation, and from transformations using the B-Spline lattice grid size of 4 mm, 8 mm and 16 mm.

Jacobian.
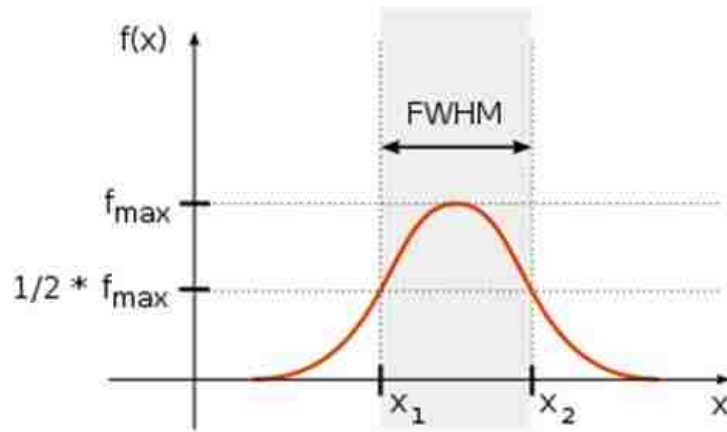
Figure 5.11: The illustration of full width at half maximum (FWHM) [3].

To find the detectable feature size range for a grid spacing setting, we conduct two sets of experiments. The first one is analysis using phantom data. We create a serious of hollow cylinders with varying diameters of the hollow region. For each fixed hollow diameter, we have a pair of images with deformation in the solid cylinder region. Figure 5.12 (a) and (b) shows an example of hollow cylinders with the same hollow region size.

Registrations are performed between each pair of images with the same hollow region size. Since the hollow region is fixed, the Jacobian values inside should be around 1. And outside solid region should have uniform Jacobian values which reflect the expansion, as shown in Figure 5.12 (c). This phantom experiment design resem-
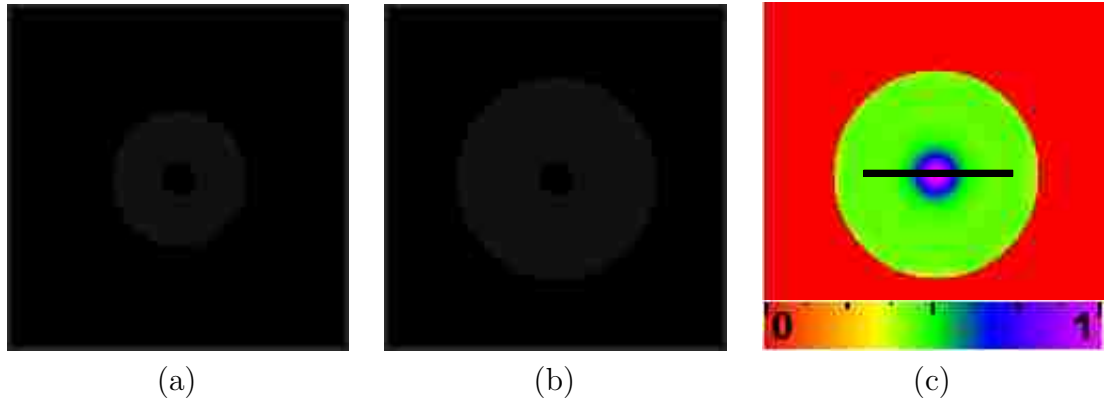
Figure 5.12: The phantom images of hollow cylinders. (a) and (b) show a pair of hollow cylinders with the same inner radius but different outer radius. The Jacobian of transformation from (a) to (b) is shown in (c). Jacobian values along the black profile line are used to find the FWHM.

bles deformation between tissue and vessel. Therefore, along the profile line which go across the image center, we are able to find the FWHM of the Jacobian variable.

The calculation of FWHM under two situations are considered to be invalid. The first case is that the difference between the maximum and minimum Jacobian values is too small. Under this situation, the change of Jacobian is nominal and can not reflect the feature property. The second case is that the FWHM is larger than twice of the diameter of hollow region. Those FWHM values are considered as meaningless for feature detection and will be throw away.

Figure 5.13 shows the FWHM of Jacobian with varying hollow region size and different grid sizes. B-Spline grid sizes are changing from 2 mm to 10 mm, and the diameters of hollow region are increasing from 2 mm to 10 mm. It is obvious that

for a fixed hollow region size, B-Spline with smaller grid size can detect them with higher accuracy. And for smaller hollow region, only B-Splines with finer grid setting can keep track of the feature.
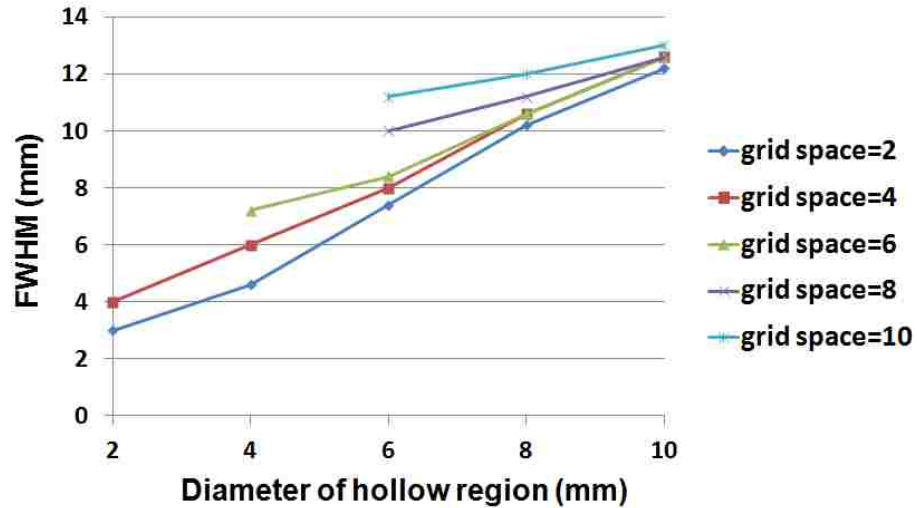
Figure 5.13: The FWHM of Jacobian across the profile line with changing hollow region size and different grid sizes. B-Spline grid sizes are changing from 2 mm to 10 mm, and the diameters of hollow region are increasing from 2 mm to 10 mm.

The second set of experiments are performed on real lung CT images. Based on the vessel segmentation used in Section 3.4, skeletonization is performed to find the centerline of the vessel tree. At each vessel location, profile lines along x-direction and y-direction are defined. Smaller FWHM of Jacobian along one of these two profile lines is chosen. Figure 5.14 shows the FWHM of Jacobian with varying vessel size and different grid sizes. B-Spline grid sizes are changing from 4 mm to 16 mm, and
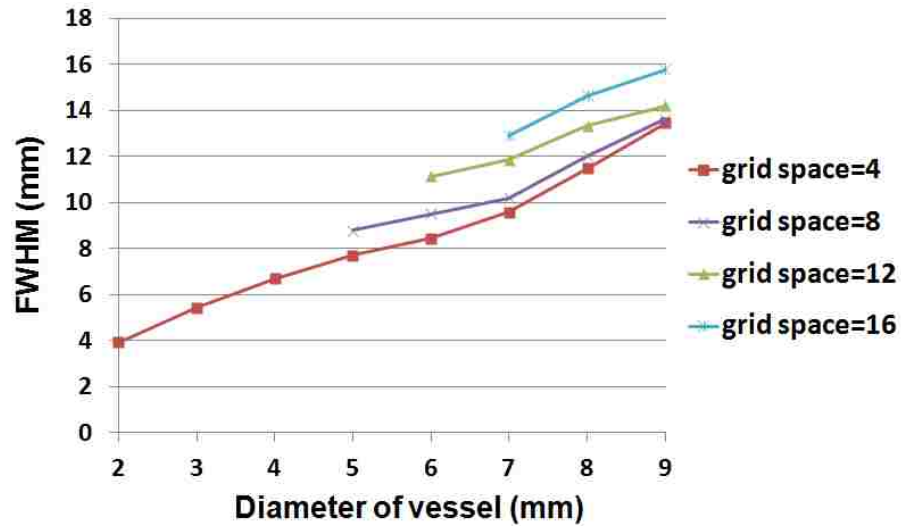
Figure 5.14: The FWHM of Jacobian with changing vessel size and different grid sizes. B-Spline grid sizes are changing from 4 mm to 16 mm, and the vessel diameters are increasing from 2 mm to 9 mm.

the vessel diameters are increasing from 2 mm to 9 mm. For a fixed vessel size, the FWHM value is averaged on all vessel locations which are within the size range across all six human subjects.

From Figure 5.13 and Figure 5.14, we can observe that finer grid spacing setting can better track the Jacobian change across different regions. To detect the mechanical quantity change of ROI with diameter less than 5 mm, finer B-Spline setting with grid size less than 4 mm is required. To study the mechanical quantities of larger ROIs, B-Splines of grid size 8 mm is a good choice when considering both the accuracy factor and optimization size problem.

5.8 Summary

In this chapter, we establish methods to estimate local mechanical quantities of lung tissue. Specific volume change are used to quantify the magnitude of regional lung function during respiration process. The regional map of maximum principal strain deviated from that of regional deformation because the former is elevated in regions where the deformation is predominantly along one direction. Anisotropy analysis reflects different tissue deformation patterns related to their locations. Combining the deformation magnitude, principal stretch directions, and distortion index together, we are able to establish a more complete studies of the lung mechanical quantities.

We also investigate the sensitivity of Jacobian measurement to the displacement noise, the underlying region size, and B-Spline grid space. The analysis results indicate that larger grid space is good for measurement robustness and reliability, while smaller grid space is good for feature detection. B-Spline grid space should selected by compromise between the two factors. When the registration error is acceptable, B-Splines of grid space 4 mm is sometimes necessary to detect the property changes of small features. However, if the registration accuracy is not satisfying enough, using B-Spline of grid space 8 mm may generate more reliable results.

CHAPTER 6
DEMONSTRATE PULMONARY MECHANICAL CHANGES WITH THE APPLICATION OF LUNG FOLLOWING BRONCHOALVEOLAR LAVAGE

6.1 Introduction

Once we determine that our measurement of regional lung mechanical parameters can be used to detect and follow the changes of regional lung function, we aim to extend these studies to abnormal data. In this specific aim, we will examine the practical application of utilizing image registration to measure regional lung mechanical parameters and tissue content following the changes introduced by the bronchoalveolar lavage (BAL).

Bronchoalveolar lavage (BAL) has important clinical usage and is typically used to diagnose lung diseases, such as infections [54], lung cancers, and interstitial lung disease. During the BAL procedure, a bronchoscope is passed through the mouth or nose into the lungs, and fluid is squirted into a small part of the lung and then recollected for examination.

For those unrecollected BAL, it is of great interest to understand the progress of its distribution and resolution. Kelly et al. [74] used a digital subtraction technique to visualize the anatomical distribution of saline containing a low concentration of radio-opaque dye. Chen et al. [50, 17] showed that the extent and frequency of defects tended to decrease with time, and cleared after approximately 24 hours. In addition, the change of lung function due to BAL procedure is important for studying the

effect of unretrived BAL. Baughman et al. [8] demonstrated that lung mechanics can be significantly altered in an hour or longer after BAL. However, few studies have tracked the resolution process of unretrived BAL and quantified the BAL effects on lung ventilation function at a regional level.

Multidetector-row computed tomography (MDCT) can be used to acquire multiple static breath-hold CT images of the lung taken at different lung volumes. Applying image registration techniques on the CT data, we are able to find dense deformation fields that transform the lungs between different lung volumes. The transformations can be analyzed to calculate voxel-by-voxel density change, estimate local lung tissue expansion, and make other biomechanical measurements. When combined with image segmentation results, functional and biomechanical measurements can be reported on a lung, lobe, and any arbitrary-shaped subregion basis [92].

Hoffman et al. [60] used CT density measurements to calculate regional tissue and air content of the lung. This method has been shown to reflect tissue density accurately and estimate regional ventilation effectively [43, 122]. Christensen et al. and Reinhardt et al. have estimated rates of local tissue expansion and contraction using a Jacobian-based ventilation measure [27, 92]. These local measurements of tissue content and ventilation function can be utilized with image registration technique to track tissue volume change and mechanical quantity change regionally over time.

In this aim, we will examine our image registration based method to quantitatively track the resolution process of unretrieved BAL and measure regional lung ventilation function during 24 hours after BAL procedure. Unretrieved BAL leads

to transient areas of atelectasis, and thus alter the local mechanical quantities of the lung. Our main tasks are:

- Tracking the tissue (non-air) volume change over time to observe the BAL resolution process.

- Tracking the regional mechanical quantities change over time to observe the mechanical alternation in lung, and demonstrate the regional pulmonary function will recover as BAL fluid resolved.

6.2   Data Sets

The protocol was reviewed and approved by the University of Iowa Institutional Review Board. CT data sets from six healthy human subjects will be used. Each subject were scanned at four time points: baseline, immediate post-lavage (within 30 minutes), 4 hours post-lavage, and 24 hours post-lavage. At each time point a pair of FRC and TLC scans were acquired. Therefore, each subject experienced totally eight CT scans from four phases during a 24-hour period. Each scan pair was acquired with a Siemens Sensation 64 multi-detector row CT scanner (Forchheim, Germany) during breath-holds in the same scanning phase. Each volumetric data set was acquired at a section spacing of 0.5 mm and a reconstruction matrix of 512×512. In-plane pixel spacing is approximately 0.6 mm $\times$ 0.6 mm. Scans were reconstructed using a B31f reconstruction kernel. Table 6.1 lists the data sets acquired for each subject in four phases and the name of each scan used in this paper. Figure 6.1 shows the lung volumes at FRC and TLC pressures, and the volume

difference between FRC and TLC scans in each phase for six subjects.

Table 6.1: Eight CT scans acquired from four phases for each subject.

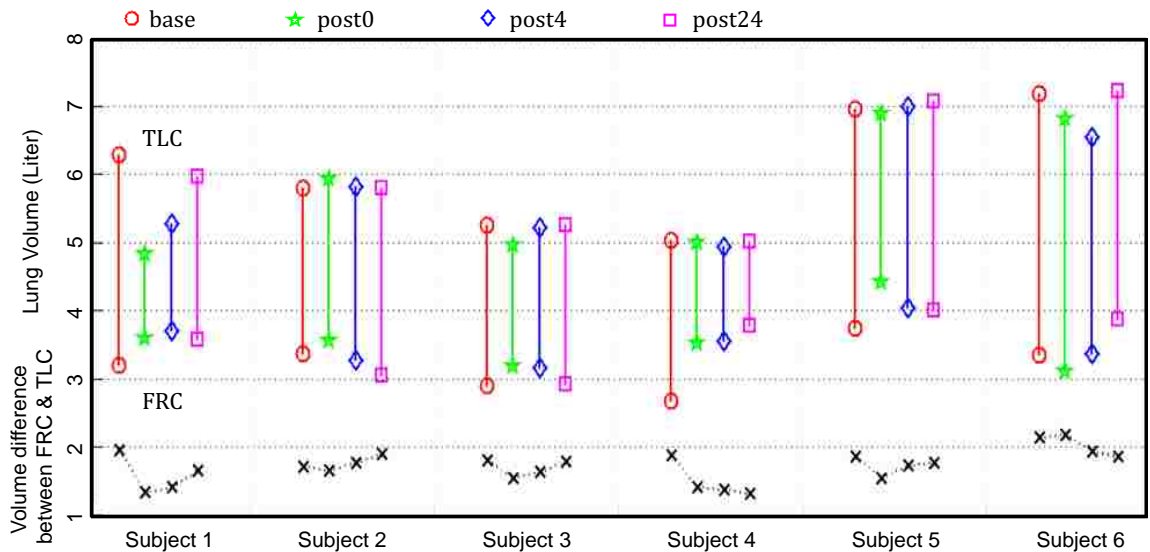|	Baseline	0 h after BAL	4 h after BAL	24 h after BAL
FRC scans	baseFRC	post0FRC	post4FRC	post24FRC
TLC scans	baseTLC	post0TLC	post4TLC	post24TLC

Figure 6.1: Lung volumes at FRC and TLC pressures, and the volume difference between FRC and TLC scans in each phase for six human subjects.

Subjects were lavaged in the right middle lobe and ligula. Each subject received aliquots of 300 mL in total; the total amount is denoted as $VBAL_{total}$. BAL

fluid was also retrieved and measured by the bronchoscopist during this procedure; the retrieved amount is denoted as $VBAL_{retrieved}$. Then the subjects underwent the post-lavage scan within 30 minutes of lavage (post0 phase scans). The volume of unretrieved BAL fluid $VBAL$ can be calculated by subtracting the volumes delivered with the volumes retrieved, as shown in Equation 6.1. The calculated $VBAL$ for each subject is shown in Table 6.2. Note that subject 2 was observed to cough a significant amount of BAL fluid out of the lungs.

$$VBAL = VBAL_{total} - VBAL_{retrieved} \tag{6.1}$$

The lung regions in all images are identified using the Pulmonary Workstation 2.0 (VIDA Diagnostics, Inc., Iowa City, IA). For the baseline TLC image of each subject, an automatic lobe segmentation algorithm [115] is used to segment the parenchyma regions into five different lobes.

6.3   Method Overview

Our goal is utilizing registration results to track non-air volume change and tissue ventilation change regionally during 24 hours after BAL procedure. Figure 6.2 shows a block diagram of the entire process. Two types of registration are performed on the CT data sets. The first one is intra-phase registrations, which register the FRC image to the TLC image within a phase. These results are used to estimate local lung functions in each phase and make comparison between different phases to measure the function change. The second one is inter-phase registrations, which register all TLC image in post-lavage phases to baseline TLC. These results are used to track

local tissue (or non-air) content change across four different phases.
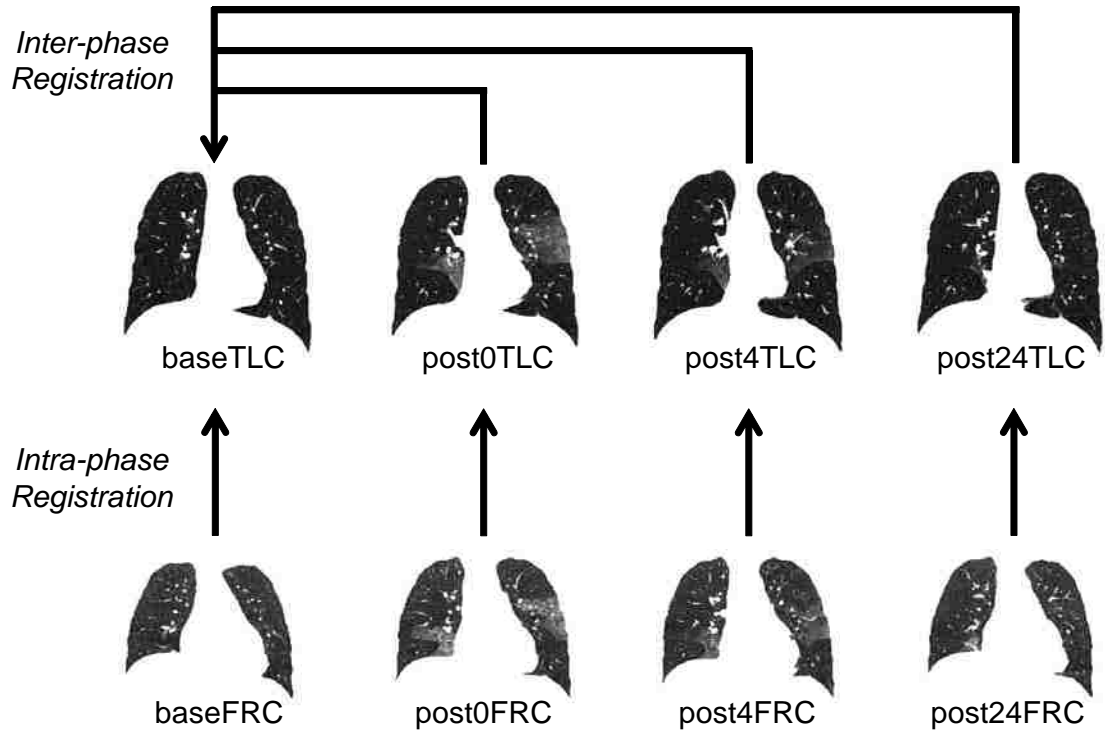
Figure 6.2: Framework of the registration-based method. For each subject, intra-phase registrations register the FRC image to the TLC image within a phase; inter-phase registration register all TLC images in post-lavage phases to baseline TLC.

6.4 Intra-phase and Inter-phase Registration

For each subject, two different kinds of registrations were performed. One is intra-phase registration, which matches a FRC data to its according TLC data in the same phase. The other registration is inter-phase registration, which matches the TLC data in post-lavage phases to the baseline TLC data. Different registration

algorithms were used to perform intra-phase and inter-phase registrations.

For a pair of FRC and TLC scans in the same phase, the time interval of acquisition can be ignored and the tissue volume is assumed unchanged. Therefore, the registration can be driven by preserving tissue volume in two images. As discussed in Section 2.5, the sum of squared tissue volume difference (SSTVD) metric [122] accounts for the variation of intensity in the lung CT images during respiration. Feature-based vesselness similarity metric and Laplacian constraint are also used during registration process to improve accuracy and help produce smooth displacements. For each intra-phase image pair, the regularized tissue volume and vesselness measure preserving image registration [16] is used to estimate the transformations from FRC to TLC in the same phase, from which we can calculate the mechanical parameters voxel-by-voxel. The total cost is defined as a linear combination of the tissue volume preserving metric, vesselness preserving metric and Laplacian constraint

$$C_{\text{INTRA-TOTAL}} \quad = \quad \rho C_{\text{SSTVD}} + \chi C_{\text{SSVMD}} + \gamma C_{\text{LAP}}. \tag{6.2}$$

Constants ρ, χ and γ are weights to adjust the significance of the three terms. In the experiments, the weighting constants were set as $\rho = 1$ and $\chi = 1$, and $\gamma = 0.1$ for all intra-phase registrations.

Since the BAL fluid were resolved during 24 hours after lavage, the tissue volume (non-air volume) was changing across different phases. Therefore, tissue volume preserving is not valid in the case when register TLC scans from post-lavage phases to baseline TLC scan. To reflect voxel-based pulmonary function change in post analysis, a similarity criterion which is able to estimate local similarities is needed.

As discussed in Section 2.5, a simple metric is the sum of squared difference (SSD), which measures the intensity difference at corresponding points between two images. Considering the change in CT intensity due to different air content and BAL effect, the grayscale range were different within the lung region in two TLC images acquired at different phases. To balance this grayscale range difference, normalization of the intensities are needed. A histogram matching procedure is used before SSD driven registration to modify the histogram of template image so that it is similar to that of target image. The inter-phase TLC scans matching uses a regularized intensity and vesselness preserving nonrigid registration. The transformation is derived by minimizing the sum of squared intensity difference (after histogram matching), the sum of squared vesselness measure difference, and the Laplacian constraints. The total cost function

$$C_{\text{INTER-TOTAL}} \quad = \quad \rho C_{\text{SSD}} + \chi C_{\text{SSVMD}} + \gamma C_{\text{LAP}}. \tag{6.3}$$

In the experiments, the weighting constants were set as $\rho = 1$ and $\chi = 2$, and $\gamma = 10$ for all inter-phase registrations. Details of other components design in intra-phase and inter-phase registration algorithms are described in Chapter 2.

6.5   Tracking Lung Tissue Volume Change

For each subject, inter-section registrations warp all post-lavage TLC images to baseline coordinate, and provide voxel-wise deformation mappings from baseline phase to three post-lavage phases. These mappings enable us to assess the tissue volume change for a given voxel position across the four phases.

We assume that the is mainly contributed by tissue and air. Following Equation 2.5 and 2.6, we can estimate regional tissue volume and air volume from HU of lung CT images. The tissue volume in a region R is calculated as

$$TV = \int_{\mathbf{R}} V(\mathbf{x})d\mathbf{x} = \int_{\mathbf{R}} v(\mathbf{x})\beta(I(\mathbf{x}))d\mathbf{x}. \tag{6.4}$$

Let $\mathbf{h_1}$, $\mathbf{h_2}$ and $\mathbf{h_3}$ be the transformation from baseTLC to post0TLC, baseTLC to post4TLC, and baseTLC to post24TLC, respectively. Then for a region located at $\mathbf{x}$ defined in baseTLC, its corresponding location in post0TLC, post4TLC, and post24TLC can be tracked through $\mathbf{h_1}$, $\mathbf{h_2}$ and $\mathbf{h_3}$, respectively. The volumes of the same region in the four images are $v(\mathbf{x})$, $v(\mathbf{x})J(\mathbf{h_1}(\mathbf{x}))$, $v(\mathbf{x})J(\mathbf{h_2}(\mathbf{x}))$ and $v(\mathbf{x})J(\mathbf{h_3}(\mathbf{x}))$. The volumes can be decomposed into the tissue volume fraction and air volume fraction based on the mean voxel intensity within the cube. Based on Equation 2.5, the tissue volumes are calculated as $v(\mathbf{x})\beta(I_0(\mathbf{x}))$, $v(\mathbf{x})J(\mathbf{h_1}(\mathbf{x}))\beta(I_1(\mathbf{h}(\mathbf{x}))$, $v(\mathbf{x})J(\mathbf{h_2}(\mathbf{x}))$ $\beta(I_2(\mathbf{h}(\mathbf{x}))$ and $v(\mathbf{x})J(\mathbf{h_3}(\mathbf{x}))\beta(I_3(\mathbf{h}(\mathbf{x}))$, respectively. Here J is denoted as the Jacobian of the transformations; I_0, I_1, I_2, I_3 are intensity function of the four images. As the ratio of tissue to air increases, the CT intensity of a voxel increases (getting brighter). In this way, we are able to track tissue volume of any subregion across the four phases using inter-phase registration results.

The total tissue volume in a region can be integrated using Equation 6.4. In the same region R defined on baseline coordinate. let TV_0, TV_1, TV_2 and TV_3 represent the total tissue volume from baseTLC, post0TLC, post4TLC and post24TLC,

respectively. They are calculated as

$$
\begin{aligned}
TV_0 &= \int_{\mathbf{R}} v(\mathbf{x})\beta(I_0(\mathbf{x}))d\mathbf{x} \\
TV_i &= \int_{\mathbf{R}} v(\mathbf{x})J(\mathbf{h_i}(\mathbf{x}))\beta(I_i(\mathbf{h_i}(\mathbf{x})))d\mathbf{x}, \quad i = 1, 2, 3.
\end{aligned} \tag{6.5}
$$

Meanwhile, we define TVC_1, TVC_2 and TVC_3 as the index of tissue volume change for three post-lavage phases when compared with base phase, and also define $TVCR_1$, $TVCR_2$ and $TVCR_3$ as the index of tissue volume change ratio. They are formulated as follows

$$
TVC_i = TV_i - TV_0, \quad TVCR_i = \frac{TV_i - TV_0}{TV_0} \times 100\%, \quad i = 1, 2, 3. \tag{6.6}
$$

6.6 Tracking Lung Mechanical Alternations

As described in Fraction 5, lung mechanical parameters extracted from registration results are calculated in this work to estimate lung mechanical changes.

The lung tissue deformation pattern is an index to assess lung function. As discussed in Section 3.7, the Jacobian determinant of the transformation field derived by image registration is used to estimate the local tissue expansion and contraction [92]. Across different phases, the Jacobian estimates are related to two factors. The first factor is the unretrieved BAL. The lung function of regions with BAL will decrease compared with baseline state. The second factor is the breathing efforts. As shown in Figure 6.1, saline fluid retained in the lung after BAL procedure may cause smaller breathing efforts, i.e., smaller volume change from FRC to TLC. Smaller volume change results lower lung function in average. In order to focus our analysis on how the unretrieved BAL affect the lung function, we eliminate the breathing efforts factor

by calculating the cumulative distribution function (CDF) of the Jacobian estimates.

In our case, CDF of Jacobian describes the probability that Jacobian values will be found less than or equal to a given value. Intuitively, it is the "area so far" function of the probability distribution. It can be viewed as "rank" information: a CDF of 1 means rank top (largest Jacobian), while a CDF value of 0 means rank bottom (smallest Jacobian). In the following description, we call the CDF of Jacobian as rank for convenience. Regardless of different overall volume changes, regions with higher lung function corresponds to higher rank. In this way, we eliminate the breathing efforts factor while comparing lung function change caused by unretrieved BAL fluid. Let $Rank_0$, $Rank_1$, $Rank_2$ and $Rank_3$ represent the rank of Jacobians estimated from base, post0, post4 and post24 phases, respectively. Then the rank change RC is defined as

$$RC_i = Rank_i - Rank_0, \quad i = 1, 2, 3. \tag{6.7}$$

Besides the deformation index, regional ventilation, strain and anisotropy index can be calculated from dense displacement fields. Similarly, in order to eliminate the effect of different breathing efforts, CDF of these parameters are needed to make a fair comparison between different phases. Rank changes of these mechanical parameters within lavage region and non-lavage region is of great interest to quantify the unretrieved BAL effect on lung function.

6.7 Experiments and Results

6.7.1 Assessment of Registration Accuracy

Registration outcome can be judged by observers through visual assessment. Visualization of the image intensity matching is the most intuitive method to determine how well the region boundaries and corresponding structures are aligned. Examples of inter-phase and intra-phase registration results are shown in Figure 6.3. Figure 6.3 (a)-(e) show the matching results of inter-phase registration. Matching results of intra-phase registration between baseTLC and baseFRC are shown in Figure 6.3 (f)-(j). It is obviously to see that besides the lung boundaries, important structures such as airway, vessel and fissure locations are aligned well after registration.

For each subject, 20 anatomic landmarks were manually selected and tracked in all eight images during four phases. These landmarks were chosen as recognizable airway branchpoints, as shown in Figure 6.4.

Registration accuracy is quantitatively assessed by tracking movement these landmarks on TLC images across four phases, and between FRC and TLC images within the same phase. Boxplot of the landmark tracking error of both inter-phase and intra-phase registrations over six subjects are shown in Figure 6.5. The mean landmark tracking error across six subjects is $0.70 \pm 0.34mm$ for inter-phase registration, and $0.86 \pm 0.50mm$ for intra-phase registration. These mean errors are within sub-voxel range, which indicates registrations achieve good accuracy and is able to catch lung deformations within the same phase and between different phases.

(a) baseTLC (b) post0TLC (c) deformed post0TLC

(d) fused before inter-phase reg (e) fused after inter-phase reg

(f) post0TLC (g) post0FRC (h) deformed post0FRC

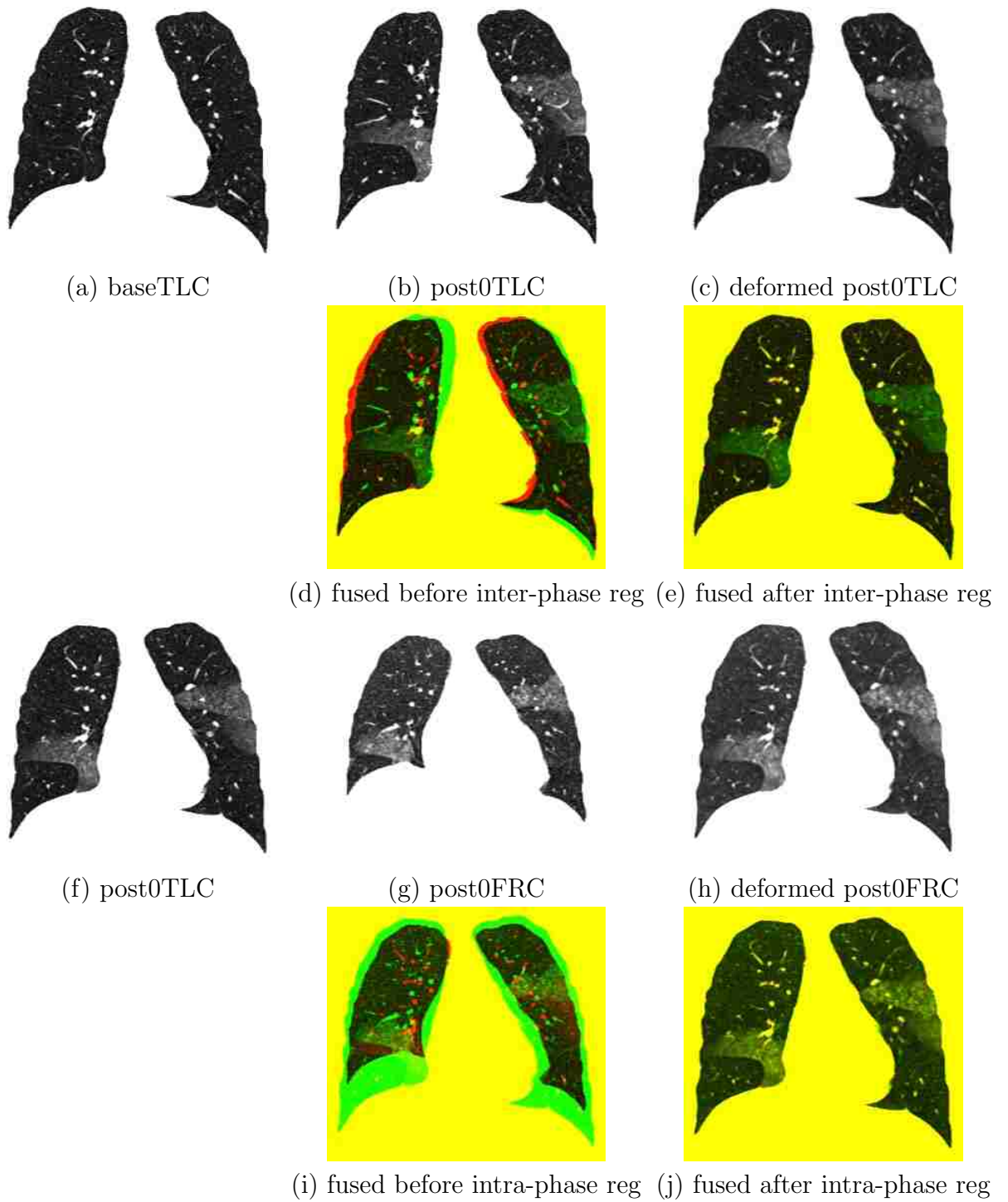(i) fused before intra-phase reg (j) fused after intra-phase reg

Figure 6.3: Example of registration results on BAL data. Matching results of inter-phase registration are shown in (a) – (e). Matching results of intra-phase registration are shown in (f) – (j).
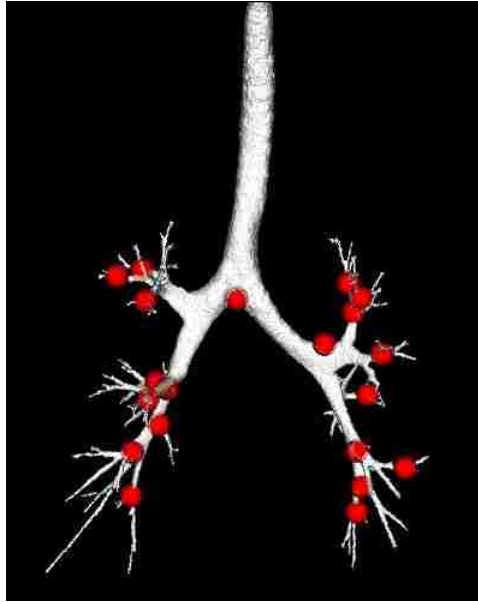
Figure 6.4: Distribution of landmark positions (red points) selected on the airway tree segmented out from the baseTLC image of one human subject.

6.7.2 Assessment of Unretrieved BAL

According to the protocol of experiments, the quantitative assessment of tissue volume change between baseline phase and post0 phase should be correlated with unretrieved BAL fluid from bronchoscopist reported data [43]. From Equation 6.1, $VBAL$ is calculated from Bronchoscopist-reported volumes instilled and retrieved during BAL procedure. From Equation 6.6, the tissue volume change calculated between baseTLC and deformed post0TLC to baseline coordinate is defined as TVC_1. Experiments to find the relationship of the quantitative assessment and clinical data are performed. The correlation coefficients between $VBAL$ and TVC_1 is calculated by linear regression.
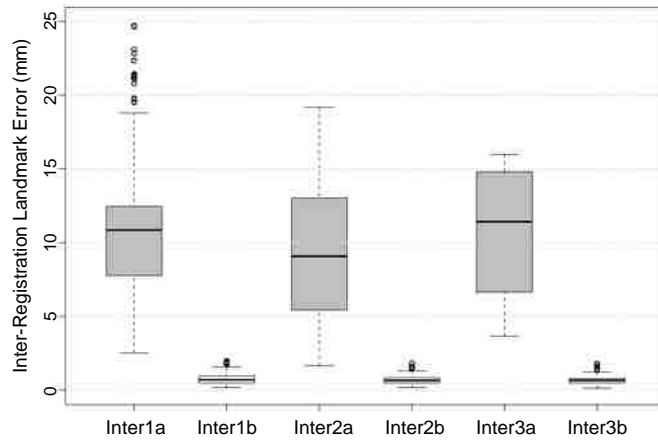
(a) Boxplot of landmark error for inter-phase registrations.
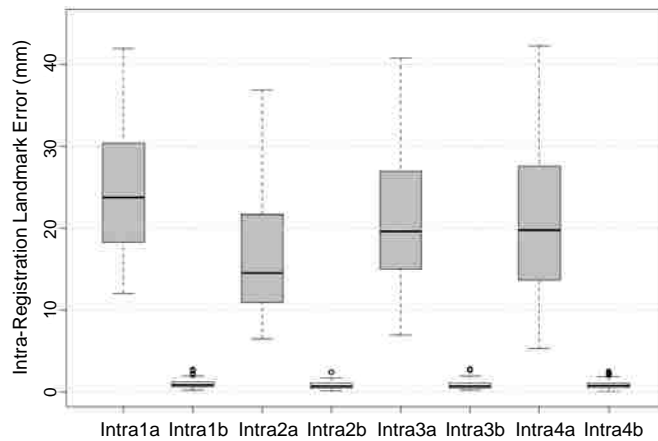
(b) Boxplot of landmark error for intra-phase registrations.

Figure 6.5: Registration accuracy on airway landmarks. (a) Boxplot of landmark error for inter-phase registrations. Inter1a, Inter2a and Inter3a denote the error from post0TLC, post4TLC, and post24 TLC to baseTLC before registration, respectively. While Inter1b, Inter2b and Inter3b denote the error after three inter-phase registrations. (b) Boxplot of landmark error for intra-phase registrations. Intra1a, Intra2a, Intra3a, and Intra4a denote the error from baseFRC to baseTLC, from post0FRC to post0TLC, from post4FRC to post4TLC, and from post24FRC to post24TLC before registration, respectively. While Intra1b, Intra2b, Intra3b and Inter4b denote the error after four intra-phase registrations.

Table 6.2 lists the volume of unretrieved BAL fluid $VBAL$ and tissue volume change TVC_1 for each subject. We noticed that TVC_1 is always lower than $VBAL$, which may due to the fluid resolution during the time interval between lavage and the first post-lavage scan (within 30 minutes). The linear regression line and correlation coefficient are shown in Figure 6.6 (a). The correlation coeffient is $R^2 = 0.81$ with a slope of 0.83. As noted, subject 2 was observed to cough a significant amount of BAL fluid out of the lungs, which are not collected during lavage process. Then it reasonable to remove this subject for the linear regression analysis. The linear regression line and correlation coefficient after removing data from subject 2 is shown in Figure 6.6 (b). The correlation coefficient is increased significantly to $R^2 = 0.94$ with a slope of 0.98.

Table 6.2: Reported and calculated BAL volumes (mL).

Subjects	$VBAL$	TVC_1
1	147	125.48
2	160	107.80
3	110	106.16
4	151	130.00
5	150	123.37
6	68	42.03
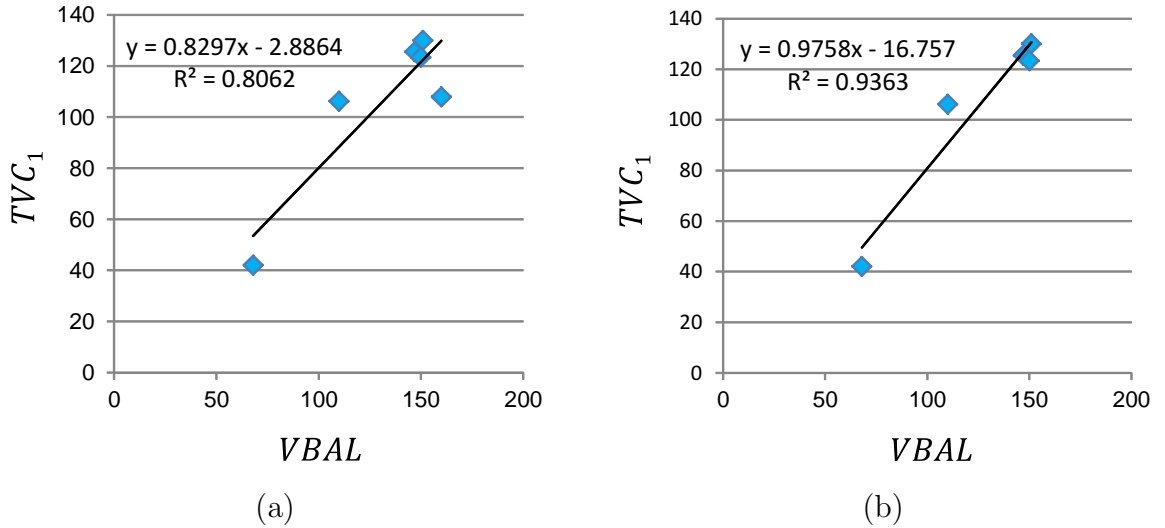
Figure 6.6: Correlation between reported BAL volumes and calculated BAL volumes. (a) shows the linear regression using data from all six subjects. (b) shows the linear regression using data from five subjects after removing subject 2.

6.7.3 Tracking Tissue Volume Change

In Equation 6.5, we can calculate the tissue volume in the same arbitrary-shaped region R (defined on baseline phase) at different phases. Substituting R with the baseline whole lung segmentation, we are able to track the global tissue volume change using Equation 6.6. The mean tissue volume change ratio to baseline state is $14\% \pm 5.41$ at post0 phase, then it drops to $7\% \pm 4.59$ at post4 phase, and finally decreases to $1\% \pm 2.64$ at post24 phase. This indicates that the fluid is continuously resolved during the 24 hours after lavage. After 24 hours, most lavage fluid is resorbed and the lung tissue volumes return to baseline state.

For each scan pair of baseline data, the lung is segmented into five different

lobes. Thus substituting R in Equation 6.5 with five different lobe segmentations, we are able to track the lobe-based tissue volume change over time using Equation 6.6. Figure 6.7 shows the lobe-based tissue volume change ratio over different phases averaged across six subjects. The right middle lung and left upper lung have the largest tissue volume change after lavage. This is because lavage fluid was delivered to the two lobes. However, other three lobes also experience tissue volume increase, which indicates the fluid is re-distributed among different lobes. After 24 hours, most lavage fluid is resorbed and the tissue volume of all lobes return to baseline state.
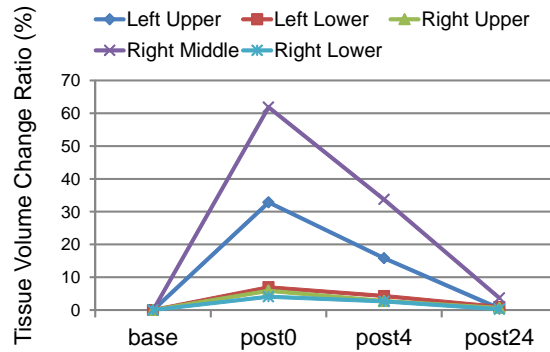
Figure 6.7: Tissue volume change ratio over different phases for five lobes average across six subjects.

6.7.4 Tracking Regional Lung Deformation Change

For each intra-phase registration, we calculate the voxel-wise Jacobian from the transformations as an index of lung expansion and contraction, which reflects the

local lung function during the respiration process. In order to observe the regional lung function tendency, we divide the lung into 30 rectangular-shaped slabs from dorsal to ventral lung, and from apex to base lung. The average Jacobian is calculated within each slab, and plotted in Figure 6.8. Each color-coded line shows the Jacobian estimated from one intra-phase registration. The mean Jacobian in each slab is high at baseline, then drops dramatically at post0 phase, and increases a level at post4, and finally returns to the baseline state at post24 phase. This is because with fluid in the lung, all subjects except subject 6 have smaller inspiration efforts immediately after lavage, as shown in Figure 6.1. As the fluid resolves, the lungs return to normal state and have similar breathing efforts with baseline state. As a result, the lung function recovers with the same inspiration efforts, shown as the overlap between blue line (baseline) and purple line (post24 phase) in Figure 6.8. We also noticed that there are gradients for each mean Jacobian curve from dorsal to ventral along lung height, and from apex to base along lung length. With different lung volume change, regions with larger lung function (dorsal lung and base lung) are affected more than other regions.

Combine intra-phase and inter-phase registration together, we can bring Jacobian estimates in different phases into the same baseline coordinate, and then make comparison easily. Figure 6.9 gives an illustration of Jacobian and its rank (CDF) distribution on a transverse slice defined in baseTLC coordinate. The left column shows its intensity pattern over four different phases; the middle column shows the corresponding Jacobian maps in each phase; and the right column shows the cor-

(a)
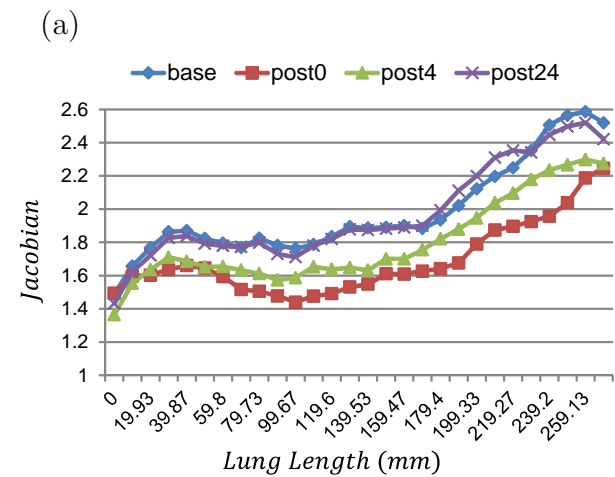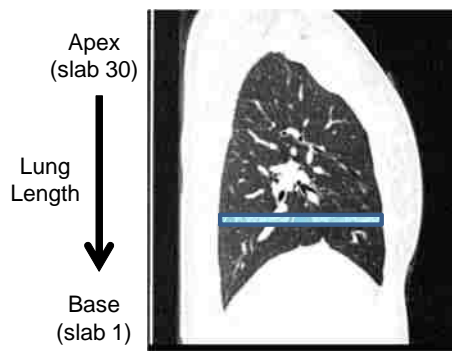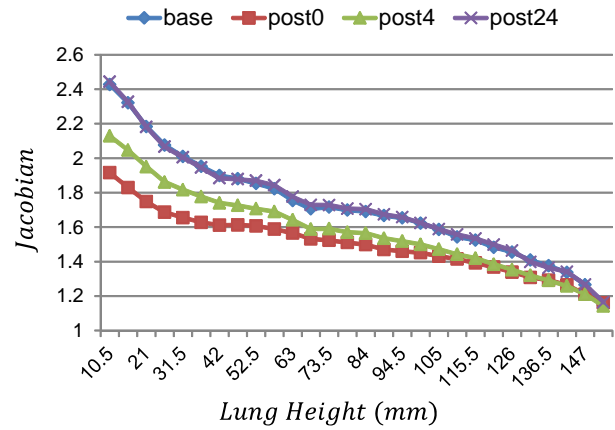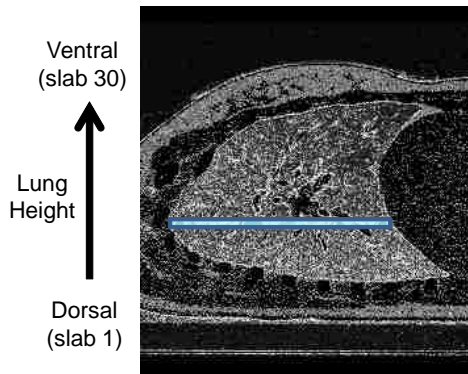
(b)

Figure 6.8: Lung expansion pattern within each phase for one subject. (a) shows the slab division scheme from dorsal to ventral lung, and the corresponding mean Jacobian in each slab over four phases. (b) shows the slab division scheme from apex to base lung, and the corresponding mean Jacobian in each slab over four phases.

responding rank maps of Jacobian estimates. The fluid delivering and resolving is clearly seen in the intensity image. Jacobian maps show the function decrease in post0 and post4 phases, and recovers in post24 phase. The rank maps show that at post0 and post4 phases, the rank for non-lavage region is almost unchanged, but the lavage region is significantly decreased. Also, after 24 hours, the rank for each region is recovered.

As shown in Figure 6.9 (d), the region with unretrieved BAL (lavage region) has much higher intensity than other regions. This intensity difference enable us to segment the lavage region manually. Then we observe the regional function change over time by tracking the rank change of Jacobian estimates over four phases within lavage region and non-lavage region, as shown in Figure 6.10. The lavage regions has around 6% function rank decrease immediately after lavage, while non-lavage regions have a little increase in contrast. Those rank changes disappear after 24 hours.

6.8   Summary

In this chapter, we apply our registration method and lung function measures to study the lung mechanics changes induced by BAL. Different algorithm designs are used for intra-phase and inter-phase registrations. Validation by tracking landmark movement shows that both inter-phase and intra-phase registration achieve good accuracy. Tissue (non-air) volume changes are assessed by intensity information and registration mappings. Inter-phase registration can be used to track tissue volume change in any arbitrary-shaped lung regions through all the phases. Jacobians esti-
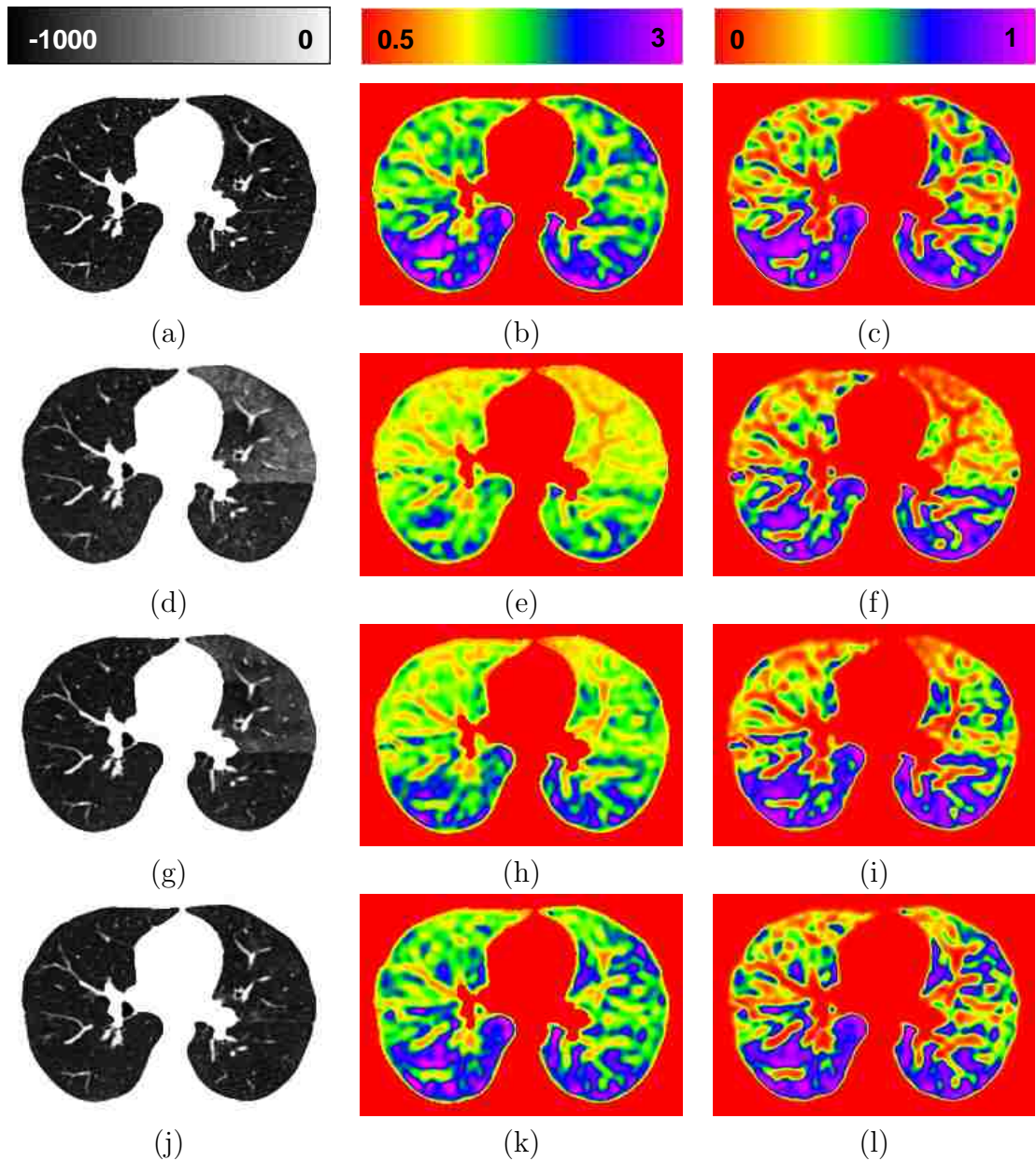
Figure 6.9: Comparison of local lung function estimates over different phases. (a), (d), (g) and (j) show the intensity pattern on the same slice from baseTLC, deformed post0TLC to baseTLC, deformed post4TLC to baseTLC, and deformed post24TLC to baseTLC, respectively. (b), (e), (h) and (k) show the Jacobian maps estimated from four phases on the slice. (c), (f), (i) and (l) show the corresponding rank maps of Jacobian estimates.
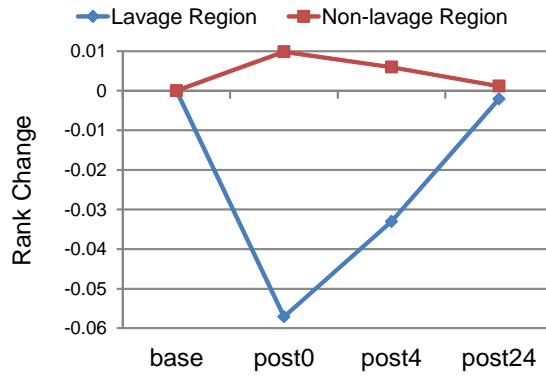
Figure 6.10: Observance of regional function change over time by tracking the rank change of Jacobian estimates over four phases within lavage region and non-lavage region.

mated from intra-phase registration are used to measure lung mechanical function. The cumulative density function (CDF) of Jacobian gives us a rank information of Jacobian, which eliminate the affect of different breathing efforts. Combining inter-phase and intra-phase registrations together, we are able to track lung function change through different phases at a local region level.

In this application, we demonstrate the ability to measure tissue volume change using registration-based method and to observe the BAL resolution and mechanical alternations over time globally and regionally. Based on the content described in the previous chapters, we present an example study to understand the changes of local lung mechanical quantities using nonrigid registration on lung CT images.

CHAPTER 7
CONCLUSION AND FUTURE DIRECTIONS

7.1   Conclusion

Image registration is an important research area within pulmonary image analysis. Accurate image registration is a challenging problem when the lungs have large volume change. Registration results estimate the local tissue movement and can be utilized to study lung mechanical quantities. In this thesis, we proposed a new volumetric registration algorithm, and a registration scheme combining both surface and volumetric registrations to solve lung CT matching problems. Approaches to study lung functions were discussed and presented through a practical application on studying changes of lung mechanical quantity.

In Chapter 2, we developed a nonrigid, regularized registration utilizing intensity and feature information. This registration scheme was suitable for register lung CT scans and catching lung motions. The tissue preserving method was specific for matching lung CT image since it accounted for the local intensity changes between images from the same subject. The feature-based similarity metric enhanced the cost contribution at vessel locations and helped guide lung CT registration during the volumetric matching procedure. A linear elastic operator was used to constrain the transformation not changing abruptly. The weighting effects for different costs were studied and appropriate parameter settings were selected. A good registration is tend to achieve lower intensity and vesselness discrepancies with acceptable level

of smoothness cost.

The effect of the newly proposed feature-based vesselness metric was validated in Chapter 3. After adding vesselness metric to different intensity-based metrics, we demonstrated the accuracy improvement on matching landmarks, vessel trees and fissure planes. Vesselness constraint helped different intensity-based registration methods to generate more consistent results, which were more reliable to estimate local lung function.

However, the volumetric registration method introduced in Chapter 2 encountered mismatching problem for some complex registration problem. In order to overcome these problems, Chapter 4 described a new registration framework utilizing both surface and volumetric registration. In this work flow, surface matching was performed firstly to compute the boundary correspondences. Using element free Galerkin method based on WEB-Splines, the boundary correspondence can be extended internally into the entire object domain. WEB-Splines have some good properties such as only nonzero values inside the object and excluding outer splines by assign its contribution to its closest set of inner splines. These properties enable us to represent arbitrarily shaped domain and ensure the stability of Galerkin framework. The extended displacements were used to initialize the intensity and feature based registration. Validation results showed our new scheme was able to overcome the mismatching problem when matching FRC data to TLC data.

After solving the registration problem, we discussed some methods to study lung function and mechanical quantities regionally in Chapter 5 utilizing the displace-

ment resulted from image registration. Specific volume change, strain descriptor, and anisotropic deformation index gave detailed information of lung tissue mechanics regionally. Analysis on Jacobian sensitivity to displacement noise and underlying feature size helped us to establish the measurement confidence interval for B-Splines with varying grid spaces.

Finally, we applied our registration and lung function estimation methods to study the lung function change induced by bronchoalveolar lavage. We registered image pairs scanned at different time points, and compared them to find the tissue volume and Jacobian changes during 24 hours. We observed those measurement changes regionally and globally, and demonstrated that the BAL was resolved and the lung function was recovered in 24 hours. This application was an example study to understand the local parenchymal tissue properties based on image registration of lung CT data.

7.2 Summary of Parameter Settings and Results

In the tissue volume and vesselness preserving registration, the parameters controlling the sensitivity of the vesselness measure in Equation 2.12 were set as $\alpha = 0.5$, $\beta = 0.5$, and $\gamma = 5$. The multiscale analysis expressed by Equation 2.13 used $\sigma_{min} = 2$ and $\sigma_{max} = 3$ in the experiments. In the regularization operator $L\mathbf{u}(\mathbf{x}) = -\alpha\nabla^2\mathbf{u}(\mathbf{x}) - \beta\nabla(\nabla \cdot \mathbf{u}(\mathbf{x})) + \gamma\mathbf{u}(\mathbf{x})$, we set $\alpha = 0.75$, $\beta = 0.25$, and $\gamma = 0$. Experiments have been done to test the appropriate setting of the cost weights in the total cost function $C_{\text{TOTAL}} = \rho C_{\text{INTENSITY}} + \chi C_{\text{SSVMD}} + \gamma C_{\text{REG}}$. From the experiments,

we may conclude that $\rho = 1$, $\chi = 0.5 - 1$ and $\gamma = 0.05 - 0.1$ is good for minimizing the three costs at the same time. An example of the spatial multiresolution scheme setting is listed in Table 2.3.

In the evaluation work of registration methods with/without vesselness metric, we showed the matching accuracy improved around 25% on the distributed landmarks and around 30% on the fissure planes by adding vesselness constraint. Higher matching accuracy on vessel trees and correlation between Jacobian and Xe-CT based specific ventilation were also achieved after using the vesselness preserving method. Our registrations captured the lung motion with average error within 1 mm on landmarks, vessels and fissure planes. The correlation of Jacobian and specific ventilation was around 0.9 using tissue volume and vesselness preserving method on one sheep data.

In the boundary-conditioned registration, the grid space was set to 12 mm or 16 mm considering the computation time and approximation accuracy in the WEB-Spline based EFGM interpolation process. Other settings of the volumetric registration were similar to the tissue volume and vesselness preserving registration. The multiresolution scheme can start from 1/4 or 1/2 of the full spatial resolution since the global motion has been captured through boundary matching and EFGM interpolation procedures. The validation results showed that compared to using volumetric registration only, the proposed boundary-conditioned registration improved the accuracy of global volume matching and alignment of regions around the base lung region.

In the analysis of mechanical quantities, we showed that the vessels had less expansion (average Jacobian of 1.28) than parenchyma tissues (average Jacobian of 1.91). The Fissures experienced more distortion (average distortion index of 2.34) than parenchyma tissues (average distortion index of 1.66). Combining the Jacobian, principal strain magnitudes and directions, and distortion index together helps us to establish a more complete studies of the lung mechanical quantities. The sensitivity studies of Jacobian measurement to the displacement noise, feature size, and spline grid space indicated that larger grid space is good for measurement robustness, while smaller grid space is good for small feature detection. When the registration error is acceptable and the size of ROI is smaller than 5 mm, splines of grid space less than 4 mm is necessary to detect the mechanical quantity changes of the ROI. On the other hand, if the registration accuracy is not satisfying enough, using splines of grid space larger than 8 mm may generate more reliable results.

In the application of observing fluid resolution and the mechanical alternations after BAL procedure, we demonstrated the ability to measure tissue volume and lung function change locally and globally based on our registration methods. We showed that the quantitative assessment of tissue volume change after BAL procedure and bronchoscopist reported unretrieved BAL fluid volume were highly correlated ($r^2 = 0.81$). The tissue volume change was decreased from 14% to 1% after 24 hours. The distribution of Jacobian from dorsal to ventral direction showed that the lung function was recovered during 24 hours after BAL.

7.3 Future Directions

The presented framework to study local lung functions using image registration technique can be extended on both methodology and applications.

The main idea of adding the vesselness metric is utilizing image information that can be extracted automatically. Fissures or other features information lie in the images can also be added into the registration, as long as the detection is reliable. For instance, in the tagged hyperpolarized Helium-3 MRI shown in Figure 7.1, the image contents appear in blobs. We can use similar way on extracting vesselness to compute blobness [33]. Then this feature information can be used to help match blob structures.

(a)   (b)
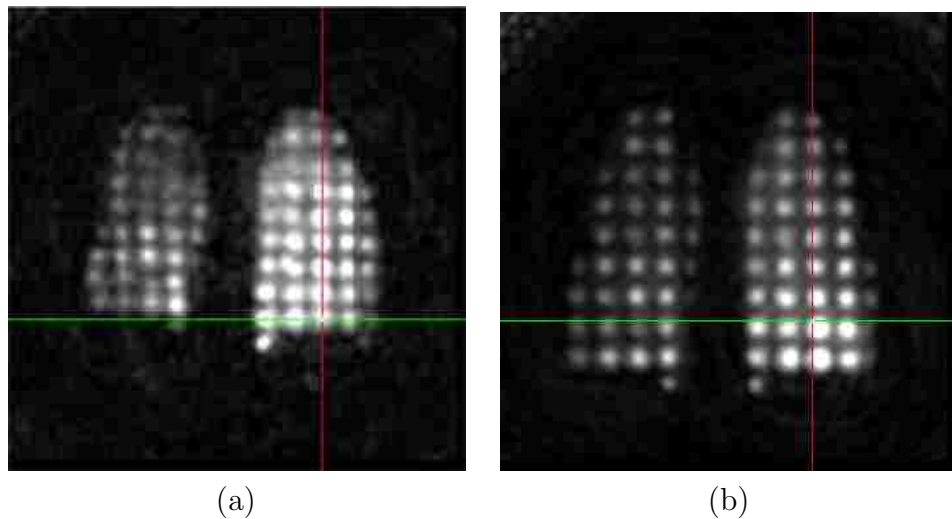
Figure 7.1: Helium-3 MRI data acquired at (a) end of exhalation and (b) end of inhalation on a coronal slice.

As we discussed in Chapter 4, the final step of volumetric registration can be parameterized using WEB-Spline when we have accurate boundary correspondence. Otherwise, it may impact the optimization of volumetric registration since the boundary is kept unchanged during the procedure. The method can be improved by incorporating the intensity feedback for updating the boundary correspondences. In addition, correspondences at internal features besides vessel locations can also be registered in the boundary matching step, and provide more accurate initialization.

Our methods have been successfully applied on sheep and human lung data. It can be tested on more data from different references, such as mouse, rat, dog, pig, and on other image modalities [72]. Registering the lung on a lobe-by-lobe basis allows discontinuities at fissure planes. The resulting displacements can be used to quantify the lobar sliding during the respiration [34, 5]. Nowadays 4D CT plays an important role in treatment planning for radiation therapy [29]. Applying our methods on 4D CT may help make more useful observations and bring our methodology closer to clinical application [32, 36, 35].

REFERENCES

[1] Lung volume. http://en.wikipedia.org/wiki/Spirometry (accessed April 15, 2011).

[2] Lung lobes. http://www.na-mic.org/Wiki/index.php (accessed April 15, 2011).

[3] Full width at half maximum. http://en.wikipedia.org/wiki/FWHM (accessed Jan 23, 2012).

[4] R. Amelon, K. Cao, K. Ding, G. E. Christensen, J. M. Reinhardt, and M. L. Raghavan. Three-dimensional characterization of regional lung deformation. *Journal of Biomechanics*, 44(13):2489 – 2495, 2011.

[5] R. Amelon, K. Cao, K. Du, K. Ding, J. M. Reinhardt, G. E. Christense, and M. L. Raghavan. Lobar sliding from registered CT scans of human lungs. In *Proc. SPIE*, volume accepted for publication, 2012.

[6] M. Anthea, J. Hopkins, S. Johnson, C. W. McLaughlin, M. Q. Warner, D. La-Hart, and J. D. Wright. *Human Biology and Health*. Prentice Hall Science, 2009.

[7] M. A. Audette, F. P. Ferrie, and T. M. Peters. An algorithmic overview of surface registration techniques for medical imaging. *Medical Image Analysis*, 4(3):201–217, 2000.

[8] R. P. Baughman. Technical aspects of bronchoalveolar lavage: recommendations for a standard procedure. *Semin Respir Crit Care Med*, 28(5):475–485, 2007.

[9] P. J. Besl and N. D. McKay. A method for registration of 3-D shapes. *IEEE Trans. Pattern Anal. and Machine Intelligence*, 14(2):239–256, 1992.

[10] R. C. Buck. *Advanced Calculus*. McGraw-Hill Book Company, St. Louis, 3 edition, 1978.

[11] R. H. Byrd, P. Lu, J. Nocedal, and C. Zhu. A limited memory algorithm for bound constrained optimization. *SIAM J. Sci. Comput.*, 16(5):1190–1208, 1995.

[12] J. Cai, K. Sheng, S. H. Benedict, P. W. Read, J. M. Larner, J. P. Mugler III, E. E. de Lange, G. D. Cates Jr., and G. W. Miller. Dynamic mri of grid-tagged hyperpolarized helium-3 for the assessment of lung motion during breathing. *Int. J. Radiat. oncol. Biol. Phys.*, 75(1):276 – 284, 2009.

[13] K. Cao, G. E. Christense, K. Ding, and J. M. Reinhardt. Intensity-and-landmark-driven, inverse consistent, B-Spline registration and analysis for lung imagery. In *Second International Workshop on Pulmonary Image Analysis*, pages 137–148, 2009.

[14] K. Cao, K. Ding, G. E. Christense, and J. M. Reinhardt. Tissue volume and vesselness measure preserving nonrigid registration of lung CT images. In *Proc. SPIE*, volume 7623, page 762309, 2010.

[15] K. Cao, K. Ding, G. E. Christensen, M. L. Raghavan, R. E. Amelon, and J. M. Reinhardt. Unifying vascular information in intensity-based nonrigid lung ct registration. In *4th International Workshop on Biomedical Image Registration*, LCNS 6204, pages 1–12. Springer, July 2010.

[16] K. Cao, K. Du, K. Ding, J. M. Reinhardt, and G. E. Christensen. Regularized nonrigid registration of lung CT images by preserving tissue volume and vesselness measure. In *Grand Challenges in Medical Image Analysis*, 2010.

[17] C. C. Chen, M. P. Andrich, and J. Shelhamer. Abnormalities on ventilation/perfusion lung scans induced by bronchoalveolar lavage. *J Nucl Med*, 34(11):1854–1858, 1993.

[18] Y. Choi and S. Lee. Injectivity conditions of 2d and 3d uniform cubic b-spline functions. *Graphical Models*, 62(6):411–427, 2000.

[19] D. Chon, B. A. Simon, K. C. Beck, H. Shikata, O. I. Saba, C. Won, and E. A. Hoffman. Differences in regional wash-in and wash-out time constants for xenon-CT ventilation studies. *Respiratory Physiology & Neurobiology*, 148:65–83, 2005.

[20] G. E. Christensen. Consistent linear-elastic transformations for image matching. In A. Kuba and M. Samal, editors, *Information Processing in Medical Imaging*, LCNS 1613, pages 224–237, Berlin, June 1999. Springer-Verlag.

[21] G. E. Christensen. Inverse consistent registration with object boundary constraints. In *Proceedings of the 2004 IEEE International Symposium on Biomedical Imaging: From Nano to Macro*, Arlington, VA, USA, April 2004. IEEE.

[22] G. E. Christensen and H. J. Johnson. Consistent image registration. *IEEE Trans. Med. Imaging*, 20(7):568–582, July 2001.

[23] G. E. Christensen, S. C. Joshi, and M. I. Miller. Volumetric transformation of brain anatomy. *IEEE Trans. on Med. Imaging*, 16(6):864–877, December 1997.

[24] G. E. Christensen, R. D. Rabbitt, and M. I. Miller. 3D brain mapping using a deformable neuroanatomy. *Physics in Medicine and Biology*, 39:609–618, 1994.

[25] G. E. Christensen, R. D. Rabbitt, and M. I. Miller. Deformable templates using large deformation kinematics. *IEEE Trans. Image Proc.*, 5(10):1435–1447, Oct 1996.

[26] G. E. Christensen, R. D. Rabbitt, M. I. Miller, S.C. Joshi, U. Grenander, T.A. Coogan, and D.C. Van Essen. Topological properties of smooth anatomic maps. In Y. Bizais, C. Braillot, and R. Di Paola, editors, *Information Processing in Medical Imaging*, volume 3, pages 101–112. June 1995.

[27] G. E. Christensen, J. H. Song, W. Lu, I. El Naqa, and D. A. Low. Tracking lung tissue motion and expansion/compression with inverse consistent image registration and spirometry. *Medical Physics*, 34(6):2155–2165, June 2007.

[28] M. M. Coselmon, J. M. Balter, D. L. McShan, and M. L. Kessler. Mutual information based CT registration of the lung at exhale and inhale breathing states using thin-plate splines. *Medical Physics*, 31(11):2942–2948, 2004.

[29] K. Ding, J. E. Bayouth, J. M. Buatti, G. E. Christensen, and J. M. Reinhardt. 4DCT-based measurement of changes in pulmonary function following a course of radiation therapy. *Medical Physics*, 37(3):1261–1272, 2010.

[30] K. Ding, K. Cao, G. E. Christensen, E. A. Hoffman, and J. M. Reinhardt. Registration-based regional lung mechanical analysis: Retrospectively reconstructed dynamic imaging versus static breath-hold image acquisition. In *Proc. SPIE Conf. Medical Imaging*, volume 7262, page 72620D, 2009.

[31] K. Ding, K. Cao, G. E. Christensen, M. L. Raghavan, E. A. Hoffman, and J. M. Reinhardt. Registration-based lung tissue mechanics assessment during tidal breathing. In *First International Workshop on Pulmonary Image Analysis*, pages 63–72, 2008.

[32] K. Ding, K. Du, K. Cao, G. E. Christensen, and J. M. Reinhardt. Time-varying lung ventilation analysis of 4DCT using image registration. In *IEEE International Conference on Acoustics, Speech and Signal Processing (ICASSP)*, pages 5772–5775, May 2011.

[33] K. Ding, W. Miller, K. Cao, G. Christensen, J. Reinhardt, S. Benedict, B. Libby, and K. Sheng. Quantification of regional lung ventilation from tagged hyperpolarized helium-3 MRI. In *IEEE International Symposium on Biomedical Imaging: From Nano to Macro*, pages 1074 –1077, March 30 - April 2 2011.

[34] K. Ding, Y. Yin, K. Cao, G. E. Christensen, C.-L. Lin, E. A. Hoffman, and J. M. Reinhardt. Evaluation of lobar biomechanics during respiration using image registration. In *MICCAI*, volume 5761, pages 739–746, 2009.

[35] K. Du, J. E. Bayouth, K. Cao, G. E. Christensen, K. Ding, and Joseph M. Reinhardt. Reproducibility of registration-based measures of lung tissue expansion. *Medical Physics*, accepted for publication.

[36] K. Du, K. Ding, K. Cao, J. E. Bayouth, G. E. Christensen, and J. M. Reinhardt. Registration-based measurement of regional expiration volume ratio using dynamic 4DCT imaging. In *IEEE International Symposium on Biomedical Imaging: From Nano to Macro*, pages 424 –428, 30 2011-april 2 2011.

[37] A. Enquobahrie, L. Ibanez, E. Bullitt, and S. Aylward. Vessel enhancing diffusion filter. *The Insight Journal*, 2007.

[38] S. B. Fain, F. R. Korosec, J. H. Holmes, R. O'Halloran, R. L. Sorkness, and T. M. Grist. Functional lung imaging using hyperpolarized gas mri. *Journal of Magnetic Resonance Imaging*, 25(5):910–923, 2007.

[39] J. M. Fellrath and R. M. Bois. Idiopathic pulmonary fibrosis/cryptogenic fibrosing alveolitis. *Clinical and Experimental Medicine*, 3:65–83, 2003.

[40] A F. Frangi, W. J. Niessen, K. L. Vincken, and M. A. Viergever. Multiscale vessel enhancement filtering. In *MICCAI*, volume 1496, pages 130–137, 1998.

[41] M. K. Fuld, R. B. Easley, O. I. Saba, D. Chon, J. M. Reinhardt, E. A. Hoffman, and B. A. Simon. CT-measured regional specific volume change reflects regional ventilation in supine sheep. *J Appl Physiol*, 104(4):1177–1184, 2008.

[42] Y. C. Fung. *Biomechanics: Mechanical Properties of Living Tissues*. Springer-Verlag, New York, 1993.

[43] L. M. Gabe, K. M. Baker, E. JR van Beek, G. W. Hunninghake, J. M. Reinhardt, and E. A. Hoffman. Effect of segmental bronchoalveolar lavage on quantitative computed tomography of the lung. *Academic Radiology*, 18(7):876–884, 2011.

[44] J. Gao, W. Huang, and R. T. Yen. Mechanical properties of human lung parenchyma. *Biomed Sci Instrum*, 42:172–180, 2006.

[45] X. Geng, D. Kumar, and G. E. Christensen. Transitive inverse-consistent manifold registration. In *Information Processing in Medical Imaging*, volume LNCS 3564, pages 468–479, Berlin, July 2005. Springer-Verlag.

[46] Vladlena Gorbunova, Pechin Lo, Haseem Ashraf, Asger Dirksen, Mads Nielsen, and Marleen de Bruijne. Weight preserving image registration for monitoring disease progression in lung CT. In *MICCAI*, volume 5242, pages 863–870, 2008.

[47] T. Guerrero, K. Sanders, E. Castillo, Y. Zhang, L. Bidaut, T. Pan, and R. Komaki. Dynamic ventilation imaging from four-dimensional computed tomography. *Phys Med Biol.*, 51(4):777–791, Feb. 21 2006.

[48] T. Guerrero, K. Sanders, J. Noyola-Martinez, E. Castillo, Y. Zhang, R. Tapia, R. Guerra, Y. Borghero, and R. Komaki. Quantification of regional ventilation from treatment planning CT. *Int. J. Radiation Oncology Biol. Phys.*, 62(3):630–634, Jul 1 2005.

[49] J. Guo, M. K. Fuld, S. K. Alford, J. M. Reinhardt, and E. A. Hoffman. Pulmonary analysis software suite 9.0: Integrating quantitative measures of function with structural analyses. In *First International Workshop on Pulmonary Image Analysis*, pages 283–292, New York, 2008.

[50] J. W. Gurney, W. C. Harrison, K. Sears, R. A. Robbins, C. A. Dobry, and S. I. Rennard. Bronchoalveolar lavage: radiographic manifestations. *Radiology*, 163(1):71–74, 1987.

[51] X. Han. Feature-constrained nonlinear registration of lung ct images. In *Grand Challenges in Medical Image Analysis*, 2010.

[52] R. S. Harris and D. P. Schuster. Visualizing lung function with positron emission tomography. *J Appl Physiol*, 102(1):448–458, 2007.

[53] P. Hellier, C. Barillot, L. Corouge, B. Gibaud, G. Le Goualher, D. L. Collins, A. Evans, G. Malandain, N. Ayache, G. E. Christensen, and H. J. Johnson. Retrospective evaluation of inter-subject brain registration. *IEEE Transactions on Medical Imaging*, 22(9):1120–1130, 2003.

[54] A. J. Henderson. Bronchoalveolar lavage. *Arch Dis Child*, 70(3):167–169, 1994.

[55] E. A. Hoffman and E.van Beek. Hyperpolarized media MR imaging - expanding the boundaries? *Academic Radiology*, 13(8):929–931, 2006.

[56] E. A. Hoffman, T. Behrenbeck, P. A. Chevalier, and E. H. Wood. Estimation of pleural surface expansile forces in intact dogs. *J. Applied Physiology*, 55(3):935–948, Sept. 1983.

[57] E. A. Hoffman and D. Chon. Computed Tomography Studies of Lung Ventilation and Perfusion. *Proc Am Thorac Soc*, 2(6):492–498, 2005.

[58] E. A. Hoffman, R. Jiang, H. Baumhauer, M. A. Brooks, J. J. Carr, R. Detrano, J. M. Reinhardt, J. Rodriguez, K. Stukovsky, N. D. Wong, and R. G. Barr. Reproducibility and validity of lung density measures from cardiac CT scans–the multi-ethnic study of atherosclerosis MESA lung study. *Academic Radiology*, 16(6):689 – 699, 2009.

[59] E. A. Hoffman, J. M. Reinhardt, M. Sonka, B. A. Simon, J. Guo, O. Saba, D. Chon, S. Samrah, H. Shikata, J. Tschirren, K. Palagyi, K. C. Beck, and G. McLennan. Characterization of the interstitial lung diseases via density-based and texture-based analysis of computed tomography images of lung structure and function1. *Academic Radiology*, 10(10):1104 – 1118, 2003.

[60] E. A. Hoffman and E. L. Ritman. Effect of body orientation on regional lung expansion in dog and sloth. *J Appl Physiol*, 59(2):481–491, 1985.

[61] E. A. Hoffman, L. J. Sinak, R. A. Robb, and E. L. Ritman. Noninvasive quantitative imaging of shape and volume of lungs. *J Appl Physiol*, 54(5):1414–1421, 1983.

[62] M. Holden, D. L. G. Hill, E. R. E. Denton, J. M. Jarosz, T. C. S. Cox, T. Rohlfing, J. Goodey, and D. J. Hawkes. Voxel similarity measures for 3-d serial mr brain image registration. *IEEE Trans. Med. Imaging*, 19:94–102, 2000.

[63] K. Hollig. Finite Element Methods with B-Splines . *Society for Industrial and Applied Mathematics*, 2003.

[64] K. Hollig, U. Reif, and J. Wipper. Weighted Extended B-Spline Approximation of Dirichlet Problems. *SIAM J. Numer. Anal.*, 39(2):442–462, 2001.

[65] Klaus Hollig and Ulrich Reif. Nonuniform Web-Splines . *Computer Aided Geometric Design*, 20:277–294, 2003.

[66] S. Hu, E. A. Hoffman, and J. M. Reinhardt. Automatic lung segmentation for accurate quantitation of volumetric X-ray CT images. *IEEE Trans. on Medical Imaging*, 20:490–498, June 2001.

[67] R. Hubmayr, B. Walters, P. A. Chevalier, J. R. Rodarte, and L. E. Olson. Topographical distribution of regional lung volume in anesthetized dogs. *J. Applied Physiology*, 54(4):1048–1056, 1983.

[68] H. J. Johnson and G. E. Christensen. Consistent landmark and intensity-based image registration. *IEEE Trans. Med. Imaging*, 21(5):450–461, 2002.

[69] S. Kabus, T. Klinder, K. Murphy, B. van Ginneken, C. Lorenz, and J. P. W. Pluim. Evaluation of 4D-CT lung registration. In *MICCAI (1)*, pages 747–754, 2009.

[70] S. Kabus and C. Lorenz. Fast elastic image registration. In *Grand Challenges in Medical Image Analysis*, 2010.

[71] S. Kabus, J. von Berg, T. Yamamoto, R. Opfer, and P. J. Keall. Lung ventilation estimation based on 4D-CT imaging. In *First International Workshop on Pulmonary Image Analysis*, pages 73–81, New York, 2008.

[72] D. W. Kaczka, K. Cao, G. E. Christensen, J. H. Bates, and B. A. Simon. Analysis of regional mechanics in canine lung injury using forced oscillations and 3D image registration. *Annals of Biomedical Engineering*, 39(3):1112–1124, 2011.

[73] P. J. Keall, V. R. Kini, S. S. Vedam, and R. Mohan. Potential radiotherapy improvements with respiratory gating. *Australasian physical & engineering sciences in medicine*, 25(1):1 – 6, 2002.

[74] C. A. Kelly, C. J. Kotre, C. Ward, D. J. Hendrick, and E. H. Walters. Anatomical distribution of bronchoalveolar lavage fluid as assessed by digital subtraction radiography. *Thorax*, 42:624–628, 1987.

[75] S. Krishnan, K. C. Beck, J. M. Reinhardt, K. A. Carlson, B. A. Simon, R. K. Albert, and E. A. Hoffman. Regional lung ventilation from volumetric CT scans using image warping functions. In *2004 International Symposium on Biomedical Imaging*, pages 792–795, Washington, DC, 2004.

[76] J. Kybic. *Elastic Image Registration Using Parametric Deformation Models*. PhD thesis, Swiss Federal Institute of Technology Lausanne, EPFL, Lausanne, Switzerland, 2001.

[77] Jan Kybic and Michael Unser. Fast parametric elastic image registration. *IEEE Transactions on Image Processing*, 12(11):1427–1442, November 2003.

[78] S. Lee, G. Wolberg, and S. Y. Shin. Scattered data interpolation with multilevel b-splines. *IEEE Transactions on Visualization and Computer Graphics*, 3:228–244, 1997.

[79] C. Marcucci, D. Nyhan, and B. A. Simon. Distribution of pulmonary ventilation using Xe-enhanced computed tomography in prone and supine dogs. *J Appl Physiol*, 90(2):421–430, 2001.

[80] D. Mattes, D. R. Haynor, H. Vesselle, T. K. Lewellen, and W. Eubank. PET-CT image registration in the chest using free-form deformations. *IEEE Transactions on Medical Imaging*, 22(1):120–128, Jan. 2003.

[81] M. I. Miller, A. Banerjee, G. E. Christensen, S. C. Joshi, N. Khaneja, U. Grenander, and L. Matejic. Statistical methods in computational anatomy. *Statistical Methods in Medical Research*, 6:267–299, 1997.

[82] M. Modat, J. McClelland, and S. Ourselin. Lung registration using the Niftyreg package. In *Grand Challenges in Medical Image Analysis*, 2010.

[83] H. E. Moller, X. J. Chen, B. Saam, K. D. Hagspiel, G. A. Johnson, T. A. Altes, E. E. de Lange, and H.-U. Kauczor. MRI of the lungs using hyperpolarized noble gases. *Magnetic Resonance in Medicine*, 47(6):1029–1051, 2002.

[84] K. Murphy, B. van Ginneken, J. P. W. Pluim, S. Klein, and M. Staring. Semi-automatic reference standard construction for quantitative evaluatoin of lung CT registration. In *MICCAI*, volume 5242, pages 1006–1013, 2008.

[85] B. Nayroles, G. Touzot, and P. Villon. Generalizing the finite element method: Diffuse approximation and diffuse elements. *Computational Mechanics*, 10:307–318, 1992.

[86] L. E. Olson and J. R. Rodarte. Regional differences in expansion in excised dog lung lobes. *J Appl Physiol*, 57(6):1710–1714, 1984.

[87] S. Ourselin, A. Roche, G. Subsol, X. Pennec, and N. Ayache. Reconstructing a 3D Structure from Serial Histological Sections. *Image and Vision Computing*, 19(1-2):25–31, December 2000.

[88] R. Pellegrino, G. Viegi, V. Brusasco, R. O. Crapo, F. Burgos, R. Casaburi, A. Coates, C. P. M. van der Grinten, P. Gustafsson, J. Hankinson, R. Jensen, D. C. Johnson, N. MacIntyre, R. McKay, M. R. Miller, D. Navajas, O. F. Pedersen, and J. Wanger. Interpretative strategies for lung function tests. *European Respiratory Journal*, 26(5):948–968, 2005.

[89] G. P. Penney, J. Weese, J. A. Little, P. Desmedt, D. L. G. Hill, and D. J. Hawkes. A comparison of similarity measures for use in 2-D-3-D medical image registration. *IEEE Trans. Med. Imaging*, 17:586–595, 1998.

[90] P. C. Pratt. Emphysema and chronic airways disease. In *Pulmonary pathology*, pages 654–659. Springer-Verlag, 1988. Edited by D. Dail and S. Hammar.

[91] J. M. Reinhardt, G. E. Christensen, E. A. Hoffman, K. Ding, and K. Cao. Registration-derived estimates of local lung expansion as surrogates for regional ventilation. In N. Karssemeijer and B. Lelieveldt, editors, *Information Processing in Medical Imaging*, volume 4584 of *Lecture Notes in Computer Science*, pages 763–774, Kerkrade, The Netherlands, 2007.

[92] J. M. Reinhardt, K. Ding, K. Cao, G. E. Christensen, E. A. Hoffman, and S. V. Bodas. Registration-based estimates of local lung tissue expansion compared to xenon-CT measures of specific ventilation. *Medical Image Analysis*, 12(6):752–763, 2008.

[93] E. M. Rikxoort, M. Prokop, B/ Hoop, M. A. Viergever, J. P. Pluim, and B. Ginneken. Automatic segmentation of the pulmonary lobes from fissures, airways, and lung borders: Evaluation of robustness against missing data. In *MICCAI (1)*, pages 263–271, 2009.

[94] E. L. Ritman, J. H. Kinsey, R. A. Robb, B. K. Gilbert, L. D. Harris, and E. H. Wood. Three-dimensional imaging of heart, lungs, and circulation. *Science*, 210(4467):273–280, 1980.

[95] H. T. Robertson, R. W. Glenny, D. Stanford, L. M. McInnes, D. L. Luchtel, and D. Covert. High-resolution maps of regional ventilation utilizing inhaled fluorescent microspheres. *J. Applied Physiology*, 82(3):943–953, 1997.

[96] J. R. Rodarte. Stress-strain analysis and the lung. *Fed Proc*, 41(1):130–135, 1982.

[97] J. R. Rodarte, R. D. Hubmayr, D. Stamenovic, and B. J. Walters. Regional lung strain in dogs during deflation from total lung capacity. *J Appl Physiol*, 58(1):164–172, 1985.

[98] D. Rueckert, L.I. Sonoda, C. Hayes, D.L.G. Hill, M.O. Leach, and D.J. Hawkes. Nonrigid registration using free-form deformations: application to breast mr images. *IEEE Transactions on Medical Imaging*, 18(8):712–721, 1999.

[99] V. L. Rvachev and T. I. Sheiko. R-functions in boundary value problems in mechanics. *Applied Mechanics Reviews*, 48(4):151–188, 1995.

[100] V. L. Rvachev, T. I. Sheiko, V. Shapiro, and I. Tsukanov. On Completeness of RFM solution structures. *Comp. Mech.*, 25:305–316, 2000.

[101] V. L. Rvachev, T. I. Sheiko, V. Shapiro, and I. Tsukanov. Transfinite interpolation over implicitly defined sets. *Comput. Aided Geom. Design*, 18:195–220, 2001.

[102] D. Sarrut, V. Boldea, S. Miguet, and C. Ginestet. Simulation of four-dimensional ct images from deformable registration between inhale and exhale breath-hold CT scans. *Medical Physics*, 33(3):605–617, 2006.

[103] D. Shen and C. Davatzikos. Hammer: hierarchical attribute matching mechanism for elastic registration. *IEEE Trans. on Medical Imaging*, 21(11):1421–1439, Dec 2002.

[104] H. Shikata, E. A. Hoffman, and M. Sonka. Automated segmentation of pulmonary vascular tree from 3D CT images. In Amir A. Amini and Armando Manduca, editors, *Proc. of the SPIE'04*, volume 5369, pages 107–116, 2004.

[105] H. Shikata, G. McLennan, E. A. Hoffman, and M. Sonka. Segmentation of pulmonary vascular trees from thoracic 3D CT images. *International Journal of Biomedical Imaging*, 2009(1):36240, 2009.

[106] B. A. Simon and C. Marcucci. Parameter estimation and confidence intervals for Xe-CT ventilation studies: A Monte Carlo approach. *JAP*, 84(2):709–716, 1998.

[107] G. Song, N. Tustison, B. Avants, and J. C. Gee. Lung ct image registration using diffeomorphic transformation models. In *Grand Challenges in Medical Image Analysis*, 2010.

[108] M. Staring, S. Klein, J. H. C. Reiber, W. J. Niessen, and B. C. Stoel. Pulmonary image registration with elastix using a standard intensity-based algorithm. In *Grand Challenges in Medical Image Analysis*, 2010.

[109] C. V. Stewart, Y.-L. Lee, and C.-L. Tsai. An uncertainty-driven hybrid of intensity-based and feature-based registration with application to retinal and lung CT images. In *MICCAI (1)*, pages 870–877, 2004.

[110] T. A. Sundaram and J. C. Gee. Towards a model of lung biomechanics: pulmonary kinematics via registration of serial lung images. *Medical Image Analysis*, 9(6):524–537, 2005.

[111] T. A. Sundaram and J. C. Gee. Quantitative comparison of registration-based lung motion estimates from whole-lung mr images and corresponding two-dimensional slices. In *Proc. ISMRM 15th Mtg*, page p.3039, 2007.

[112] J. K. Tajik, D. Chon, C.-H. Won, B. Q. Tran, and E. A. Hoffman. Subsecond multisection CT of regional pulmonary ventilation. *AR*, 9:130–146, 2002.

[113] P. Thevenaz and M. Unser. Spline pyramids for inter-modal image registration using mutual information. In *Proc. SPIE*, volume 3169, pages 236–247, 1997.

[114] J. Tschirren, E. A. Hoffman, G. McLennan, and M. Sonka. Intrathoracic airway trees: Segmentation and airway morphology analysis from low-dose CT scans. *IEEE Transactions on Medical Imaging*, 24(12):1529–1539, 2005.

[115] S. Ukil and J. M. Reinhardt. Anatomy-guided lung lobe surface segmentation in X-ray CT images. *IEEE Trans. Medical Imaging*, 28(2):202–214, Feb. 2009.

[116] M. Vaillant and J. Glaunès. Surface matching via currents. In *Information Processing in Medical Imaging*, pages 381–392. Springer-Verlag, July 2005.

[117] E. J. R. van Beek, J. M. Wild, H.-U. Kauczor, W. Schreiber, J. P. Mugler III, and E. E. de Lange. Functional MRI of the lung using hyperpolarized 3-helium gas. *Journal Of Magnetic Resonance Imaging*, 20(4):550–554, 2004.

[118] S. Weinberger, B. Cockrill, and J. Mandel. *Principles of Pulmonary Medicine*. Elsevier Science, 2008.

[119] J. B. West and F. L. Matthews. Stress, strain, adn surface pressures in the lung caused by its weight. *J Appl Physiol*, 32(3):332–345, 1972.

[120] Wikipedia. Histogram matching. Hypertext Document.

[121] Y. Yin, E. A. Hoffman, K. Ding, J. M. Reinhardt, and C.-L. Lin. A cubic B-spline-based hybrid registration of lung CT images for a dynamic airway geometric model with large deformation. *Phys. Med. Biol.*, 56:203, 2011.

[122] Y. Yin, E. A. Hoffman, and C.-L. Lin. Mass preserving non-rigid registration of CT lung images using cubic B-spline. *Medical Physics*, 36(9):4213–4222, 2009.

[123] Terry S. Yoo. *Insight into Images: Principles and Practice for Segmentation, Registration, and Image Analysis*. AK Peters Ltd, 2004.

[124] Y. J. Zeng, D. Yager, and Y. C. Fung. Measurement of the mechanical properties of thehuman lung tissue. *J Biomech Eng*, 109(2):169–174, 1987.